Study of sub-monolayer Co/Ru(0001) and multilayers Ru/Nb(110) as platforms for skyrmions-superconductor hybrid realization and Majorana bound states emergence

zur Erlangung des akademischen Grades eines

Doktors der Naturwissenschaften (Dr. rer. nat.)

von der KIT-Fakultät für Physik

des Karlsruher Instituts für Technologie (KIT)

genehmigte

Dissertation

von

M. Sc. Loïc Mougel

aus Dijon (Frankreich)

Tag der mündlichen Prüfung: 22. Oktober 2021
Erster Gutachter: Prof. Dr. Wulf Wulfhekel
Zweiter Gutachter: Prof. Dr. Markus Garst

"The most exciting phrase to hear in science, the one that heralds the most discoveries, is not 'Eureka!' but 'That's funny'..."

Isaac Asimov

Contents

Introduction

In the past decades, technology has evolved a lot toward the miniaturization and the increased capabilities of its components. What required before hours of computation on space demanding and expensive constructions can nowadays be made on personal laptops in a matter of seconds. This comes from the combined effort of the semiconductor and computer industry to build smaller and more powerful devices. Yet, the development of always smaller components is now facing new challenges because of the natural boundaries it encounters. Amongst other limitations, smaller devices are subject to shorter lifetime due to atoms diffusion, playing a more important role the further the size is decreased. Quantum effects such as tunneling effect are also a limiting factor when the size of the device reaches the nanometer scale; at these scales, the quantum effects are not negligible anymore and need to be taken into account. Most devices available commercially just avoid or suppress them, but these solutions become more unrealistic the further down the scale of the device is brought.

To overcome these problems, new kind of devices and computing paradigms have progressively been developed. Quantum computing [1, 2], spintronics and Skyrmionics are examples of research fields aiming to take advantage of the quantum effects and integrate them in the development process. The exploited properties arise from a broad panel of objects including, but not limited to, single atoms [3, 4], solid state hybrid systems [5, 6], skyrmions [7–9] or single photons [10]. The development of these new generation devices opens a door toward smaller devices for high-density data storage, but also for new computing methods, in the case of quantum computing. The field of skyrmionics has mainly been developed to create new kind of memories, both fast and compact [11, 12].

The existence of skyrmions was first postulated in 1962 [13], while the first observation of magnetic skyrmions has been reported in 2009 [14]. Since then, many other works reported the observation of skyrmions in different phases,

i.e. arranged in a lattice [15] or isolated skyrmions [16, 17], and different shapes. The study of magnetic skyrmions dynamics recently gained in popularity because of their application potential in micro-electronics. Indeed, the research grows fast and successful skyrmions creation and destruction were reported using different methods [17, 18]. Furthermore, research teams also reported successful magnetic skyrmions manipulation on thin conducting band using lateral current spin torque transfer manipulation [19]. All this brought together make magnetic skyrmions ideal candidates for the development of high-speed and high-density data novel devices. Although the results are very promising, it keeps the applications in the framework of classic computation.

Recently, it has been proposed to bring skyrmionics in the framework of quantum computing either by exploiting the properties of magnetic skyrmions directly [20] or by using them as platforms for the emergence of exotic states [21, 22]. Indeed, theory suggests that single skyrmions could be placed in contact with a superconductor (SC) to lead to the emergence of exotic states, called Majorana states. These states are intensively investigated because of their application potential in the realization of Q-bits [23, 24]. Observation of Majorana states have already been reported for 1D systems, such as chains of magnetic adatoms placed in contact with a superconductor [25], or semiconducting nanowires [26, 27]. For the particular case of skyrmionics, these Majorana bound states (MBS) are predicted to emerge by pairs in the center of magnetic skyrmions and at their rim [21, 22]. It is proposed to use knowledge of skyrmions dynamics gathered from the last years to braid Majorana states, a key manipulation toward functional Q-bits realization.

The aim of this project was to study the magnetic and superconducting properties of cobalt sub-monolayers (sub-ML) deposited on a ruthenium single crystal cut in the 0001 direction. More specifically, we wanted to confirm the conventional superconducting nature of Ru(0001) and how superconducting properties are transferred to the Co sub-ML. Furthermore, we investigated the possibility to form single magnetic skyrmions to observe the first known skyrmion-SC hybrid.

The first chapter gives a brief introduction to the fundamentals of the experiment. We present the basic principle of quantum tunneling effect and its experimental application for the realization of scanning tunneling microscopy (STM), the tunneling magnetoresistance (TMR) and tunneling anisotropic

magnetoresistance (TAMR) allowing us to investigate surface magnetic structures, a brief derivation of the microscopic model for superconductivity and the difference between type I and type II superconductors and a description of magnetic skyrmions with a short introduction to topology in real space. Finally, at the end of the chapter an important part is dedicated to the understanding of the origin of Majorana fermions in solid-state physics, their emergence and physical realization, their importance in Q-bit realization and the physics underlying their existence in skyrmion-SC hybrid systems.

The second chapter is a short chapter presenting the experimental facility this work was realized on. We present the ultra-high vacuum (UHV) setup and the refrigeration system, as well as the surface cleaning method, the magnetic coil allowing us to apply magnetic fields to the studied system, and the Auger electron spectroscopy (AES) unit.

The third chapter contains the main results of the current work. We start by presenting the surface of a Ru(0001) single crystal and the method used to clean it properly. We also report the observation of the Ru superconducting gap using scanning tunneling spectroscopy (STS), and we confirm the conventional superconductor nature of Ru by measuring the dependency of this gap with temperature. We continue with the deposition of Co sub-ML on the Ru(0001) surface; we report here the observation of a new stacking configuration for Co/Ru(0001), highly transparent to Cooper pairs, the charge carriers for superconducting material. Furthermore, we explain how to form magnetic skyrmions on the Co/Ru(0001) system, and we study their size dependency with the applied magnetic field, giving us insight on the magnetic skyrmions dynamics of this system and the magnetic interactions playing a role in this dynamics. After that, a study of the proximity effect between Ru(0001) and the different observed Co stacking phases is provided, and we demonstrate the possibility to form magnetic skyrmions and recover the superconducting state afterward. Finally, we show that despite the coexistence of magnetic skyrmions and superconductivity, no Majorana states could be observed systematically, due to the topological characteristic number of the formed skyrmions, according to most recent theory [21, 22]. Yet, we present differential conductance spectra exhibiting Majorana-like states and discuss other magnetic structures that could lead to the emergence of MBS, and the possibility to engineer them.

The fourth and last chapter presents a preliminary study of Ru multi-layers deposited on a niobium single crystal cut in the 110 direction. We intend

here to provide a new platform for MBS emergence on skyrmion-SC hybrid systems by coupling the magnetic skyrmions to superconducting vortices. We first present the Nb(110) surface and its reconstruction, and shortly describe its superconducting properties. Afterward, we describe the deposition of Ru multi-layers on the surface, and how the surface of the layered system is impacted by the deposition temperature. Finally, we show that the superconducting properties of Nb transfer to the Ru multi-layers almost without disturbance, including the SC vortices, making it a promising candidate for MBS emergence.

The last part summarizes the main ideas and results of this work, and provides a possible guideline toward future work perspectives on the studied systems.

1 Background

In this chapter, we introduce the concept of Scanning Tunneling Microscopy (STM) and the different associated techniques used in this work to probe the samples. We will cover the fundamentals of STM theory, as well as the underlying principles for Tunneling Magneto Resistance (TMR), Tunneling Anisotropic Magneto-Resistance (TAMR), and superconductivity. Finally, a brief introduction to topology will be given, and we will present the basics of magnetic skyrmions formation as well as the existence and emergence of Majorana fermions.

1.1 Scanning Tunneling Microscopy theory

The tunnel effect is the underlying mechanism for STM. When two electrodes are brought close to contact, electrons can tunnel through the insulating barrier, i.e. go from one electrode to the other despite the absence of conductive material between the two. When we consider a simplified 1D model, the electron can be described with a propagating plane wave which encounters a barrier. A reflection happens at the interface, but the wave function also decays exponentially into the barrier. At the second interface, the wave is again partially reflected, and partially transmitted. This results in a non-zero probability for the electron to be transmitted from one side of the barrier to the other, resulting in quantum tunneling. The total wave function is the solution of the Schrödinger equation solved in the two electrodes and the insulating barrier [28]. This model is shown in Fig. 1.1. For an electron with energy E arriving at a barrier with energy U and width a, one then obtains:

$$\begin{cases} \psi_I(x) = Ae^{ikx} + A'e^{-ikx} \\ \psi_{II}(x) = Be^{\kappa x} + B'e^{-\kappa x} \\ \psi_{III}(x) = Ce^{ikx} \end{cases}, \tag{1.1}$$

with $k = \sqrt{2mE}/\hbar$ and $\kappa = \sqrt{2m\,(U-E)}/\hbar$. ψ_I, ψ_{II} and ψ_{III} describe the electron's wave function before the barrier, inside the barrier and after the barrier, respectively. The functions and their derivatives must be continuous on $x = 0$ and $x = a$ to satisfy the continuity conditions. The probability for the electron to cross the barrier is then given by the transmission coefficient [28]:

$$T = \left|\frac{C}{A}\right|^2 = \frac{4E\,(U-E)}{4E\,(U-E) + U^2 \sinh^2(a\kappa)}. \tag{1.2}$$

The tunneling current is then proportional to the transmission coefficient. In the case of STM, one can consider $e^{\kappa a} \ll 1$, which yields from the above:

$$I \propto T \approx \frac{16k^2\kappa^2}{\left(k^2+\kappa^2\right)^2} e^{-2\kappa a}. \tag{1.3}$$

As one can see from this equation, the current exponentially decreases with an increasing size of the barrier. In the case of STM $\kappa \sim 1$ Å^{-1}, which in turn means that for an increase of 3 Å (typical height difference between two atomic layers) the current would decrease by three orders of magnitude.

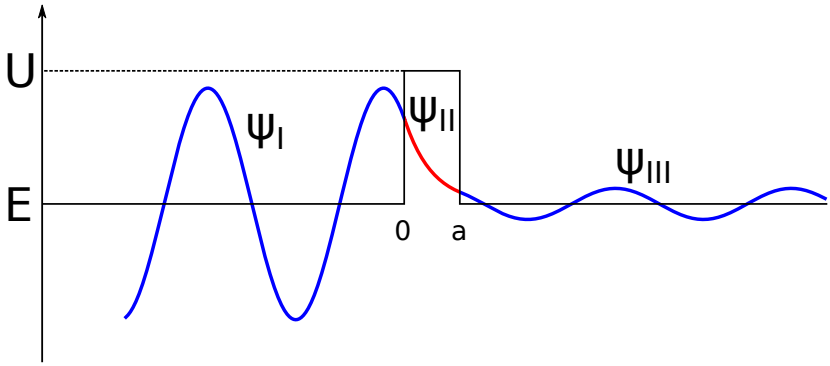

Figure 1.1: Illustration of the tunneling effect: the wave function ψ of the electron is shown in the 3 regions. The wave propagates in region I, decays exponentially in region II and finally propagates with non-zero amplitude in region III.

Although this model is oversimplified compared to real conditions, it allows us to understand how the tunneling current can be used to probe topography of a surface with sub-angström precision. Though it is only a 1D model

and does not take into account the geometry of the system, nor the band structure of the two electrodes, it is insufficient to explain some of the main STM features. Bardeen provided a more precise model in 1961 [29]. In this model, the full Hamiltonian of the system is considered and can be written as:

$$H\psi(\boldsymbol{r},t) = -\frac{\hbar}{2m}\Delta\psi(\boldsymbol{r},t) + V(\boldsymbol{r})\psi(\boldsymbol{r},t). \tag{1.4}$$

To simplify the problem, this Hamiltonian can be considered as two independent Hamiltonian, one for each of the electrodes. With this simplification, we can rewrite Hamiltonian:

$$H_\alpha = \frac{\boldsymbol{p}^2}{2m} + V_\alpha(\boldsymbol{r}), \tag{1.5}$$

with $\alpha \equiv$ tip or sample. The eigenstates of H_α can now be treated independently, and one can use the Fermi golden rule to calculate the transition probability between the tip (μ) and the sample (ν), and vice versa, i.e. calculate the tunneling current I:

$$I = \frac{2\pi e^2}{\hbar}\sum_{\mu,\nu} f(E_\mu)[1 - f(E_\nu + eV)]\left|M_{\mu,\nu}\right|^2 \delta(E_\nu - E_F), \tag{1.6}$$

where f is the Fermi distribution, $M_{\mu,\nu} = -\frac{\hbar}{2m}\int\left(\psi_\mu^*\nabla\psi_\nu - \psi_\nu^*\nabla\psi_\mu\right)dS$ is the matrix element for the transition, e is the charge of the electron and U is the applied bias voltage between the electrodes. The matrix element can be calculated if we assume certain conditions. Tersoff and Hamann described first an approach to the STM geometry, modeling it with a tip with a spherical apex, and an s-type wave function which decays exponentially in the vacuum [30, 31]. In the small bias and temperature conditions, the above equation transforms into:

$$I \propto \int_{E_F}^{E_F+eV} \rho_\mu(E - eV)\rho_\nu(E)T(z,E,eV)dE. \tag{1.7}$$

One can see that the current is proportional to the Density of states (DOS) of the tip ρ_μ and the sample ρ_ν integrated over the energy. Assuming the tip DOS to be constant near the Fermi energy, which is usually a good assumption when a tungsten tip is used, the current depends then only on the DOS of the sample. When making Scanning Tunneling Spectroscopy (STS), one can then investigate the Local Density Of States (LDOS).

1.2 Differential conductance and scanning tunneling spectroscopy

When investigating a sample, interesting properties usually arise in the LDOS. As the current depends only on the integrated LDOS under the right assumptions, measuring the derivative of the current relatively to the energy gives a direct probe for the LDOS:

$$\left.\frac{dI}{dU}\right|_{U=U_0} \propto \rho_{sample}(U_0). \tag{1.8}$$

By measuring the current while varying the applied bias, we can compute the derivative of the signal and obtain the LDOS. However, this can be constraining, time-consuming and the signal over noise ratio may not be optimal. To prevent these disadvantages, one can use a lock-in amplifier. A small AC voltage is added to the applied bias. The tunneling current varies and is demodulated at the same frequency as the modulation frequency. The demodulated signal is then directly proportional to the differential conductance, and therefore gives a direct measurement of the LDOS. This technique provides several advantages: It is not necessary anymore to sweep the bias to probe the LDOS, one can therefore investigate the electronic properties at a given energy. The signal over noise ratio is also usually better using this technique, as the lock-in amplifier is sensitive mostly to the modulation frequency in the demodulated signal [32]. Most of the white noise is canceled if the signal is demodulated over a reasonable number of periods.

1.3 Experimental principle of STM

The principle of STM is to use an atomically sharp metallic tip to probe the topography of the surface of a sample and its electronic properties [31, 33]. The tip is brought close enough to the surface without touching it. A scheme of the tip-sample junction is shown in Fig. 1.2 (a). Without further action, the tip-sample system is at thermal equilibrium, and the probability for tunneling from tip to sample is the same as from sample to tip for the electrons. Hence, no effective current can be observed. A voltage difference is applied between them to bias the chemical potential of one of the electrodes and favor the electron tunneling in one direction. Electrons will flow through the junction,

resulting in a so-called tunneling current. This current experiences very drastic changes when the applied bias or the distance between the tip and the surface change, allowing us to probe the surface properties with great precision.

To investigate the surface properties and topography, the basic idea of the STM, shown in Fig. 1.2 (b), is to move the tip parallel to the surface (in the x-y directions), and measuring the variations of the tunneling current. The latter being strongly dependent with the tip-surface distance, the vertical tip position (z direction) can then be compensated using a feedback loop to maintain a constant current during the displacement. All the next images shown in this work, unless specified otherwise, were recorded using this technique. Since we typically want to achieve sub-nanometer displacement, it is necessary to use piezoelectric elements to realize the movement in the x-y-z space; they have the property to contract or extend in given directions when submitted to a voltage [34]. The tip being mounted on a piezoelectric tube, we can achieve such a precise motion of the tip in all three directions by controlling the voltage applied to the tube.

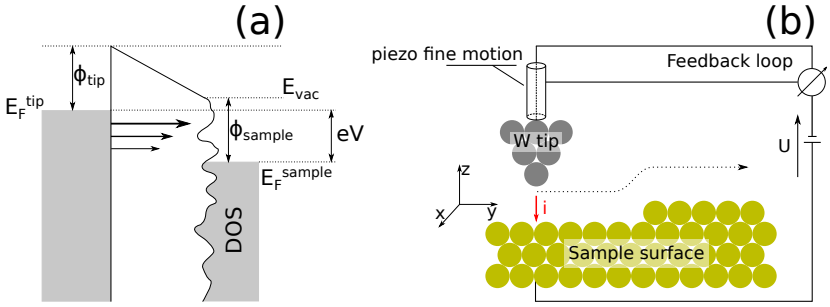

Figure 1.2: Illustration of the STM working principle: (a) Tip-sample junction with external potential eV added. Arrows going from the tip to the sample figures the electron tunneling, resulting in a current. ϕ_{tip} and ϕ_{sample} are the work functions of the tip and the sample, respectively. (b) A bias U is applied to the sample, allowing electrons to flow from the tip to the sample or vice versa. A feedback loop measures the difference between the flowing current and the current set point (controlled by a software in association with a real-time controller) as the tip moves and adjust the voltage applied to the piezo fine motion to adjust the height of the tip (dashed arrow shows the trajectory of the tip).

1.4 Tunneling Magnetoresistance and Tunneling Anisotropic Magnetoresistance

When the surface of a sample exhibits a magnetic structure, it becomes possible to investigate its spatial dependency using tunneling magnetoresistance (TMR) effect or tunneling anisotropic magnetoresistance (TAMR) effect. Both principles rely on a conductance variation at the tunneling junction depending on the magnetic moment orientation below the tip. Both methods present advantages and disadvantages, that we review now while describing the underlying physics behind the process.

Spin polarized STM (SP-STM) is a common technique to investigate magnetic properties of a surface. This exploit the TMR effect [35]; Fig. 1.3 (a) illustrates the variation of the differential conductance in the case of the TMR effect. This effect arises when both electrodes of a tunneling junction have a given spin polarization. During the tunneling process, when considering elastic tunneling process only, the spin of an electron does not change. Therefore, the conductance depends on the alignment between magnetizations of the two electrodes. It has its maximum when the two magnetizations are parallel, and its minimum when the two magnetizations are anti-parallel. The inconvenience with this technique is that it might be difficult to put in place and may induce strong interactions with the studied system. Indeed, the W tip needs to be coated with a material carrying a magnetic moment. If the chosen material is ferromagnetic, such as Fe or Co, the tip will generate a strong magnetic stray field of the order of the saturation magnetization which may affect the measurement, depending on the nature of the experiment. Another possibility is to use antiferromagnetic material such a Cr to coat the tip. This generates a much smaller magnetic stray field. Furthermore, when the tip is prepared, the stability of the apex is not guarantied, and can therefore change or even disappear. One of the great advantages of SP-STM is that it provides a direct readout of the spin direction and orientation. Furthermore, the conductance contrast provided by this technique is rather high (about 40% of the background signal in the case of Co/Ru(0001) [16]), the signal over noise ratio is therefore very good. Yet, because the technique can be difficult to use, and because the stray field generated by the tip may influence the magnetic texture below the tip, we did not use it and preferred to use the second method, described below.

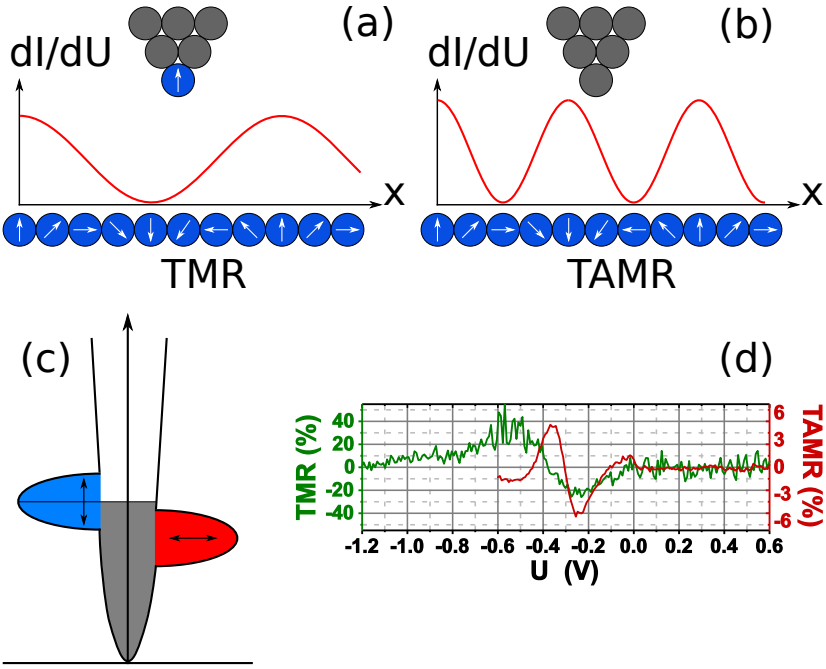

Figure 1.3: TMR and TAMR effects (a) and (b) Schematic view of the dI/dU signal obtained with TMR and TAMR (respectively) for the same spin texture. (c) Schematic view of the density of states for TAMR. The arrows show the orientation of the spins. (d) TMR and TAMR contrast for Co/Ru(0001). Figure taken from [16].

Another possibility to investigate spin textures is to use the TAMR effect [36, 37]. This effect does not require to further prepare the W tip; Fig. 1.3 (b) illustrates the variation of the differential conductance in the case of the TAMR effect. This effect arises from spin-orbit coupling (SOC) which induces an anisotropy for the magnetic moments at the surface. This results in a dependence of the LDOS on the magnetization axis, and therefore of the differential conductance, for whether the spin is in-plane or out-of plane. The scheme shown in Fig. 1.3 (c) illustrates how the TAMR effect can be understood. The contrast between in and out-of plane can be seen with a non spin-polarized tip. Hence, the tip is likely to be more stable as it does not depend on any added material. Furthermore, the tip does not generate a magnetic stray field, the magnetic texture is less affected by it. For Co/Ru(0001)

system, the magnetic texture being rather soft and movable, not having a stray field coming from the tip is important for observation. The main inconvenience of this technique is that the measured signal is much weaker (~6% of the background signal; Fig. 1.3 (d) taken from [16] shows the bias depending contrast obtained for TMR and TAMR effect with a Cr/W and W tip on Co/Ru(0001)). This means that good noise conditions are needed to perform a measurement. Furthermore, the conductance being different for in- and out-of-plane orientations of the spins only, it is not possible at a given position to distinguish the possible directions (for example, for the in-plane case, all angle from 0° to 360° will give the same value for the differential conductance. Similarly, for out-of-plane orientation, it is impossible to discriminate up and down directions beforehand).

1.5 Superconductivity

1.5.1 Microscopic theory of superconductivity

Superconductivity was first discovered by Onnes in 1911 when he discovered that the resistivity of mercury suddenly drops close to 0 below a certain temperature T_c [38]. Some metals, when cooled down to low enough temperatures, see their resistance drop to zero, acting therefore as perfect electric conductors. It was only in 1957 that John Bardeen, Leon N. Cooper, and Robert Schrieffer provided a complete microscopic description of the phenomenon [39]. The so-called BCS theory states that phonons in the material couple electrons and pair them, creating Cooper-pairs [39, 40]. The paired electrons behave then as one quasi-particle obeying a bosonic distribution. This results in the Cooper-pairs condensing in a Bose-Einstein condensate, being able to flow in the material and conduct the current without resistance. For a given metal, we can consider the total potential, the sum of the contributions of the external potential, ion potential and electron potential [40]:

$$\phi = \phi_{ext} + \phi_{ion} + \phi_{e^-}. \tag{1.9}$$

It is useful to consider the relation between the total potential and the external potential through the dielectric constant ϵ:

$$\frac{\phi_{ext}}{\epsilon} = \frac{\phi_{ext} + \phi_{ion}}{\epsilon_{e^-}} = \frac{\phi_{ext} + \phi_{e^-}}{\epsilon_{ion}}, \tag{1.10}$$

leading to $\epsilon = \epsilon_{ion} + \epsilon_{e^-} - 1$. Inside the electron gas, long-distance Coulomb repulsion screening lead to the change $V(r) = \frac{e^2}{4\pi\epsilon_0 r} \rightarrow \frac{e^2}{4\pi\epsilon_0 r} e^{-k_0 r}$. Hence $V(q) \propto \frac{1}{q^2+k_0^2}$. We obtain the relation:

$$\epsilon_{e^-} = 1 + \frac{k_0^2}{q^2}. \tag{1.11}$$

By analogy, we can obtain the ions' response:

$$\epsilon_{ion} = 1 - \frac{\Omega_p^2}{\omega^2}, \tag{1.12}$$

where Ω_p is the plasmonic frequency of the ions. Finally, the complete relation is obtained:

$$\frac{1}{\epsilon} = \frac{1}{1 + \frac{k_0^2}{k^2}} \frac{\omega^2}{\omega^2 - \frac{\Omega_p^2}{\epsilon_{e^-}}}. \tag{1.13}$$

One can notice that, if $\epsilon < 0$, the interaction between electrons becomes attractive, therefore coupling them through the emergence of a virtual phonon (created by one electron, absorbed by the other, coupling them). Fig. 1.4 show the Feynman diagram illustrating the physical mechanism behind Cooper-pairs formation. It is important to note that we here consider the phonon as the coupling virtual particle, but there is no counter indication preventing to have any arbitrary boson such as magnon as coupling particle.

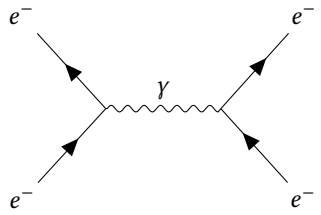

Figure 1.4: Feynman diagram for superconductivity: This Feynman diagram shows how two electrons are coupled together via the creation and absorption of a virtual phonon.

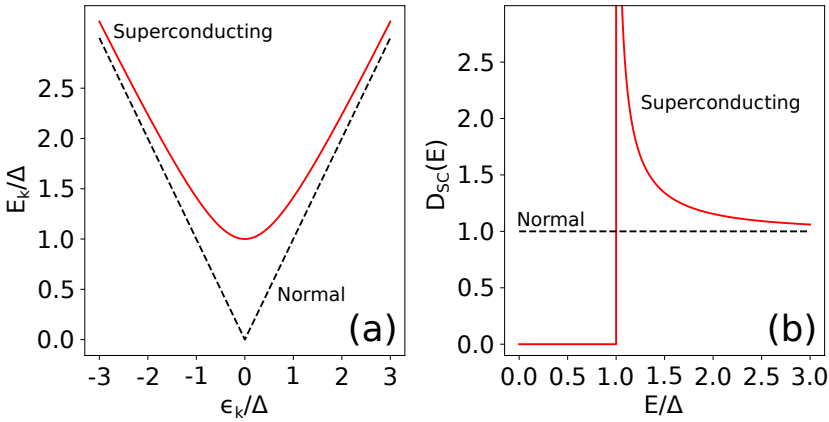

Figure 1.5: Normal vs. superconducting dispersion relation and density of states.

Cooper demonstrated in 1956 that the Fermi sea of electrons is unstable against the formation of bound pairs of electrons [41]. These Cooper-pairs are in a singlet state with $S = 0$, and have therefore bosonic properties. They condense in a Bose-Einstein condensate, and a gap opens in the DOS. Each electron in the Cooper pair sees its energy decreased by the energy gap Δ_0 (at $T = 0$ K) [40, 42]:

$$\Delta_0 = 2\hbar\omega_D e^{-\frac{2}{D_N(E_F)V}}, \tag{1.14}$$

with ω_D the Debye frequency of the material, D_N the density of states of the material and V the attractive potential. The creation of elementary quasi-particles out of the condensate is a fundamental excitation of the superconducting (SC) state. They have the energy:

$$E_k = \sqrt{\epsilon_k^2 + \Delta^2}, \tag{1.15}$$

with $\epsilon_k = \frac{\hbar^2 k^2}{2m} - E_F$. From the equation above, we obtain the DOS for a single electron (or hole) excitation:

$$D_{SC}(E) = \begin{cases} \frac{|E|}{\sqrt{E^2-\Delta^2}} & |E| > \Delta \\ 0 & |E| < \Delta \end{cases}. \tag{1.16}$$

We can see that the DOS is divergent at $E \rightarrow \Delta$, energy of the so-called quasiparticle peak, and zero below the energy gap. A sketch of the dispersion relations and the DOS for normal and superconductor are shown in Fig. 1.5 (a) and (b).

1.5.2 Type I and type II superconductors

Two types of superconductors exist. The first ones, designated as type I superconductor, have the property to be perfect diamagnets, that is their magnetic susceptibility is $\chi = -1$, no magnetic field can penetrate the bulk of the superconductor. This effect is known as the Meissner effect [43]. The magnetic field is repelled at the surface of the superconductor. It penetrates only the surface and decays exponentially with a characteristic length called the London penetration depth λ_L [40, 44]:

$$\lambda_L = \sqrt{\frac{m}{\mu_0 n q^2}}, \tag{1.17}$$

where m is the mass of the charge carriers, n is charge carrier density, and q is the electrical charge of the carriers. If the applied magnetic field goes above the value of the critical field of the superconductor B_c, the superconductivity breaks down and the material becomes a normal conductor again.

On the other hand, type II superconductors have low critical magnetic fields. When the applied magnetic field goes above the value of the first critical field B_{c1}, superconducting vortices appear in the bulk of the superconductor. These vortices trap a quantized magnetic flux:

$$\phi_0 = \frac{h}{2e}. \tag{1.18}$$

This state is also called mixed state, since the material is superconducting outside the vortices, but in the normal state inside. The flux quantization implies that the number of vortices increases with the applied magnetic field, according to:

$$B = n\phi_0, \tag{1.19}$$

where n is the number of vortices per surface unit. The vortices usually arrange in a hexagonal lattice, and the distance between them a_0 is given by:

$$a_0 = \sqrt{\frac{\phi_0}{B}\frac{2}{\sqrt{3}}}. \tag{1.20}$$

When $a_0 \sim 2\xi$, the vortices occupy all the sample and a transition into the normal state happens. This happens when the vortex density is too high, that is, the applied magnetic field goes above a second critical value B_{c2}.

1.5.3 Superconducting proximity effect

The superconducting proximity effect, or Holm-Meissner effect, is a phenomenon happening when a superconductor is placed in contact with a normal conductor, an insulator or a weaker superconductor [45, 46]. Because of the non-locality of the electrons in a metal, the properties of the electrons cannot change discontinuously. The Holm-Meissner effect at an SC-N interface is shown in Fig. 1.6.

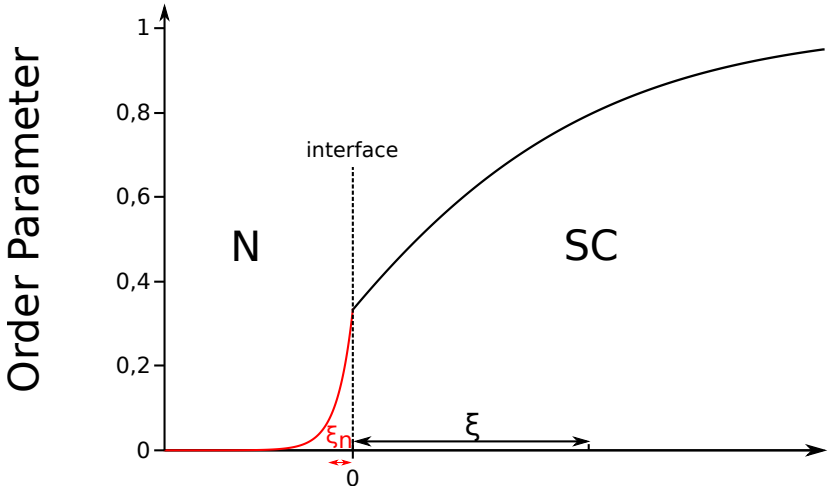

Figure 1.6: Schematic view of the proximity effect for an SC-N interface.

At the SC-N interface, the superconductor transfers Cooper-pairs inside the normal metal, which becomes superconducting. The superconducting state persists inside the normal material and decays exponentially over a characteristic length ξ_N. Similarly, normal conducting electrons are carried from the normal metal to the superconductor, and Cooper-pairs coherence is reduced inside the latter and the SC gap is lowered. The superconducting state is restored in the bulk over the coherence length of the SC material ξ.

1.6 Magnetic skyrmions

1.6.1 Introduction to topology

Topology is a branch of mathematics studying the geometry of objects and their invariant properties under continuous transformations and deformations [47, 48]. The most well-known example coming from this field is probably the topological equivalence under deformation of a torus and a coffee mug, shown in Fig. 1.7. Studying this field requires to define a topological invariant, i.e.

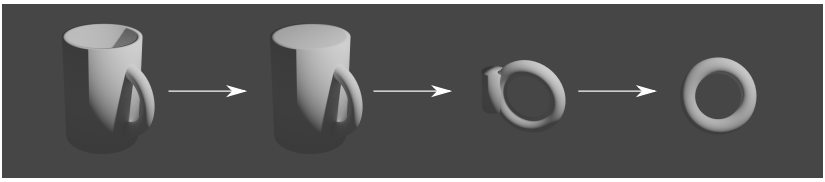

Figure 1.7: Illustration of homeomorphism. A coffee cup (on the left) can be continuously deformed into a donut, or torus (on the right). That is, it is not necessary to create a new hole, breaking the surface, to go from one to another.

an integer quantity that under a given set of allowed transformation may or may not change, *de facto* separating objects into different topological classes. In the case of a cup and a torus, this invariant is the number of holes the object contains. For instance, in this case, a torus and a triple torus are not topologically equivalent under continuous deformation, since it is impossible to continuously deform one into the other without creating new holes (or removing them for that matter).

1.6.2 Case of the magnetic skyrmions

Skyrmions are quasi-particles first described by Tony Skyrme in 1962, first postulated in the framework of particle physics [13]. Magnetic skyrmions are the solid state equivalent of this quasiparticle [14, 49]. It is a two-dimensional object created by projecting a hairy ball where the hairs figure a given spin orientation, also called hedgehog or combed hedgehog configured sphere, onto the plane, as shown in Fig. 1.8. For a given spin configuration in the plane, the topological charge of the configuration, also called winding number, is defined by [47, 50]:

$$S = \frac{1}{4\pi} \int \int \boldsymbol{m} \left(\frac{\partial \boldsymbol{m}}{\partial x} \times \frac{\partial \boldsymbol{m}}{\partial y} \right) d^2 \boldsymbol{r}. \tag{1.21}$$

Changing to polar coordinates $\boldsymbol{r} = (r, r\cos(\varphi), r\sin(\varphi))$, and considering radial symmetry for the spin configuration in the plane, we have the following spin parametrization for a magnetic skyrmion:

$$\boldsymbol{m} = (\cos(\phi)\sin(\theta), \sin(\phi)\sin(\theta), \cos(\theta)), \tag{1.22}$$

where $\phi \equiv \phi(\varphi)$ and $\theta \equiv \theta(r)$ are the azimutal angle and the polar angle of the magnetic moments, respectively. Equation 1.21 then becomes:

$$S = \frac{1}{4\pi} \int_0^{\infty} dr \int_0^{2\pi} d\varphi \frac{d\theta}{dr} \frac{d\phi}{d\varphi} \sin\theta = \frac{1}{4\pi} \left[\cos(\theta)\right]_{r=0}^{r=\infty} \left[\phi\right]_{\varphi=0}^{\varphi=2\pi}. \tag{1.23}$$

One can intuitively see that, in this particular case, this quantity represents the number of time the field covers the 3D sphere of the order parameter space. In the case of a simple skyrmion, the winding number is $n = 1$. It is possible though to have skyrmions with higher winding numbers.

As magnetic skyrmions are planar objects, it is possible to observe them using STM techniques. They are magnetic structures, it is therefore necessary to use TMR or TAMR to be able to image them.

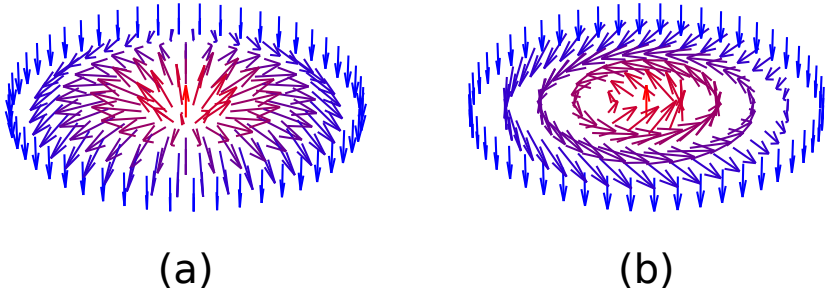

Figure 1.8: Skyrmions with winding number 1: (a) Configuration of the magnetic moments for a Néel skyrmion, corresponding to the projection of a hedgehog sphere (b) Configuration of the magnetic moments for a Bloch skyrmion, corresponding to the projection of a combed hedgehog sphere.

Magnetic skyrmions are stabilized by the Dzyaloshinskii-Moriya interaction (DMI) [51, 52]. This is a noncollinear interaction that originates from spin-orbit coupling, and which Hamiltonian term for two interacting magnetic moments can be written as:

$$H_{i,j}^{DMI} = \boldsymbol{D}_{i,j}\boldsymbol{S}_i \times \boldsymbol{S}_j, \tag{1.24}$$

with $\boldsymbol{D}_{i,j}$ the interaction vector. We can see that if this interaction is introduced in a ferromagnetic system, the parallel arrangement of the spins is not the ground state anymore, but the spin will have the tendency to be tilted relatively to the parallel alignment axis. On systems such as Fe/Ir(111) [53], this interaction leads to the ground state being a lattice of skyrmions, while on Co/Ru(0001) the energy of this interaction is small compared to the exchange interaction's energy; the ratio between the two interactions energies combined with a very small magneto-crystalline anisotropy value leads the magnetic ground state to be a soft magnetic spin spiral [16].

1.7 Topological superconductivity and Majorana fermions

1.7.1 Introduction to topological superconductivity

The concept of topological superconductivity is analog to topology, as explained earlier. But instead of studying the invariant properties under continuous deformations in the real space, the transformations are now done on the band structure [54, 55]. Defining a topological invariant may be quite challenging and highly depends on the symmetry the system is constrained to. The following paragraphs are adapted from [56].

A very basic idea to see if two gapped Hamiltonians are topologically equivalent, is to count the number of levels below zero for each Hamiltonian. If both numbers are equal, then the Hamiltonians can be continuously transformed into one another with no level crossing the zero energy. They can therefore be defined as topologically equivalent. The transformation can be parametrized as such:

$$H(\alpha) = \alpha H' + (\alpha - 1)H \, . \tag{1.25}$$

A continuous transformation between two topologically equivalent Hamiltonians can be seen in Fig. 1.9. In this figure, no energy level crosses the Fermi energy, but it should be noted that even if that happens at some point, it does not mean that the two Hamiltonian are not topologically equivalent, even if an energy level did effectively cross the Fermi level during the transformation. In fact, it is possible to add an arbitrary term β to eq. 1.25 to shift the energy levels up or down to avoid Fermi energy crossing. This may be possible, keeping the transformation continuous without closing the gap. This is possible only if the number of occupied energy level remains the same at the beginning and at the end of the transformation, hence the choosing of this quantity as the topological invariant.

The basic idea behind this simplified image is that two Hamiltonians are topologically equivalent if we can transform one into another without closing the gap. However, defining the number of levels below the Fermi level as a topological invariant does not hold if the system has for instance a sublattice symmetry or electron-hole symmetry. In these cases, the levels on each side of the zero energy are symmetric. While the levels repel each other around zero for the system with sublattice symmetry, this is not the case for the

system with electron-hole symmetry. Then, even if the gap closes under transformation, the number of states remains the same below zero. Examples of continuous transformations for Hamiltonians with sublattice symmetry and electron-hole symmetry are shown in Fig. 1.10 (a) and (b), respectively.

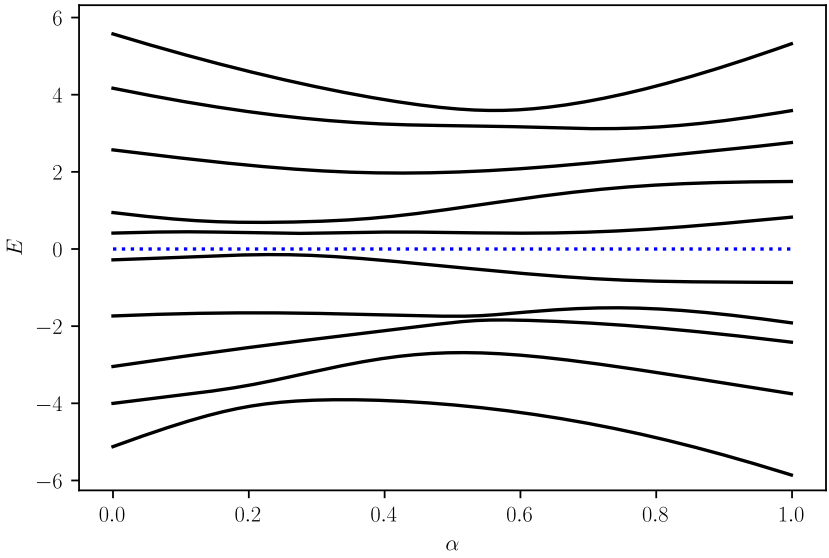

Figure 1.9: Topological equivalence between two Hamiltonian: Graph showing the continuous transformation from one Hamiltonian to another, following eq. 1.25. α varies from 0 to 1 and the transformation $H \to H'$ happens. The gap never closes. No energy level crosses the Fermi energy, and the total number of occupied states remains the same, making H and H' topologically equivalent in this definition. H and H' are taken real and without particular symmetry.

A number that can be taken for a topological invariant is then a quantity called the pfaffian Pf of the matrix A, or more precisely its sign. Pf is defined as follows:

$$Pf(A)^2 = \det(A). \tag{1.26}$$

The pfaffian has the properties that, when the gap closes, its sign changes, which make it a good quantity for topological classification of Hamiltonian with electron-hole parity.

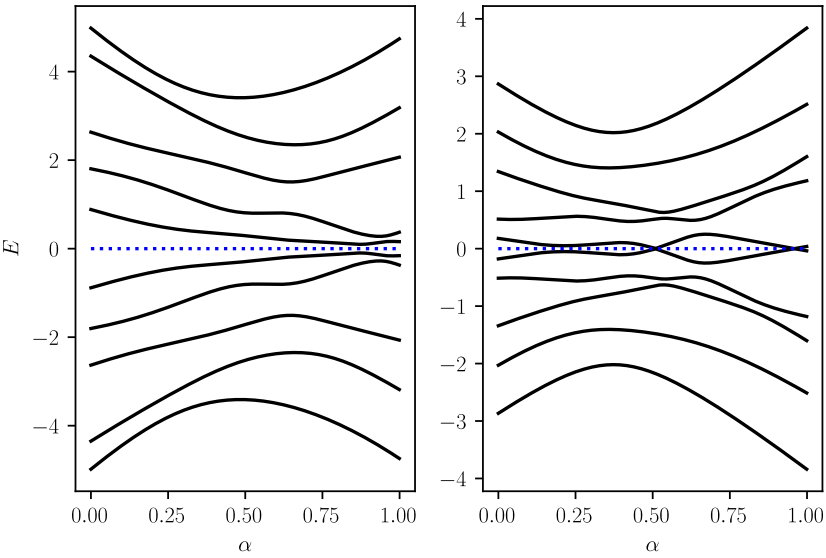

Figure 1.10: Continuous transformation of Hamiltonians with added symmetry: (a) Transformation of a Hamiltonian with sublattice symmetry. The levels are symmetric relatively to the Fermi energy and never cross the Fermi level. (b) Transformation of a Hamiltoninan with electron-hole symmetry. The levels are symmetric relatively to the Fermi level, but can cross it.

1.7.2 Emergence of Majorana fermions

Now that we introduced basic principles for topological superconductivity, we are going to introduce Majorana fermions and explain how they can emerge as in-gap states in superconductors.

Majorana fermions where first hypothesized by Ettore Majorana in 1937 [57, 58] in the framework of particles physics. The particularity of these particles is that they are their own antiparticles, and this is only possible if their rest energy is 0 [58, 59]. Although it is thought that such particles could exist, we here focus on the solide-state quasi-particle analog that would appear in the LDOS as spatially localized zero energy states. They are called Majorana zero states (MZS).

When we consider fermionic creation and annihilation operators, obeying Fermi commutations rules $c^\dagger c + cc^\dagger = 1$, $c^2 = 0$ and $\left(c^\dagger\right)^2 = 0$, we can rewrite the operators as a linear combination of new creation and annihilation operators:

$$c = \frac{1}{2}\left(\gamma_1 + i\gamma_2\right), \tag{1.27}$$

$$c^\dagger = \frac{1}{2}\left(\gamma_1 - i\gamma_2\right). \tag{1.28}$$

For these rewritten operators to satisfy the anticommutation relation, the following relations have to be true:

$$\gamma_1 = \gamma_1^\dagger, \tag{1.29}$$

$$\gamma_2 = \gamma_2^\dagger. \tag{1.30}$$

As one can see, this does imply that the particle corresponding to these new γ_i operators are their own antiparticles. As well, they must obey the following relation $\gamma_1\gamma_2 + \gamma_2\gamma_1 = 0$, $\gamma_1^2 = 0$ and $\gamma_2^2 = 0$. Equation 1.27 and 1.28 show that Majorana fermions are hypothetical particles composing regular fermions. This suggests that it is not possible to obtain isolated MZS, i.e. they always come in even numbers. In the case of condensed matter, they will be considered as elementary bricks for electrons, but any fermion creation and annihilation operators can always be written in terms of Majorana operators. And it is yet but a fact that MZS always appear in pairs. The way the fermionic operators are written also suggest that Majorana fermions always compose a regular fermion, and that it would be impossible to separate them in the real space. It is although possible to get two spatially separated MZS using bulk edge correspondence.

1.7.3 Bulk edge correspondence as key ingredient for Majorana fermions observation

A simplified model can let us understand the nature of isolated Majorana fermions. Let us consider a chain of N sites, where each site can host a fermion. This implies that each site can host two Majorana states [56, 60]. If

each occupied site is attributed an energy μ, each excited state has energy $\pm\frac{|\mu|}{2}$ and the Hamiltonian is:

$$H = -\mu \sum_{n=1}^{N} c_n^\dagger c_n = \frac{i\mu}{2} \sum_{n=1}^{N} \gamma_{2n-1}\gamma_{2n}. \tag{1.31}$$

This coupling is illustrated in the top panel in Fig. 1.11. In this picture, each Majorana pair is localized on one site, hence no isolated state emerges, and the system band structure is gapped everywhere. Now, let us consider a different coupling, where each Majorana state pair is made by coupling two adjacent sites. If we attribute each excited state an energy $\pm\frac{|\nu|}{2}$, the Hamiltonian is then written:

$$H = \frac{i\nu}{2} \sum_{n=1}^{N-1} \gamma_{2n}\gamma_{2n+1}. \tag{1.32}$$

This particular coupling is illustrated in the lower panel of Fig. 1.11. In this case, the extremities of the system each host one unpaired state, which do not appear in the Hamiltonian, i.e. they are zero energy states. The system's band structure is therefore gapped everywhere but at its extremities. These states are bound to a given location, and are called Majorana bound states (MBS).

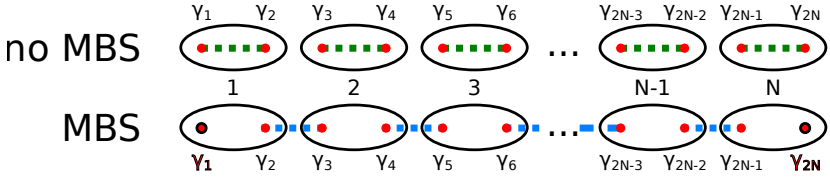

Figure 1.11: Model of dominoes: Upper panel: Schematic view of Majorana pairs being coupled on sites. No Majorana mode is isolated and no MBS emerges. Lower panel: Schematic view of Majorana pair being coupled in between sites. Two isolated (uncoupled) Majorana states remains at the extremities of the system, and do not interact with each other because the system is gapped everywhere else, leading to the emergence of bound zero energy states at the extremities.

From this toy model, we can already obtain an idea on how to form unpaired Majorana states, and we can compute a more realistic model: the Kitaev chain

model [60]. From above, we can write the tight binding Hamiltonian of a superconducting wire with fermionic operators:

$$H = -\mu \sum_n c_n^\dagger c_n - 2\nu \sum_n c_{n+1}^\dagger c_n + \Delta \left(\sum_n c_n c_{n+1} + h.c. \right), \tag{1.33}$$

The special case when $2\nu = \Delta$ and $\mu = 0$, corresponding to the unpaired Majorana state. However, if the regime for this set of parameters can appear to be exceptional and therefore not suitable for real life realization, it is actually robust. The unpaired Majorana states remain as such as long as they do not interact with each other, that is, as long as the bulk of the wire is gapped. When the gap closes under a variation of the parameter μ, this is the point where the two unpaired Majorana states interact, and the system undergoes a topological phase transition. It becomes topologically trivial and no unpaired Majorana states exists anymore. This transition happens at:

$$\mu = \pm 4\nu. \tag{1.34}$$

Coupling the two unpaired Majorana states is impossible as long as the bulk is gapped without violating the particle-hole symmetry [61, 62]. The only way to do it is by closing the gap in the bulk and reopen it afterward.

1.7.4 Majorana fermions as a platform for Qbit realization

Because of their spatial separation, their robustness under small variations of the Hamiltonian parameters and their non-abelian statistics (derivated in the next paragraph), Majorana fermions are ideal objects to make robust Qbits with very long lifetimes [59, 63, 64]. Let us consider a chain of Majorana fermions as shown in Fig. 1.12, where we have the possibility to move the states and exchange their positions. The transformation is supposed to be adiabatic, and the quantum state of the system $|\psi\rangle$ does not leave the ground state manifold. The initial and final states are connected by the unitary operator U:

$$|\psi\rangle \rightarrow U\,|\psi\rangle\,. \tag{1.35}$$

The expression for U can be found with the following considerations:

1. Exchanging two MZS does not change the total fermion parity. Hence, we must have $[U, P_{tot}] = 0$.

2. We consider that U only depends on the exchanged states, and no other ones. Hence, U must be a function of γ_n and γ_m (where n and m are the index of the exchanged states).
3. Finally, since the total fermion parity is conserved, U must be a function of $\gamma_n\gamma_m$.

This leads us to the general expression of U:

$$U = e^{\beta\gamma_n\gamma_m} = \cos(\beta) + \gamma_n\gamma_m \sin(\beta), \tag{1.36}$$

with β a real number. When we then consider the exchange of two Majorana states, it leads to $\beta = \pm\frac{\pi}{4}$ [59]. The sign of β speaks for the fact that exchanging the particle clockwise or counterclockwise is a different operation, and acts differently on the wave function. If we take as an example a two-fermion system (which automatically yields four Majorana states), we obtain the four eigenvectors of the Hilbert space $|00\rangle, |11\rangle, |01\rangle, |10\rangle$. If the system finds itself in the initial state $|00\rangle$, we can exchange Majorana states 2 and 3 (assuming clockwise inversion, $\beta = +\frac{\pi}{4}$):

$$|00\rangle \rightarrow \frac{1}{\sqrt{2}}\left(|00\rangle - i\,|11\rangle\right). \tag{1.37}$$

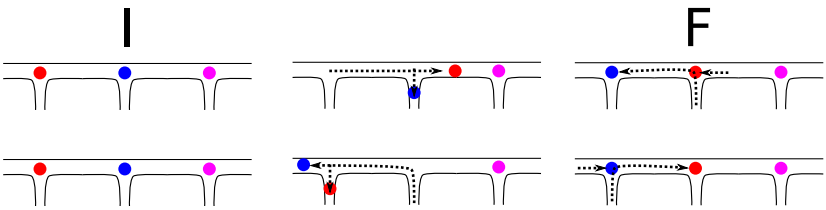

Figure 1.12: Illustration of a braiding operation with MZS: A chain is in an initial state I, and is brought to a final state F. Depending on how we move the MZS, i.e. clockwise of counterclockwise shown on the upper panel and the lower panel, the final positions of the states can be the same, although the wave functions of the system F will differ.

The exchange of two particles does not necessarily result in a trivial state of the wave function, but rather in a linear combination of the base states. For a two-fermion system, the exchange operators are explicated in the 4.3. Interestingly, we can note that, unlike bosons and fermions which wave functions are

respectively multiplied by 1 or −1 when two particles are exchanged, MZS wave function does not obey such a statistic, and is furthermore sensitive to clockwise-counterclockwise exchange. MZS are therefore anions obeying non-abelian statistics [59].

This property can be used to explore the full Hilbert space of the wave function by choosing in which order and in which direction one has to exchange the states to accomplish an operation. This operation is called braiding. Theoretical works have already been published to describe how the basic AND, OR and XOR quantum gate could be realized by braiding Majorana states [63, 64].

1.8 Skyrmions-SC hybrid as host for Majorana fermions

As we saw before, magnetic skyrmions are characterized by single or multiple spin rotations occurring radially. It is known that, when a spin rotation occurs in one dimension, it leads to the emergence of MBS [65–67]. The analogy between a one dimensional spin rotation and a skyrmion can be considered, as the later can be viewed as a two-dimensional radial spin rotation [21]. Indeed, a helical field is gauge equivalent to a Zeeman field and Rashba spin-orbit interaction (SOI), key ingredients to the emergence of MBS [68]. Recent work showed that the analogy between a helical structure in 1D and a skyrmion in 2D is valid and that the latter, placed in contact with and S-wave SC should also lead to the emergence of MBS for the same reason [21, 22]. A necessary condition for this to happen, is for the skyrmion to have an even winding number. If this is not the case, then the effective winding number has to be incremented by one, either by creating a new skyrmion with $n = 2$ by merging two $n = 1$ skyrmions, or by coupling a skyrmion with an odd winding number with a superconducting vortex. Theoretical analysis has shown that the first option is not a realistic option for an experiment, as the barrier to overcome to merge the skyrmions is too high, the skyrmions would rather undergo a discontinuous transformation and result in a $n = 1$ skyrmion [22]. Nonetheless, a recent publication predicts that if the skyrmions are not perfectly round, which is a realistic view in a real experiment and the case for skyrmions formed on Co/Ru(0001), MBS could appear even on skyrmions with a winding number $n = 1$ [69].

1.9 Skyrmion and Majorana fermions for Qbits realization

As we just saw, when a skyrmion is placed in contact with a superconductor, one can expect the emergence of MBS. Furthermore, as explained previously, MBS can be braided to realize quantum computation.

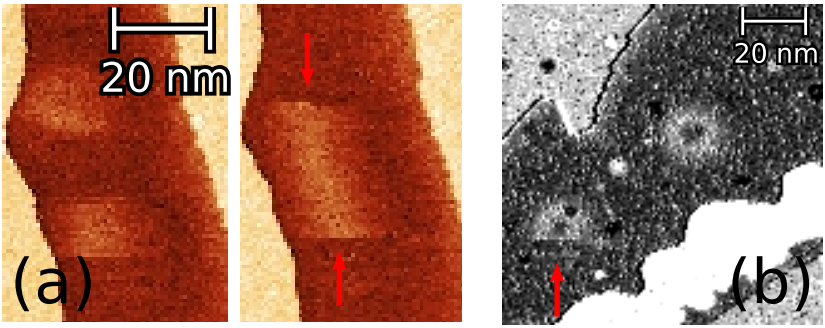

Figure 1.13: Displacement of magnetic skyrmions: (a) and (b) show skyrmions that were moved during an STM scan. (a) also shows the possible merging of two skyrmions. The displacement is visible by the discontinuity on the spin texture, indicating that the skyrmions moved from one recorded line to the other. The discontinuity is shown with a red arrow to guide the eyes. (a) taken from [16] $I = 10$ nA, $U = -400$ mV,$U_{mod} = 40$ V_{RMS}. (b) $I = 1$ nA,$U = -350$ mV,$U_{mod} = 50$ mV.

Yet, one major inconvenience of previously observed MBS, is that they were not movable. Creating MBS linked to a skyrmion would allow us to get rid of this problem. Several studies already demonstrated that it was possible to move skyrmions at will using driving current [19, 70]. Co/Ru(0001) presents several advantages:

- Skyrmions do not form spontaneously in a skyrmion lattice, unlike Fe/Ir(111) [53], which allows us to form individual and independent skyrmions.
- The formed skyrmions are rather soft and elongated in the ground state, breaking radial symmetry, which is an assumption of the previously developed theory. It therefore may act as a hybrid between perfectly

round skyrmion and Kitaev chainlike-system. Since they are soft, it means they can be deformed and moved.

- Movable skyrmions are the key for braiding. In our case, moving and annihilating skyrmion with action of the tip has already been demonstrated [16] and successfully reproduced in this work, as shown in Fig. 1.13 (a) and (b)

1.9.1 Skyrmions for Majorana states braiding

Previous works already reported the observation of MZS [25–27, 71]. Although it opened the field for research, in all the reported observations, no displacement of the states were performed. This is required if one wants to use these states for quantum computing, because braiding the states is essential. The limiting factor is often that the states are bound to defects, or that the system is one dimensional, and does not provide room for moving the states (such as the Kitaev chain system).

As we saw before, if skyrmions are placed in contact with a superconductor, two spatially separated MBS might emerge, one in the center of the skyrmion, and the other one at its rim. Although it seems that the states are once again bound, it is known that skyrmions can be moved in a controlled way using lateral current [19, 70], or using lateral displacement of the tip of an STM [16]. Doing so would induce local perturbations, to which Majorana state and Q-bit made with them are not sensitive to, due to the robustness of bulk-edge correspondence. Therefore, movable skyrmions on which Majorana states would be bound might be suitable objects for Q-bit realization.

2 Scanning Tunneling Microscopy - experimental setup

In this chapter, we present the experimental setup used in this work. An overview of the measurement facility will be given, including a description of the system layout, as well as a description of the preparation methods. This work was made using a homebuilt STM designed and assembled in the group of Prof. Wulf Wulfhekel [72], cooled down with a dilution refrigerator, allowing temperatures as low as 30 mK. Therefore, we will also shortly discuss the working principle of dilution refrigerators. Finally, a very brief description of Auger electron spectroscopy techniques will close this chapter.

2.1 ultra-high Vacuum setup

The working environment is an ultra-high vacuum (UHV) setup. A complete layout of it can be seen in Fig. 2.1. It contains three chambers: a load-lock, a preparation chamber and an STM chamber, each separated by a gate valve. This allows us to transfer, prepare and measure samples without altering the pressure conditions in the other chambers. The base pressure in the load-lock is $P = 4.0 \times 10^{-8}$ mbar. It is the only non UHV chamber, as its purpose is to transfer samples in and out the system. Both preparation and STM chambers have a base pressure of $P = 1.0 \times 10^{-10}$ mbar. This is necessary for our experiments, as we study surfaces; the preparation and measuring processes require as low contamination as possible. Furthermore, UHV conditions in the STM chamber allow us to thermally decouple the cryostat from the ambient temperature bath outside the setup, making it possible to cool the samples to sub-kelvin temperatures. A set of manipulators allows us to manipulate samples in-situ without leaving UHV conditions.

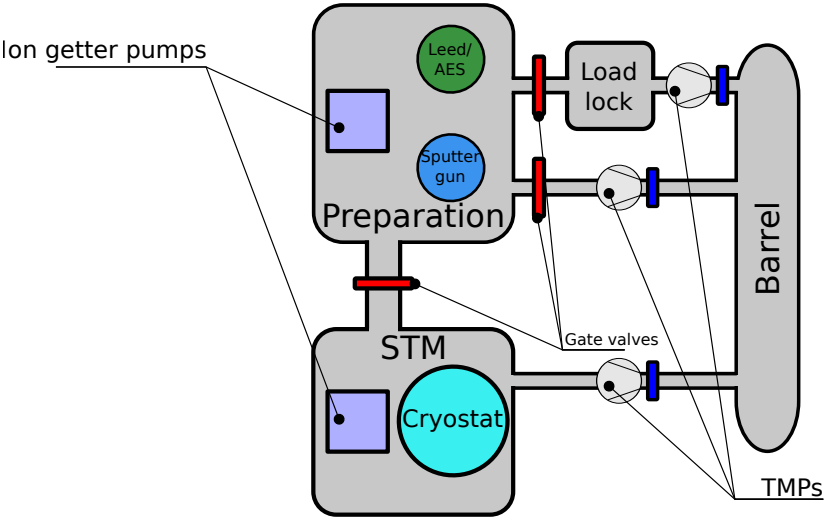

Figure 2.1: UHV setup layout.

The UHV conditions require to use turbomolecular pumps (TMPs). Each chamber is equipped with one TMP. The backside of each TMP is connected to a common barrel, itself connected to a rotary pump generating a pre-vacuum. The barrel can be decoupled from the rotary pump by means of a magnetically controlled valve if necessary. However, TMP cannot be kept running during STM experiments, as STM requires a low level of vibrations. Hence, while the TMPs are off, the UHV conditions in preparation and STM chambers are maintained with ion-getter pumps. The preparation chamber also features a titanium sublimation pump which can be manually triggered to improve low pressure conditions. The STM additionally contains a passive sorption pump (SAES pump).

On the preparation chamber are mounted various devices allowing diverse sample preparations. An ion gun (so-called sputter gun) is located on the top of the chamber. Connected to it, two bottles of gas mounted on leak valves allow the user to introduce some amount of gas in the chamber with a $\sim 10^{-9}$ mbar precision. Although the experiments are made in the STM chamber, some pre-analysis can be executed in the preparation chamber thanks to the coupled low-energy electron diffraction (LEED) and Auger electron spectroscopy (AES) unit. These techniques are meant to control the

order and the purity of the surface. A quadrupole mass spectrometer is also connected to the chamber to check gas purity and the nature of desorbing gas in the chamber when it occurs.

The manipulator is also equipped with a replaceable filament placed below the sample, and it is possible to let compressed air or liquid nitrogen flow in it to actively cool it while heating the samples to avoid overheating of the manipulator.

Once the sample is cleaned using the methods described below, one can deposit a variety of material using the evaporators placed on the side of the preparation chamber. Five evaporators are connected to the chamber. The STM chamber also contains a four pockets evaporator oriented on the direction of the sample placed in the STM, which make it possible to deposit single atoms on cold surfaces.

2.2 Low-temperature setup

2.2.1 Cryostat system

Above the STM body is the cryostat system. It consists of three parts, insulating the STM from the outside and cooling it down to cryogenic temperatures. In Fig. 2.2 (a) and (b) a schematic cross-section of the system and of the STM body are shown. The liquid Nitrogen (LN_2) is the outmost part of the cryostat. The tank can hold LN_2 for ~ 60 h, and is decoupled from the room temperature bath by UHV. It precools some parts of the system, as well as the dilution stage. It also provides protection against thermal radiations for the liquid helium (LHe) tank.

The LHe tank is located below the LN_2 tank, and inside a thermal shield, cooled down to 77 K thanks to the latter. It provides cooling power for the dilution system, and is itself connected to a radiation shield protecting the dilution system and the STM body against thermal radiations.

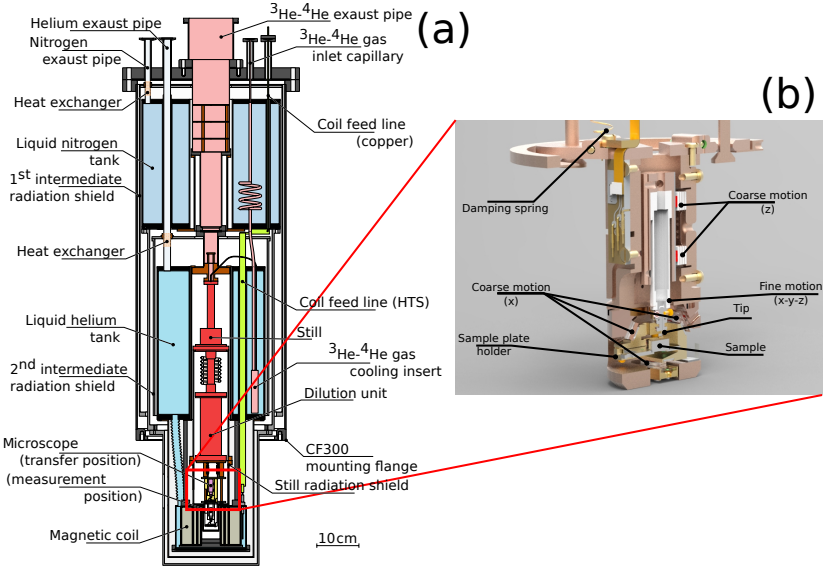

Figure 2.2: Inside view of the low-temperature setup and of the STM body: (a) Open view of the cryostat and dilution system. Taken from [72]. (b) open view of the STM body indicated by a red box in (a).

2.2.2 Dilution system

To achieve low-temperature cooling of the STM body and the sample, we use a dilution refrigerator built by BlueFors [73]. It allows to bring the temperature of the sample down to 30 mK [74–76]. This is required to increase the energy resolution of tunneling spectroscopy, and allows to study some superconducting sample with low T_c. A schematic view of the dilution refrigerator and the diagram phase of the ^{3}He/^{4}He mixture are shown in Fig. 2.3 (a) and (b), and we now describe the working principle. A mixture of ^{3}He/^{4}He gases is stored in a tank outside the STM room. One can control the opening/closing of pneumatic valves in the STM room to control the flow of the mixture inside the system. First, the mixture is precooled via heat exchange with, in order, the LN_2 tank, the LHe tank and the still, i.e. the outlet part of the cooling system. The Joule-Thomson (JT) expansion happens at the stage of the same name and is realized by bringing the inlet's pressure to about 2 bar. The mixture condenses and cools down even further. When enough mixture is

condensed, it fills the still, which can be pumped. By pumping the still, due to the evaporation of the mixture, the temperature can be brought down to ~ 800 mK, while the pumped mixture is circled back in the line.

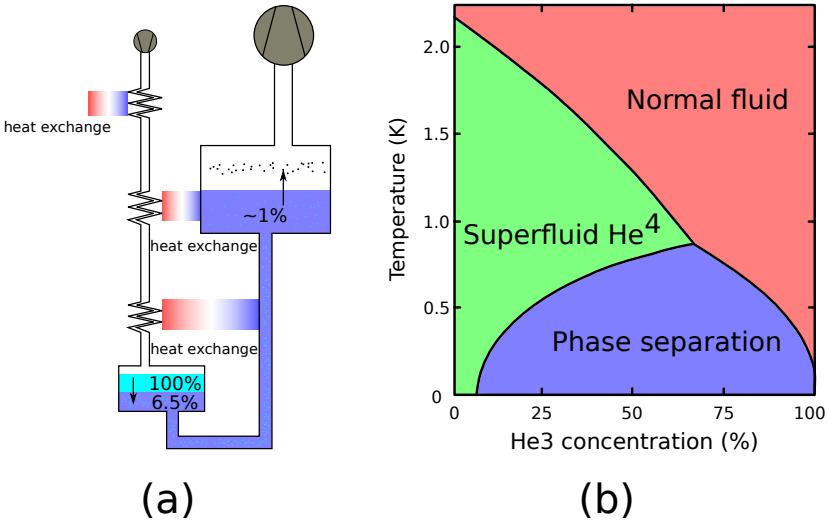

Figure 2.3: Dilution refrigerator setup and ^{3}He/^{4}He phase diagram: (a) Schematic view of the dilution refrigerator stage. Adapted from [76]. (b) ^{3}He/^{4}He phase diagram.

For temperatures comprised in the range $2.17\ \text{K} > T > 870$ mK (depending on ^{3}He concentration, and given that it is lower than 67%), the mixture undergoes a phase transition where ^{4}He becomes superfluid, and ^{3}He is a Fermi liquid mixed into the superfluid phase. When the mixture reaches temperature lower than 870 mK (for a ^{3}He concentration of 67%) due to the evaporation, another phase transition happens, where the two phases are poorly miscible. That is, the ^{4}He rich phase (also called diluted phase, the lower one) is made of superfluid ^{4}He with low concentration of ^{3}He of about 6.5%, while the ^{3}He rich phase (also called concentrated phase, standing on the top) is made of pure liquid ^{3}He. By pumping the still when the mixture is in the separated phase, the vapor pressure being much lower for ^{4}He than for ^{3}He at this stage, the ^{3}He is pumped out of the diluted phase, resulting in a non-equilibrium situation at the interface between concentrated and diluted

phase. Therefore, ^{3}He will cross this interface from the concentrated phase to the diluted phase. This process is endothermic. Hence, energy is taken from the environment, effectively cooling it. By coupling the STM body to the mixer, its temperature will go down to the base temperature.

2.3 Surface preparation

2.3.1 Surface cleaning

As for the sample preparation itself, we use the sputter gun unit to clean the surfaces by removing atomic layers. This is achieved by accelerating electrons in the surface direction. The electrons go through pure argon gas and ionize it. The argon ions are then accelerated and hit the surface with near grazing incidence, removing material from the surface, thus cleaning it from surface impurities. Below the sample is also located a replaceable filament. With it, we can softly anneal the sample by thermal radiations to temperatures up to $\sim$ 500℃. It is also possible to reach much higher temperatures for the sample by applying a high voltage (HV) to it. By doing so, emission conditions can be reached and the emission electrons heat the sample to up to $T = 2000$℃. Doing so evens the surface, which was rough due to the sputtering operation, and lead to desorption of adsorbed impurities. Two to three cycles of sputtering are usually enough to obtain a clean surface for a sample that was stored in the chambers for a long time (several days). Inter-samples preparation usually require no more than one cycle to be properly cleaned, as it is only necessary to remove the deposited materials, often consisting in less than a monolayer of material.

In the case of the Ru(0001) surface, sputtering is usually not enough to reach the desired level of cleanness. Single crystals of ruthenium have the tendency to capture carbon atoms and store them in the bulk as impurities. Sputtering and annealing the sample is usually not enough to get rid of these impurities. As they come from the bulk, just removing the first atomic layer off the surface does not decrease the carbon concentration in the bulk. As such, it is necessary for the sample to go through another cleaning step, called oxygen annealing. During this process, the sample is put in a pure O_2 atmosphere under a typical pressure of 5.0×10^{-8} mbar. Furthermore, the sample is heated to $T \approx 1000$℃. Due to the elevated temperature of the sample, carbon

atoms migrate from the bulk of the crystal to the surface, where they react with the O_2 gas. Since the heating temperature is only about 40 to 50% of the melting point, this diffusion of the carbon to the surface remains a long process, and several cycles of several hours are required to obtain the wanted cleanness for the surface. Between each cycle, it is necessary to wait until all the oxygen is pumped out of the chamber. The sample is then flashed to a minimum temperature of $T = 1500$℃ to remove the formed RuO and the adsorbed O_2 gas from the surface by desorption to continue the process with a pure Ru surface. It is important to note that the surface's cleanness cannot be controlled using AES nor LEED, as the carbon impurities represent only a small fraction of the atoms on the surface. Hence, they do not disturb the lattice arrangement significantly, and the quantity of carbon atoms is below the detection level of AES. More detailed information about the cleaning process are given in section 3.1.1.

2.3.2 Metal deposition on the surface

To deposit the wanted species on the surface, we used commercially available evaporators to use molecular beam epitaxy (MBE). The principle of this method is to place the evaporation material, often in the form of a rod or pellets, in the center of a filament. Current is put through the filament, and HV is applied between the evaporation material and the filament. The emission electrons go from the filament to the rod, and heat it. The material is heated to high enough temperatures so that atoms detach from the rod into the vacuum. The flux current is measured by the electronics of the evaporator and usually is of the order of $10 - 100$ nA. For each system, a short section will specify the used material and parameters used to prepare it in the corresponding chapter.

2.4 Magnetic field

Additionally to the STM setup, a magnetic coil is available to apply magnetic fields to the systems. When it is in position for experiments, the STM body lays in the center of the coil. The coil is capable of applying up to 7.5 T. The current in the coil is controlled by a commercial controller sold by Oxford

Instruments [77] and allows to regulate the applied magnetic field, and the ramping rate.

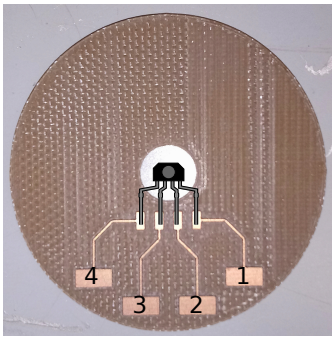

Figure 2.4: Hall probe wiring: picture taken of the PCB and view of the connection to the THS 119 Hall sensor [78].

	2	3	4
1	0.569 Ω	0.540 Ω	0.566 Ω
2	x	0.573 Ω	0.710 Ω
3	x	x	0.570 Ω

Table 2.1: Resistance values between each pin.

When running experiments, we realized that, the relation between applied current and applied magnetic field does not exactly follow the calibration. It was impossible to counteract the small remanent field after applying a large magnetic field. While this is not an issue for certain experiments, the remanent field being quite small ($\approx$ 7 to 10 mT after applying 300 mT), this became a problem when working on the Co/Ru(0001) system, as field as low as $|B| = 5$ mT are required in this case. To overcome this problem, we proceeded to the installation of a four wire hall probe. The hall probe we installed is the GaAs THS 119 made by Toshiba [78]. We choose this hall probe since, despite its technical specifications, it has been demonstrated that this sensor could operate at cryogenic temperatures [79]. Mounted on a small Printed Circuit Board (PCB), it was then placed at the bottom of the coil, below the STM position. The PCB-Hall sensor system is shown in Fig. 2.4, along with the resistances between the electrodes in Tab. 2.1. We had to calibrate the hall probe to establish a resistance versus B field relation, and to know what is the resistance value for a truly $B = 0$ T (before any field was applied). The calibration curve is shown in Fig. 2.5.

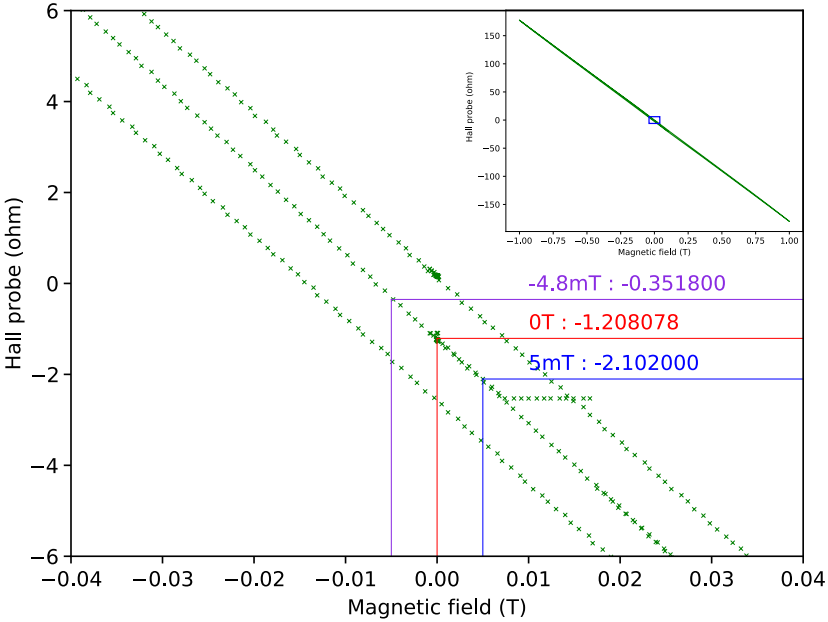

Figure 2.5: Calibration curve of the R vs B relation: Inset shows the ramping of the magnetic field and evolution of the Hall sensor resistance, following $B = 0$ T $\rightarrow$ 100 mT $\rightarrow -1$ T $\rightarrow 1$ T $\rightarrow -1$ T $\rightarrow 0$ T (value displayed by the electronic controller). The main figure is a zoom in the region from -40 mT to 40 mT from (a) (indicated by the blue rectangle). The coil has a hysteresis generating remanent field, even when the electronic controller displays a field of 0 T.

2.5 Auger Electron Spectroscopy

AES is used to study the composition of the surface of samples [80, 81]. It can probe the surface composition up to 10 ML. To do so, an electron gun is used to send electrons toward the sample to analyze. A sweep provider is used to accelerate them at a given energy. These electrons will create a hole in one of the core shell of the atoms on the surface. This hole will be filled by an outer shell electron, releasing energy. This energy can be coupled to another outer shell electron and release it free at a given kinetic energy according to:

$$E_{kin} = E_{core} - E_B - E_C \,, \tag{2.1}$$

with E_{core}, E_B and E_C the energy of the core state, the shell energy of the decaying electron and the bounding energy of the emitted electron respectively. The kinetic energy of the emitted electrons can then be measured with the help of an energy filter and an electron multiplier. A given range of energy of the incoming electrons is probed with the help of a sweep provider. For a given material, the intensity of the signal can then be plotted against the energy of the detected electrons, and characteristic peaks will be seen in the intensity, allowing to identify the material on the surface.

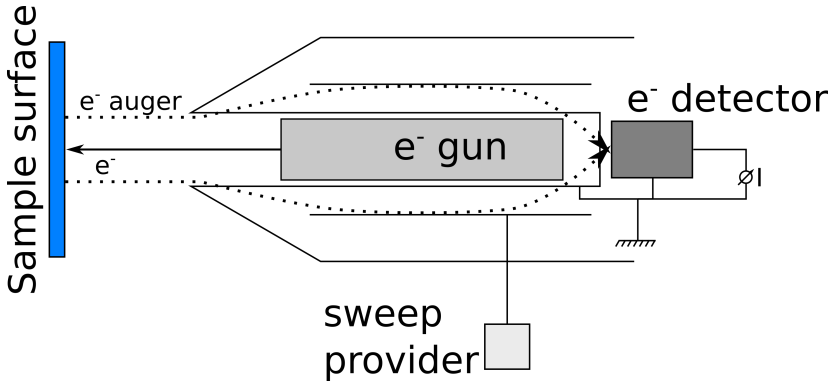

Figure 2.6: AES Schematic: Electrons are accelerated toward the sample. The energy of the electrons that are scattered by the sample is measured, and the signal amplified by the electron detector. Adapted from [80].

3 Study of Co sub-monolayer deposited on Ru(0001) surface

The motivation of this chapter is to investigate the superconducting properties of Ru(0001), and Co sub-monolayer (sub-ML) on Ru(0001). In this chapter, we first introduce in more details the cleaning of the Ru(0001) sample, the Co sub-ML deposition and the different type of islands we observed depending on the cleaning and deposition conditions. We then investigate how Co affects the superconductivity of Ru(0001), and reversely how superconductivity of Ru transfers to the Co sub-ML. We also investigate whether the magnetic ground state structure of Co/Ru(0001) is affected or not by the superconducting state of the substrate, and if we can form magnetic skyrmions and retrieve the SC state. Ultimately, we want to know if this coexistence lead to the emergence of MZS inside the SC gap of the sample.

3.1 Ru(0001)

3.1.1 Surface preparation and cleaning

Ru contains carbon impurities that do not affect the electronic properties of the overall surface in a meaningful way. Yet, it is important to remove as much of these impurities from the surface of the Ru sample for Co deposition. To obtain a clean enough flat surface of Ru(0001), we alternate sputtering/annealing cycles with annealing of the sample in clean oxygen atmosphere. First, the sample is sputtered for 10 to 30 minutes with Ar^+ ions, with a sputter current measured at the sample of 4.5 to 10 μA. The sample is then annealed using HV emission to a temperature $T = 1500 - 1700$℃ to make the surface flat again. It is important for the sample to reach at least 1400℃, otherwise flatness cannot be achieved from the rough surface generated by sputtering. Repeating these operations two or three times is enough to get a clean and flat surface, but it

is not enough to remove carbon contamination [82]. The carbon atoms are in the bulk of the sample, and removing atomic layers with sputtering does not affect the carbon concentration on the surface, but reveals the impurities buried in the bulk.

To remove carbon impurities from the bulk, the sample needs to be annealed in pure oxygen atmosphere [83]. Two workflows have been tried, results from both of which are shown in Fig. 3.1, and both showed similar and satisfying results. Yet, as it will be shown below, for equally good surface cleanness, the second method is preferred as it requires less preparation time:

- The first way is to continuously heat the sample for several hours in pure oxygen atmosphere. With our setup, by cooling down the manipulator using liquid nitrogen, it is possible to reach temperatures of the sample up to 1100℃. Like this, we can keep the sample hot for a long time without overheating the manipulator. Two problems arise when this method is used: The filament used to heat the sample is likely to break during the process, as it is in oxygen atmosphere and can be submitted to high currents. Besides, most of the manipulator is cooled down to very low temperature, and acts as a cryopump for the oxygen. It is therefore necessary to wait that the manipulator reaches room temperature again for the gas to desorb, which can take several hours. This operation has to be done several times to cumulate at least 8 hours of annealing in oxygen atmosphere to observe significant reduction or carbon impurities on the surface. Fig. 3.1 (a) and (b) show the Ru(0001) surface after a full cleaning cycle of 2 hours, without waiting and with waiting for the manipulator to warm up to room temperature, respectively. Fig. 3.1 (c) shows the surface after 8h30 cumulated oxygen annealing time.
- The second way is to heat the sample slightly higher than the previous one, with temperatures ranging from 1200℃ to 1300℃, still in oxygen atmosphere but without liquid nitrogen cooling the manipulator. To avoid any unwanted rise of pressure in the chamber, or temperature of the manipulator, compressed air flow is used to regulate the manipulator temperature. This reduces the time one can keep the sample hot, but the sample temperature being higher, the diffusion of the carbon impurities is more efficient, and it makes it possible to reach the desired purity level faster. Furthermore, the manipulator is not cooled down to cryogenic temperatures. Therefore, no waiting is needed after a

cycle, except the time needed for the manipulator to cool down to room temperature again (~ 10 min). Fig. 3.1 (d) shows the surface after 4 cycles of the second method.

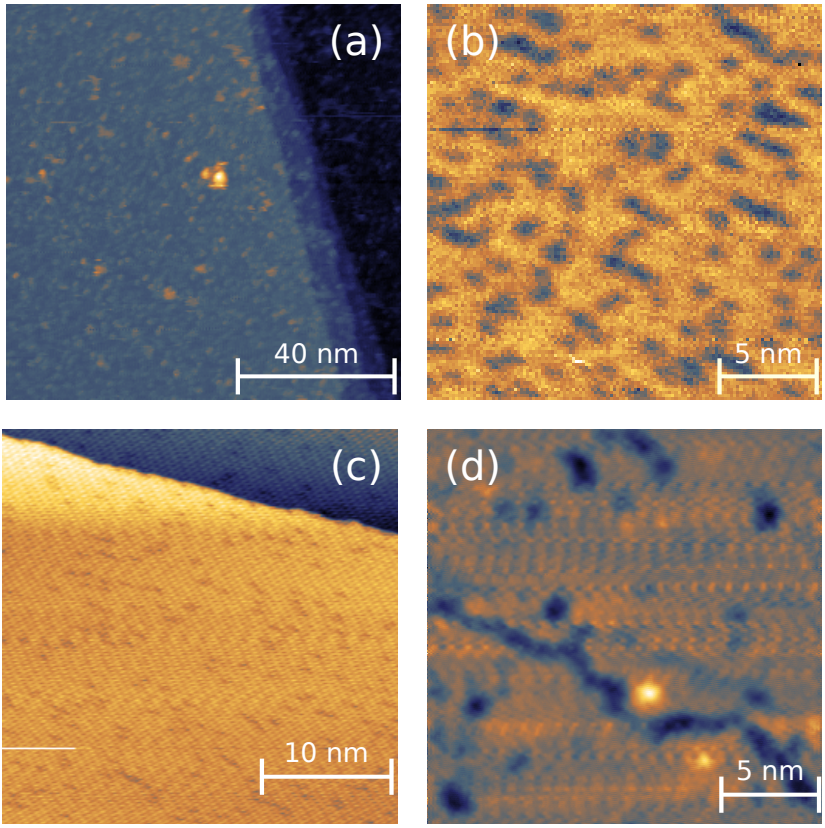

Figure 3.1: Comparison between cleaning methods: Topographic images of (a) Ru(0001) surface after 2h effective oxygen annealing time (first method) without waiting for the manipulator to reach room temperature before measurement. I = 2.45 nA, U = 1 V. (b) same surface after one sputtering cycle with coverage estimated at 22%. I = 1 nA, U = 30 mV. (c) Sample after 8h30 effective oxygen annealing time with carbon coverage estimated at 16%. I = 1 nA, U = 100 mV. (d) sample after 4 short oxygen annealing cycles (second method) with coverage estimated at 9%. I = 1 nA, U = 1000 mV.

By masking manually the observed carbon surface impurities in gwyddion [84], we were able to determine that for good deposition condition, maximally 20% of the surface coverage is allowed (that is, the area of the mask in an image should not represent more than 20% of the total image area). Above this value, the deposition results become uncertain and increasing the carbon surface concentration rapidly decreases the deposition quality. By repeating oxygen annealing cycles for several hours (first method described above) we were able to bring this concentration down to 16%. Using the second method is much more efficient, as we could reach concentration as low as 10%. All carbon concentration estimations were done locally by analyzing area from 400 nm^2 to 900 nm^2. The carbon concentration being uniform over the whole sample surface, the values measured on different locations of a given sample do not differ by more than 0.5%. Estimating the diameter of the observed carbon atoms is not straightforward: the impurities do not have sharp edges, and post treatment of the data for noise reduction of background removal may alter the quality of the image such that manual masking cannot be performed on some images. In both described workflows, after all the oxygen in the chamber has been pumped away, it is necessary to flash the sample to at least 1200℃ to remove the remaining layer of O_2 and RuO on the surface. Flashing the sample higher than 1400℃ is not advisable, as it makes the carbon impurities from the bulk segregate to the surface again, making the oxygen annealing step useless. From this point, the sample can be carried into the STM to check if the desired purity is achieved, or deposition can be done right away (although it is necessary to proceed first to a degassing phase of the evaporation rod, as oxygen created an oxide layer on it, the sample might not be as pure as wanted).

3.1.2 Superconducting properties

It has been observed that ruthenium is a superconductor [85]. Previous measurement estimated the critical temperature to be $T_c = 470$ mK. It is also known to be a type I superconductor with a critical field of $B_c = 5$ mT [85]. Yet, the SC gap has not been measured. It is critical to use a dilution refrigerator to perform this measurement, as T_c is lower than the temperature reachable with only a LHe cryostat or a JT refrigerator. Using our refrigerator, we could measure the superconducting gap, as well as its dependency with the temperature, to confirm the conventional BCS superconductor nature of ruthenium. The tunneling spectrum and the fitting of the data are shown in

Fig. 3.2 (a). We brought the temperature down to $T = 25$ mK, and performed STS measurement to observe the SC gap. We then fitted the dI/dU signal using a BCS gap fit. We confirmed the conventional BCS superconducting nature of the Ru by slowly increasing the temperature from 25 mK to T_c, and measuring the gap at regular steps. We could then plot the fitted values of the gap versus the temperature, and fit the obtained graph using the relation:

$$\frac{\Delta\,(T)}{\Delta_0} = \tanh\left(1.74\sqrt{\frac{T_c}{T} - 1}\right), \tag{3.1}$$

with $\Delta_0 = \Delta(T = 0)$. The experimental data and the fit are shown in Fig. 3.2 (b). The results of the fit gives us a critical temperature of 583.8 mK, which gives an error of about 20% compared to reported value in [85], and $\Delta_0 = 71.9$ µeV. The latter can be compared with the calculated value given by $\Delta = 1.76 k_B T_C = 71.4$ µeV. Both values match reasonably well with the expected values, indicating that Ru is indeed a conventional BCS superconductor.

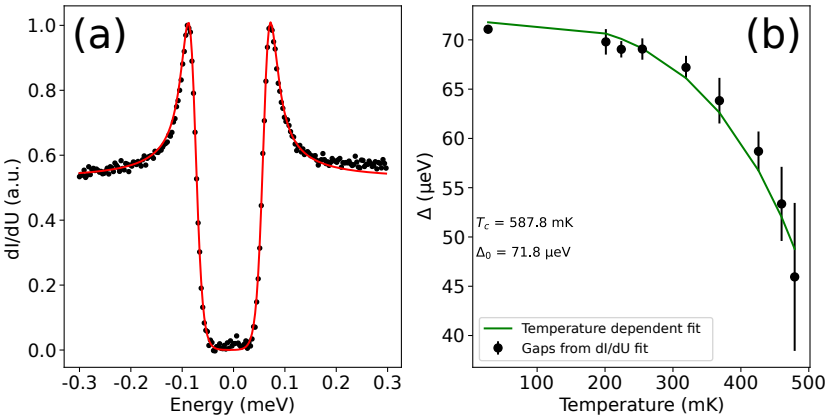

Figure 3.2: SC gap of Ru(0001) and temperature dependence of the gap: (a) Plot of the dI/dU spectra measured at 25 mK (black dots) and the corresponding BCS fit (red line). $I = 500$ pA, $U = 300$ µV, $U_{mod} = 5$ µV. Fit results: $\Delta = 70.7 \pm 0.1$ µeV, $T = 83.8 \pm 0.8$ mK (b) Temperature dependence of the resulting gaps (black dots), together with a fit to the data (green line). Both results indicate that Ru is a conventional BCS superconductor.

3.1.3 Ramping the magnetic field and restore superconductivity

During the experiment, a magnetic field needs to be applied in order to form the desired skyrmions. As explained in the next sections, a magnetic field of ±250 mT needs to be applied to form the skyrmions, and can be ramped down to zero afterward with the skyrmions living on the surface. Unfortunately, after applying a magnetic field and then ramp it to zero, a residual field remains applied to the sample, keeping it in the normal state. We first thought this was the remanent field of the coil, but it became clear that the controller's PID was overshooting before stabilization, and was therefore applying a field of a few mT in the opposite direction. This was detected and later overcame by installing a hall probe below the STM body [78, 79], allowing us to probe the magnetic field at this position with great precision. By ramping the magnetic field using a very low slew rate of 1 mT/min or manually using an external current generator, we are able to restore the superconducting state of the Ru sample. This is achieved by both controlling the value of the hall probe's resistance, and by continuously measuring the LDOS at the quasiparticle state energy. Doing so, we can easily discriminate the normal state from the superconducting state. This procedure is displayed in Fig. 3.3. The bias voltage is placed at the value at which the quasiparticle peak has been measured before applying the magnetic field, and the differential conductance signal is continuously measured at this energy. The field is then ramped slowly in the wanted direction, until a sudden jump is seen in the dI/dU signal, indicating that the sample is superconducting. The field is immediately maintained at its current value. It often happens that the superconducting state does not hold more than a few seconds or a minute, in which case another jump is observed in the dI/dU signal, and this operation needs to be repeated until a stable superconducting state is obtained.

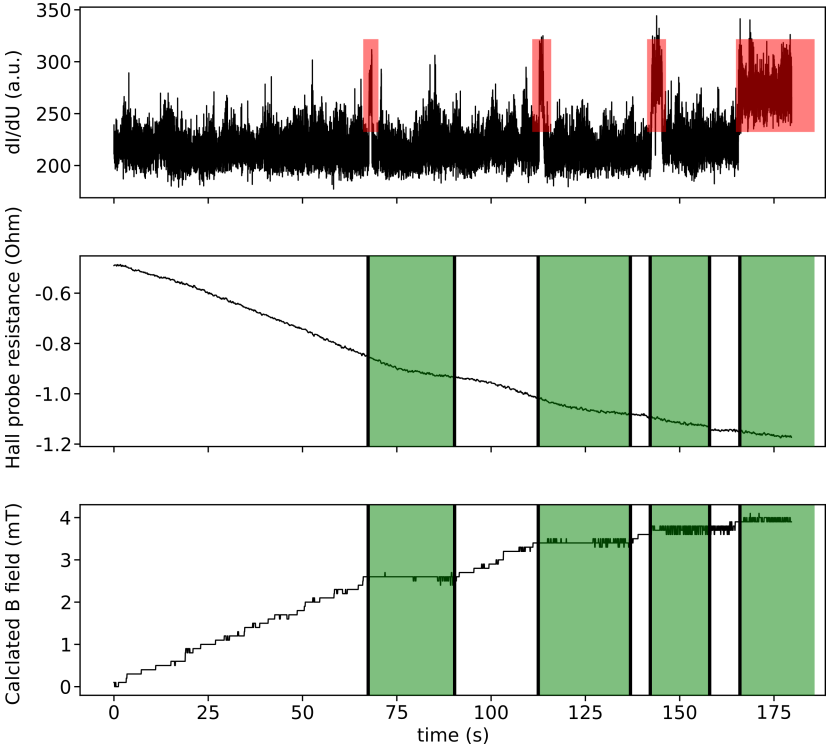

Figure 3.3: Evolution of the differential conductance as a function of applied magnetic field. Upper panel: differential conductance measured at the quasiparticle state energy $E \approx 70$ µeV over time. The red boxes indicate the time interval during which the sample is superconducting. Middle panel: Hall probe resistance measured over time. Lower panel: magnetic field indicated by the controller. The green regions show the time interval during which the magnetic field is maintained by the controller. As one can see, a lot of S-N and N-S transitions can be observed before a stable transition into the super conducting state is reached. If one stops the ramping at this point, it is possible that the field keeps evolving before total stabilization. Even though the field is not supposed to evolve anymore, the Hall probe resistance keeps evolving and the sample still experiences transition from SC to N.

3.2 Co/Ru(0001)

3.2.1 Cobalt deposition and phases on ruthenium surface

In previous studies, it has been shown that Co/Ru(0001) arranges in different ways depending on the temperature of deposition, and/or depending on the post annealing temperature [86]. We discovered that Co sub-ML can exhibit different stackings: the regular hcp stacking for which the Co atoms follow closely the packing of the underlying Ru atoms, and a new stacking, which is similar to an already observed phase of Co nanoparticles and has a structure similar to the β-phase of Mn [87, 88]. We believe that temperature difference between the deposition attempts plays a minor role, because for two similar deposition conditions, the sub-ML display very different behaviors. Instead, we believe that the carbon concentration plays a much more important role in the formation of this new phase, as we will demonstrate in this section. Furthermore, it appears that maintaining a constant temperature plays a bigger role than placing the sample at the same potential as the evaporation rod, as it will be discussed below.

While the second monolayer of Cobalt has already been studied in the past and is known to be ferromagnetic [82], we found no study for the new arising phase. On topographic images, it appears lower than the known hcp-Co stacking. On samples with low carbon concentration, small to medium size clusters could be observed, often included in hcp-Co islands. Yet, if the carbon concentration is too high, this new stacking becomes dominant and no hcp-Co island can be observed. We concluded, from atomically resolved images, that this new stacking was most likely to be the ε-Co stacking [87]. The phase shows a large unit cell in the form of a $(\sqrt{10} \times \sqrt{10})$-reconstruction. The basis vectors have a length of 939 pm. This unit cell agrees well with the 2d unit cell of (111) bulk ε-Co of 860 pm [87] as shown in Fig. 3.4 (a). We could not observe any non-collinear spin structure on it. In topographic images of perfectly formed islands, the rim of the island appears higher than the core of the island. This is attributed to a relaxation from ε to hcp stacking. This is coherent with the fact that, on better prepared samples, the ε stacking was never observed as single islands, but as clusters included in the core of bigger hcp stacked Co islands. Another hint that this is indeed the case lie in the proximity effect between ε or hcp phase and Ru(0001) (detailed in section 3.2.4). Fig. 3.4 (a) shows a dI/dz map of a surface location exhibiting free

Ru(0001), hcp-Co and ε-Co, while Fig. 3.4 (b) shows the crystal structure of the ε-Co lattice cut in the (111) direction. Fig. 3.4 (c) shows the cross-section for both islands in the inset.

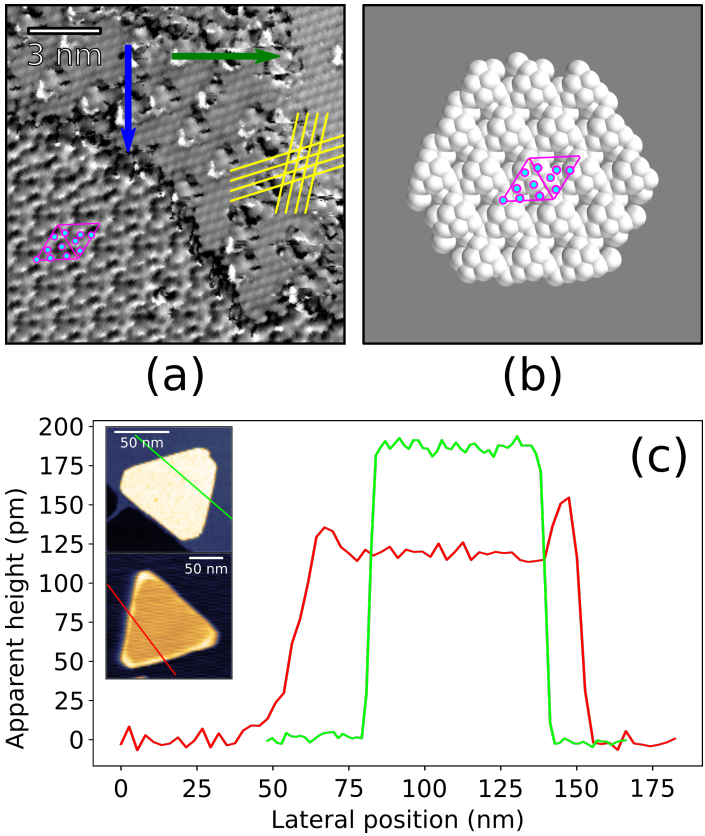

Figure 3.4: ε-Co and hcp-Co: (a) dI/dz image of the different stacking of Co near a Ru(0001) step edge (I = 1 nA, U = 100 mV, z_{mod} = 20 pm). The green and blue arrows show the interface between Ru/hcp-Co and hcp-Co/ε-Co. The yellow lines follow the lattice of Ru and hcp-Co to guide the eyes. (b) (111) cut of ε-Co phase. The pink lines show the unit cell. Light blue dots show the positions of the atoms. The positions are repeated in (a) for comparison. (c) Apparent height of ε stacking (red) and hcp stacking (green). Two peaks are visible at the edge of the cross-section of the ε island. The inset shows topographic images of the two different stackings of Co sub-ML on the Ru(0001) surface recorded at (I = 1 nA, U = 1 V), with the lines indicating where the cross-sections have been made.

Co sub-ML was deposited using MBE. The evaporator used for the deposition is a commercial evaporator sold by Specs [89]. A 99.99% pure cobalt rod sold by ChemPur is placed in the evaporator and HV is applied to it (typically 900 V to 1 kV). The current in the filament of the evaporator is then increased until the flux reaches the desired value. Typically, depositions were made using 10 to 11 mA emission and a flux of 15 to 30 nA for a deposition time of 35 to 45 s. For newly installed or vented rod, it is necessary to degas it over night at low flux (1 to 2 nA). For the deposition, a shutter is open to let Co atoms fly toward the sample surface, where they are adsorbed. During the deposition, the sample is softly annealed below 200 ℃ using thermal radiation of the filament underneath it. Since the sample is heated, the adatoms diffuse and form islands on the surface. Two deposition processes were tried.

The first process is used to prevent accelerated atoms to penetrate the sample below the surface, thus modifying the surface structure and state. To do so, HV with value equal or above the potential of the evaporation rod is applied to the sample during the deposition. Since the sample and the rod are at the same potential, most of the ions are stopped when they reach the surface. Therefore, they do not go below the surface and just adsorb. During the procedure, it is necessary to stop the heating current of the sample flowing in the filament, otherwise an emission current will flow and heat the sample above the desired value, This method was used because samples prepared with the second method (explained in the next paragraph), although exhibiting perfectly formed islands, were not exhibiting spin contrast. We believed that it was due to the ions that penetrated the surface, forming defects and altering the interaction between the surface and the magnetic Co adatoms. These sub-surface defects are not visible in topographic images (Fig. 3.5 (a)) but they are visible in dI/dU maps (Fig. 3.5 (b)). It later became clear that the second method was also suitable to prepare samples with the desired properties, as atoms penetrating the surface would in fact not alter the surface properties significantly. The underlying reason that caused the spin contrast not to be visible later appeared to be a tip DOS incompatible with TAMR observations. This first method was abandoned since only a few samples were successfully prepared with the desired properties. The reason is that, when the heating current of the sample is cut, the voltage applied to the sample and the shutter of the evaporator open for deposition, the Ru sample cools down by radiations. This cooling process depends on too many parameters and cannot be well controlled, nor monitored. Hence, the formation of islands cannot be predicted, and malformed islands are likely to appear on the sample.

If on top of this, the carbon concentration is not optimal, the ε stacking will be dominant and no experiment can be carried out on the magnetic structures (see next paragraphs). Unsuccessful and successful samples are shown in Fig. 3.5 (a), (b), (c) and (d), (e), respectively. The new ε phase is visible in Fig. 3.5 (c).

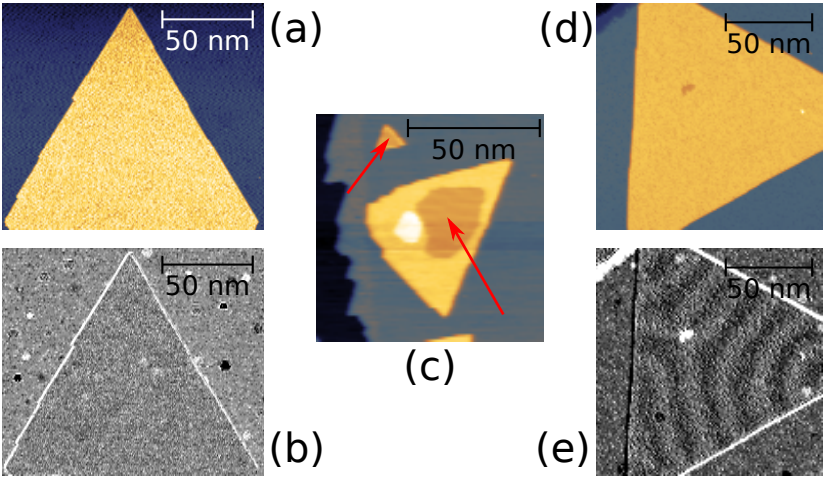

Figure 3.5: Comparison of islands observed on the surface with the different methods: (a) Topographic image of a single Co island, obtained with the second method. On the topography, no defect can be noticed, while bright and dark dots can be seen on (b) the dI/dU map. Yet, no TAMR contrast is visible. While it was first attributed to the underlying defects, it became clear later that this was likely due to the tip. (a) and (b) were recorded with $U = -350$ mV, $I = 3$ nA, $U_{mod} = 50$ mV. (c) Typical island obtained with the first method and insufficient carbon atoms removal, resulting in unwanted ε phase of Co (darker area in the core of the triangular island and small island in the top, indicated by the red arrows). The regular hcp phase is present, but a second layer starts to appear, and large inclusions of a newly observed phase reduce the surface of hcp-Co island, thus preventing us to make measurement on the magnetic structure if this surface is too small. $U = 1$ V, $I = 1$ nA. (d) and (e) display a nicely formed island and the corresponding TAMR measurement (respectively) exhibiting a magnetic structure (bright and dark stripes). $U = -350$ mV, $I = 2$ nA, $U_{mod} = 50$ mV.

The second method simply consists of depositing Co sub-ML while the sample is maintained at a constant temperature via the radiations from the filament. Although the exact temperature cannot be monitored because it is main-

tained below 200℃, a given set of parameters for a given filament gave us reproducible results. That is, the size of the islands could be controlled from one sample to the other by increasing or decreasing the current in the filament. A reference sample is, of course, needed every time the filament is changed, since a given set of parameters would not result in the same sample temperature. Yet, this method is simpler because fewer manipulations are necessary. It is also more reliable and provides better control on the deposition parameters.

3.2.2 Investigation of the magnetic structure of hcp Co/Ru(0001) and skyrmion formation

In a previous work [16], spin-polarized STM measurements and density functional theory (DFT) calculations have been combined to explore the ground state properties of Co/Ru(0001) and it was shown that skyrmions were stabilized by a vanishing effective anisotropy in combination with a small DMI. This particular ratio of magnetic interactions makes Co/Ru(0001) a prototypical soft ferromagnet in which isolated skyrmions have been stabilized down to zero external magnetic fields.

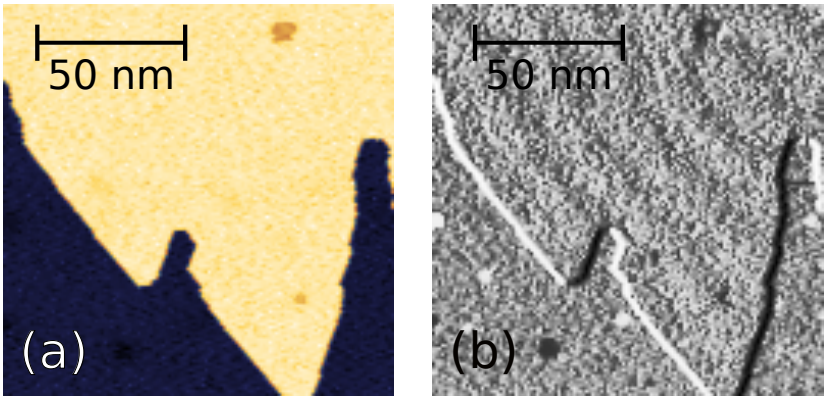

Figure 3.6: Ground state spin texture of the Co/Ru(0001) system: (a) topography of a Co island. (b) dI/dU map of the same island, showing the spin texture. On the Co island dI/dU maps, bright and dark stripes correspond to in-plane and out-of-plane magnetization, respectively. $I = 1$ nA, $U = -350$ mV, $U_{mod} = 50$ mV.

Here, we study this magnetic structure on isolated or almost isolated islands. We also report a constraint on the size of the isolated island for the skyrmion formation. The ground state spin-spiral texture can be seen in Fig. 3.6. Since we use TAMR to image the spin texture, the observed pattern has a period two times smaller than the period of the actual texture, since we cannot differentiate spin with up or down direction.

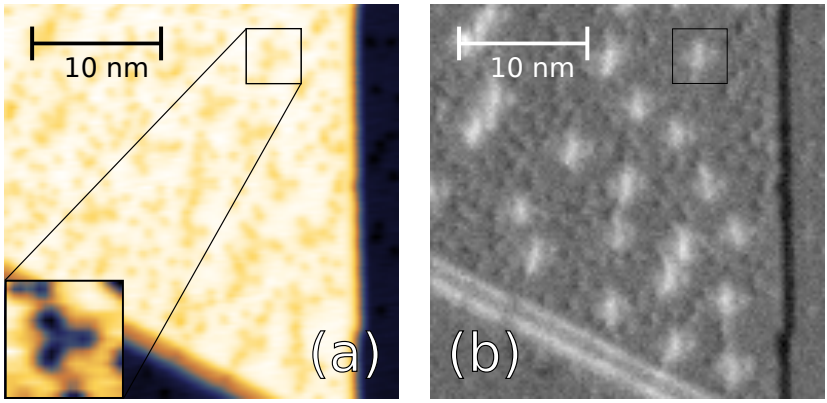

Figure 3.7: RuCo impurities: (a) Topographic image of an island exhibiting triangular impurities thought to be Ru atoms included in the Co layer. The inset is a zoom of the region framed by a black box showing the 3 atoms structure of the impurity. (b) dI/dU map of the island shown in (a). The image map was made at the energy where the TAMR contrast is normally visible. The impurities appear brighter and do not allow the user to see TAMR contrast. For both images $I = 1$ nA, $U = -350$ mV, $U_{mod} = 50$ mV.

On several samples, we could detect the presence of a new kind of impurities on certain islands, which would effectively make it locally impossible to see any magnetic contrast. This is because, at the energy at which the TAMR contrast is obtained, the LDOS on these impurities is high, resulting in very "bright" spots on the dI/dU map. The TAMR signal being small in comparison, we could not see the underlying spin texture. These impurities always appeared in the shape of a triangle defined by three dots, presumably Ru atoms segregating in the Co island. This assumption is further sustained by results obtained while studying the proximity effect between Ru(0001) and Co (see section 3.2.4). Unfortunately, we could not link the appearance of these impurities to a preparation parameter. Indeed, they would or wouldn't

appear in one to another sample with identical preparation conditions. Furthermore, on the same sample, some islands would exhibit such impurities while other islands of the same region (neighboring islands) would be found to be free of impurities. This strongly suggests that the appearance of this impurities comes from the local structure of the sample, and therefore cannot be controlled reliably. A topographic image of an island containing these impurities as well as a dI/dU map of the island are shown in Fig. 3.7 (a) and (b).

Once an island that shows a spin spiral has been found, we can progressively apply magnetic fields to the sample in order to form skyrmions. The evolution of a spin spiral until the formation of skyrmions is shown in Fig. 3.8. It should be noted that, in order for this process to work properly, a triangular island should have a minimum lateral dimension of 80 nm; although it is possible to form skyrmions on islands with lateral dimension as small as 50 nm, it remains a very hard process. The field is ramped at a rate of 50 mT/min from 0 T to 250 mT, field at which the skyrmions will form. If wanted, it is possible to ramp the field by steps of 50 mT to make a dI/dU map between each step and survey the spin spiral evolution, allowing to identify which regions of the structure are pointing up or down.

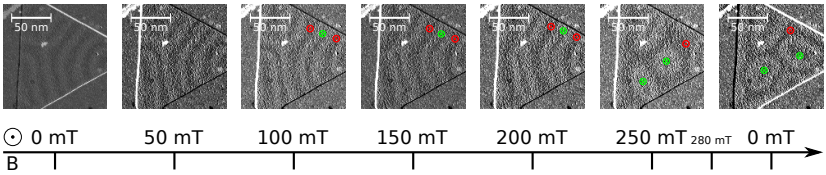

Figure 3.8: Skyrmions formation: dI/dU maps recorded at the TAMR contrast energy. The field is ramped up from 0 to 280 mT, then down to 0 again. An image was recorded every 50 mT. The deformation of the spin-spiral is visible from $B = 100$ mT, the direction of the out-of-plane spins are indicated by red ⊙ and green ⊗ (parallel and antiparallel to the magnetic field, respectively). Skyrmions start to form at 250 mT. For each image $I = 2$ nA, $U = -350$ mV, $U_{mod} = 50$ mV.

3.2.3 Skyrmion size dependency with magnetic field and annihilation

This section is adapted from a published article [90]. Understanding the dynamics of skyrmions is of first importance, as manipulating them as single

objects is a goal for the realization of skyrmionic systems. More specifically, it is important to know the interactions involved in this dynamics and their relative scales. With this motivation, we here report the observation of a collapse field B_c for single skyrmions in Co islands on Ru(0001). We experimentally determined B_c for skyrmion annihilation at minimal thermal activation at $T \approx 30$ mK [72]. These experimental results are compared with numerical estimations of B_c based on ab-initio parameters made by Bertrand Dupé from Liège and Patrick Bühl from Mainz. We found a good agreement between experimental results and simulation, giving us insights on the interactions playing a role in the stabilization of the skyrmions.

To study the size of the skyrmions depending on the magnetic field and the field at which the core magnetization will reverse and unwind the skyrmions back into the ferromagnetic state (which we call collapse field), a magnetic field is applied in the opposite direction to the magnetic moment of the skyrmion center by steps of 50 mT and the skyrmions are imaged between each step. The Zeeman energy leads to a compression of the skyrmions [91–93], which size can then be fitted. When the magnetic field reaches the critical value B_c, the skyrmions will collapse and the islands hosting the skyrmions undergo a transition into the ferromagnetic state. This process has already been studied in the continuum limit; in this ideal case the collapse of skyrmions occurs when their radii shrink down to zero [94]. On a finite lattice of magnetic atoms, the radius reaches a finite value before the collapse [92, 94]. The collapse of skyrmions is associated with an energetic barrier and is usually studied as being thermally activated within the framework of transition state theory [95].

Transition state theory investigates high energy states, also called saddle points. This is done via nudged elastic band (NEB) calculations [96]. In magnetism, NEB has been extended to take into account the constant size of the magnetic moments and is known as the geodesic nudged elastic band (GNEB) [97, 98]. This method has been used extensively to study the thermally activated probability of skyrmion collapse in strong ferromagnets such as Co/Pt(111) [92] and in ultrathin magnetic films such as Pd/Fe/Ir(111) [99–101]. Yet no reports explore this transition at low temperature. This critical for the study of the saddle point, because it removes the possibility for the skyrmions to undergo the transition into the ferromagnetic state via thermal activation. Although the transition between the skyrmion lattice and the ferromagnetic phase has been measured at 4 K, the saddle point could not be explored in these cases because of the too large value of the collapse field [17, 91]

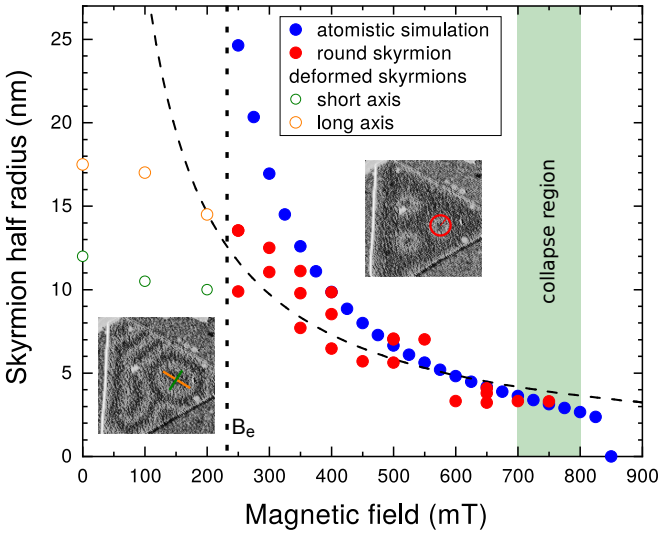

Figure 3.9: Skyrmions' size dependency and collapse with magnetic field: Theoretical (blue filled circles) values of $\sigma/2$ of the skyrmion versus applied magnetic field in Co/Ru(0001) together with the experimental values for round skyrmions $B > B_e \approx 230$ mT as illustrated in the right inset. At $B < B_e$, the skyrmions are elongated and both the radii along the long (orange) and short (green) axis are plotted as illustrated in the left inset. The black dashed curve is a fit to a/B. At fields in the shaded green area, annihilation of skyrmions was experimentally observed. The insets are differential conductance maps (white level proportional to dI/dU) of 130x130 nm, $I = 2$ nA, $U = -350$ mV, $U_{mod} = 60$ mV. left inset: $B = 0$ mT, right inset: $B = 400$ mT.

As we described before, we form magnetic skyrmions by applying a magnetic field B normal to the surface. The spin spiral is deformed until two in plane magnetized stripe joins together to transform into an isolated skyrmion, which radius will depend on the applied magnetic field. Again, we exclusively used the TAMR signal to determine the shape of the skyrmions for later fitting to avoid magnetic dipole interactions between the tip and the sample, and tracked the skyrmion dimensions as a function of magnetic field as shown Fig. 3.9. Skyrmions were formed by first applying 250 mT. Then, the B was ramped down until the value displayed by the controller was

0 T, i.e. to the remanence of the superconducting magnet (≈ 7 mT) and metastable skyrmions remained. After the skyrmions were formed, we again increased the magnetic field by steps of 50 mT to study the evolution of the skyrmion dimensions as function of B. It should be noted that for field below $B = 230$ mT, skyrmions are not round objects but rather elongated and curvy, depending on the hosting island geometry and the spin spiral reformation during the ramping of the magnetic field to 0 T. Such structures are shown in Fig. 3.10 (a) and (b). We keep speaking of skyrmions in this case because, even if they do not respect rotational symmetry, their winding number is the same as round skyrmions, and they can continuously be deformed in one another, therefore keeping the topological protection for both objects. The fact that, in absence of magnetic field, skyrmions are not round anymore is due to their tendency to reform the spin-spiral ground state. This is prevented by the topological protection of the skyrmions. On smaller island, i.e. under stronger constraint from the edges, the skyrmions were most of the time slightly elongated with an elliptical shape.

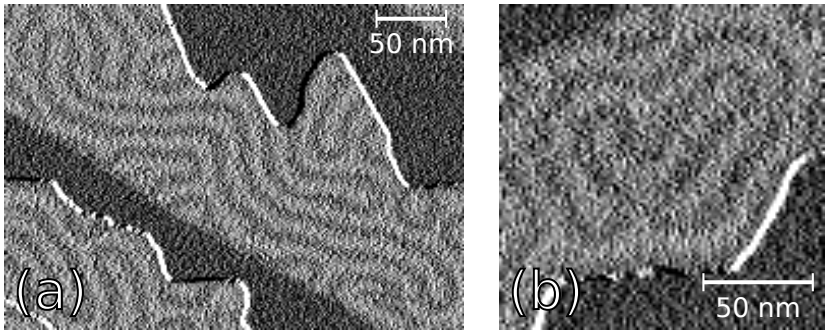

Figure 3.10: Peculiar skyrmion-like structures at $B = 0$ T: $I = 1$ nA, $U = -350$ mV, $U_{mod} = 50$ mV.

Thus, for fields below 230 mT, we determined the largest and smallest axis of the elongated skyrmions instead of their radius. These quantities are indicated in orange and green lines in the left inset and open circles in Fig. 3.9. At fields higher than 230 mT, the skyrmions become rounder, indicating that the influence of the neighborhood becomes negligible in comparison to the Zeeman interaction (see right inset of Fig. 3.9). To fit the skyrmions' size, we work under the assumption that the orientation of the magnetic

moments evolve linearly between the core of the skyrmions and their edge. This vision is incorrect, and no analytical function describes this evolution. A popular vision is to approximate the lateral evolution of the orientation of the magnetic moments with two domain walls and apply rotational symmetry to it [91]. In our case, the linear approximation is justified by the fact that DMI is rather small. The dI/dU signal varies as $\cos^2(\theta)$, with θ being the polar angle. We therefore use the following function to fit the skyrmions' radii [102]:

$$dI/dU = \begin{cases} \cos^2\left(\pi\frac{\rho}{\sigma}\right) \text{ if } \rho \leq \sigma \\ 0 \text{ otherwise} \end{cases}, \tag{3.2}$$

where ρ is the lateral distance from the center of the skyrmion, and σ is the radius of the skyrmion. With this definition, it means that, on a dI/dU map, the radius of a skyrmion is taken to be two times the distance from the center of the skyrmion to the maximum brightness, that is the distance between the out-of-plane and the in-plane magnetic moments. A simulation of both the TAMR and TMR signals we obtain by using this approximation are shown in Fig. 3.11 (a) and (b). For both simulations, a circle is drawn at the position of the in plane magnetization, i.e. half of the fitted radius also indicated with a line. For the TAMR simulation, this circle superimposes with the brighter positions as described above. For the TMR simulation, the orientation of the tip's spin is taken to be parallel to the skyrmion's core magnetization. A fit made on a real skyrmion is shown in Fig. 3.11 (c).

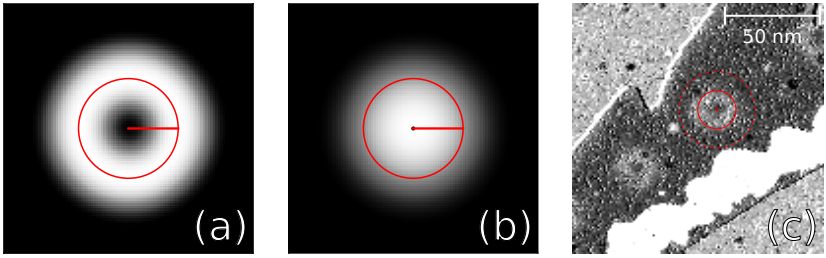

Figure 3.11: TAMR and TMR simulations and experimental skyrmion fit: (a) TAMR profile of a skyrmion simulated using equation 3.2. (b) TMR profile of the same skyrmion. (c) dI/dU map of Co/Ru(0001) displaying two skyrmions. The right skyrmion is fitted using the model shown on (a). The inner and outer circles show the fitted $\sigma/2$ and σ. Parameters for (c) are $I = 2$ nA, $U = -350$ mV, $U_{mod} = 60$ mV.

At higher fields, analytical models predict the radius of isolated skyrmions to scale as $1/B$ [103, 104] and has been experimentally verified [17]. This tendency has been fitted to the high field experimental data and is shown in Fig. 3.9 (black dashed line). For each step of the magnetic field ramp, we fitted the dI/dU contrast via eq. (3.2) and plotted the obtained half-radii values against B in Fig. 3.9. The results of the fits for each magnetic field are plotted as red circles in Fig. 3.9 (c).

At lower fields, we determined the length of the short and long axis of the not round skyrmions by hand. These are shown as unfilled green and orange circle in Fig. 3.9 (respectively). At these low field values and near the field at which we can fit the skyrmions as circular objects, the data scatter and do not follow the $1/B$ tendency, anymore. This is easily explained by the mentioned elliptical instability and the skyrmions' sensitivity to the near spin-spiral phase. As the field increases, these effects become marginal and the radius of the different skyrmions converges to the same value.

It is predicted that, at the saddle point, the magnetic moments align in-plane to create a vortex whose size is only several unit cells [98]. Since the skyrmion is a topologically protected structure, the only way for it to unwind into the topologically trivial ferromagnetic state is to introduce a topological defect. Recently, the saddle point configurations were explored theoretically, and it was found that even when the magnetic interactions are described in the continuum limit, a skyrmion of finite size could be expected as the saddle point configuration [105]. For fields below B_e, the dependency in $1/B$ of the skyrmions' size breaks down, as the ground state is not an infinitely extended skyrmion [106] but the spin-spiral phase. For the elongated skyrmions, the short axis as defined before has a length of about 24 nm corresponding to a local periodicity of the spin-spiral of ≈ 48 nm. This is coherent with our expectation: at 0 field the system wants to restore its ground state, and the small axis of the skyrmion will therefore relax into a structure that has similar dimensions as the one of the spin-spiral ground state [16], while the long axis can extend as long as the constraints of the system allow. Skyrmion with long axis as long as ≈ 300 nm have been observed, as shown in Fig. 3.10 (a).

Of course, due to the system constraints, the long axis of the skyrmion will not diverge to infinity. At fields larger than B_e the round skyrmions are compressed, and the radii keep decreasing but stay finite until $B = 700$ mT. At this field, the collapse region is reached and individual skyrmions disappear by annihilating the topological charge, and do not reappear upon lowering

the field again. When the field reaches $B = 800$ mT all skyrmions have disappeared which shows that the collapse field B_c was reached at $B_c = 750 \pm 50$ mT. As all measurements are made at $T \approx 30$ mK, this collapse is not due to thermal activation. Moreover, during ramping the field, the tip was retracted such that an influence of the tunneling current on the skyrmion collapse was excluded. It should be noted that it remains unknown to this day if the skyrmion's transition into the ferromagnetic state can be done by tunneling between these two states. This would require time extensive specific measurements.

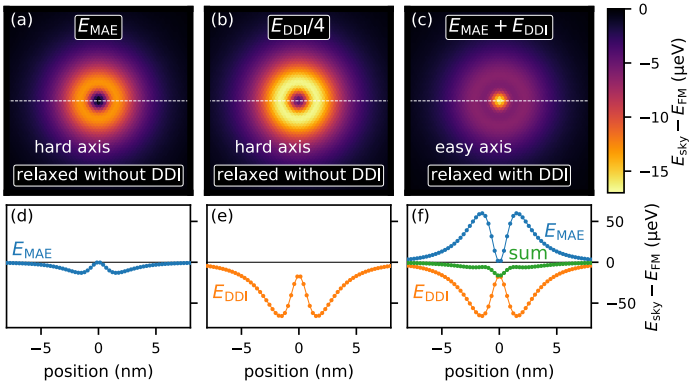

Figure 3.12: Energy density distribution with respect to the FM state at $B = 750$ mT: (a) and (b): The skyrmion was relaxed with an easy axis in-plane anisotropy of 13 μeV and without DDI: (a) MAE contribution and (b) DDI contribution. (c) skyrmion relaxed with both DDI and an easy axis anisotropy out-of-plane of 60 meV. (d), (e) and (f): radial energy density distribution showing the MAE (d), the DDI (e) and both contributions (f). The integral of (a) and (c) are of comparable magnitude with 13.8 meV and 11.8 meV, respectively. Taken from [90].

To investigate the interactions in play, calculations at the sadle point have been made by Bertrand Dupé and Patrick Bühl. In calculations, the saddle point configuration is easy to explore since the magnetic configuration can be constrained. We compared the experimental results with atomistic simulations made with the Spirit code [107]. The energy of the magnetic texture is described as:

$$
\begin{aligned}
E &= -\sum_{ij} J_{ij}\boldsymbol{M}_i\boldsymbol{M}_j - \sum_{ij}\boldsymbol{D}_{ij}\left(\boldsymbol{M}_i\times\boldsymbol{M}_j\right) \\
&- \sum_i M_s\boldsymbol{M}_i\boldsymbol{B} - \sum_i \kappa\boldsymbol{M}_{i,z}^2 \\
&- \sum_{ij}\frac{\mu_0 M_s^2}{4\pi}\frac{\boldsymbol{M}_i\boldsymbol{M}_j r_{ij}^2 - \left(\boldsymbol{M}_i\boldsymbol{r}_{ij}\right)\left(\boldsymbol{M}_j\boldsymbol{r}_{ij}\right)}{r_{ij}^5},
\end{aligned}
\tag{3.3}
$$

wihh J_{ij} the magnetic exchange interaction, $\boldsymbol{D}_{ij}$ the Dzyaloshinskii-Moriya vector, κ the magnetocrystalline anisotropy (MAE) and $\boldsymbol{B}$ the external magnetic field. The magnetic interaction parameters were obtained by DFT in a previous work [16], and are $J_1 = 13.1$ meV, $D_1 = 0.2$ meV, $\kappa = -0.013$ meV and $M_s = 1.8\mu_B$. With these parameters, the experiment was modelled by a periodic superlattice containing 1000×1000 magnetic moments on a hexagonal lattice with the Ru lattice parameter $a = 0.27$ nm. For each magnetic field B an isolated skyrmion was relaxed to its minimum of energy. The skyrmion radius was then fitted with eq. (3.2).

The radius of the skyrmion without the dipole-dipole interaction (DDI) was calculated as a function of the field (blue dots in Fig. 3.9), as in previous work [16]. Although the calculated radius decreases more steeply with increasing field than measured, it follows the same trend and matches well at fields higher than 500 mT. This agreement at higher field is what is needed, since the exploration of the saddle point is the goal here. The discrepancy at lower fields is easy to explain: the skyrmions observed experimentally are not isolated skyrmions. They are hosted on islands with size of the same order of magnitude than the skyrmions' size. The skyrmions being more densely packed, this leads to additional compression compared to the simulations. The atomistic simulations predict a collapse field of $B_c = 820 \pm 10$ mT which is in good agreement with the experimental value. It should be noted that all theoretical parameters were obtained from DFT, which makes the agreement between the atomistic simulations and the experiments extremely good. This is particularly remarkable as tiny modifications of the anisotropy on the scale of the DFT-accuracy result in drastic modifications of the skyrmion radii and B_c in this fragile regime of atomistic parameters.

Including the DDI demonstrates the delicate balance of atomistic parameters in this soft magnet. The DDI was evaluated in a magnetic configuration

that was minimized neglecting it (Fig. 3.12 a,b,d,e). The energy gain of the skyrmion compared to the ferromagnetic state through the DDI is more than 5 times the gain of the MAE. Nevertheless, qualitatively both distributions do not differ. The only exception is the non-vanishing energy gain at the core in case of the DDI. This is consistent with the common 2D interpretation of the DDI as shape anisotropy which can be absorbed into an effective magnetic anisotropy [108]. Due to the relatively large magnitude of the DDI in this system, the magnetic ground state changes drastically when the DDI is included. The background magnetization tilts in-plane in the experimentally investigated field range, and skyrmions in an out-of-plane background exist only in a small region around 1.5 T. In order to agree with the experiment, the MAE as smallest parameter with large theoretical uncertainty and similar impact was tuned to $\kappa = 0.06$ meV which approximately counters the energy gain through the DDI. While the shape of the energy gain from the effective anisotropy shifts towards the core when including the DDI and modifying κ (Fig. 3.12 c,f), the previous dependence of the skyrmion radius on the field is recovered. That is, the experimental results can also be described when including DDI, although a reasonable but arbitrary modification to the MAE is necessary.

Since DDI is not required to study the stability of skyrmions in ultra-thin films, the energy barrier has been explored without explicitly considering DDI in the vicinity of B_c via GNEB simulations [97] on a 400×400 grid as shown in Fig. 3.13. The simulations were initialized with the relaxed skyrmion profile for a given magnetic field. Along the reaction path, the skyrmion shrinks until it reaches the saddle point, which corresponds to the maximum of energy. The energy is maximal when the half radius reaches about 2 nm. The core then reverses and the ferromagnetic state is quickly reached (towards the right side of the figure). In that respect, even at the saddle point, this confirms numerically that in soft ferromagnets a finite radius skyrmion solution exists [105].

As the external magnetic field is increased, the energy barrier decreases drastically (right inset of Fig. 3.13) reaching 0.5 meV at 800 mT. For each magnetic fields, the skyrmion solution at the saddle point has a finite radius. The initial flat section of the energy evolution easily allows variation of the skyrmion radius in the vicinity of B_c while the very small barrier at B_c prohibits direct observation of the skyrmion collapse. Still, with the minimal experimental skyrmion half radius of $\approx$ 3.1 nm the direct vicinity of the collapse is observed to a good approximation and all further compression

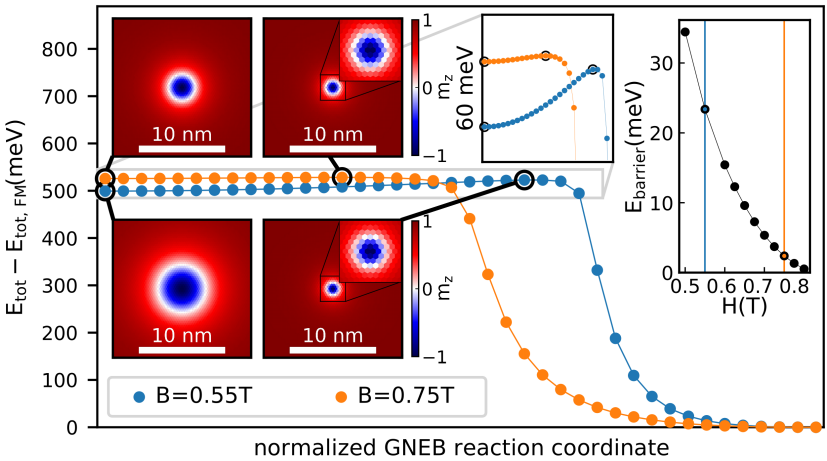

Figure 3.13: GNEB calculation: for B = 0.55 mT (blue) and B = 0.75 mT (orange) with zoom-in between 485 and 545 meV. The right inset shows the magnetic field dependence of the GNEB energy barrier. The four left insets depict the distributions of the z-component of the magnetization, including zooms of the saddle-point core. Taken from [90].

leads to vanishing of the barrier (or tunneling) on timescales too small for observation.

3.2.4 Proximity effect between Ru and hcp and ε Co

One goal of this work is to couple magnetic skyrmions with a superconducting surface. It is therefore of first importance to study the transparency of the deposited Co sub-ML to Cooper-pairs. As Co is not a superconductor and is magnetic, the superconducting order parameter is expected to be locally reduced. As we investigated the samples, we discovered that Co has a long range effect on the order parameter. Furthermore, the way cobalt is stacked on the Ru(0001) surface, i.e. hcp of ε, matters a lot for the modification of the superconducting order parameter. This section is adapted from an article to be published.

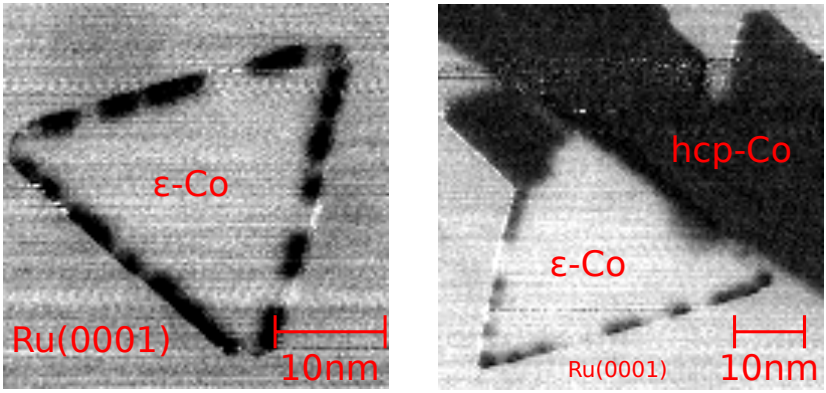

Figure 3.14: Differential conductance map of hcp and ε-Co islands: (a) and (b) were measured at the quasiparticle peak energy. Bright area are locations where either the Ru(0001) surface is free of Co-island, or where the Co-island is transparent to Cooper-pairs, i.e. ε-Co. Darker area are the position of hcp-Co islands, with very low transparency to SC Cooper-pairs. $I = 700$ pA, $U = 60$ µV, $U_{mod} = 20$ µV.

As explained previously, Co can exhibit two different stackings on the first monolayer. We observed that the superconducting gap is different for the two stackings. Not only the stacking of these two phases is different, but they also show very different behaviors when it comes to considering the proximity effect. While hcp-stacked islands behave as expected, i.e. the transparency to SC Cooper-pairs is rather small, the ε-stacked islands have a completely opposite property, in the sense that Cooper-pairs seem to go across the interface without problem, the interface is therefore almost completely transparent. This effect can be seen by mapping the differential conductance at the quasiparticle state energy. Measuring at this energy gives us an indirect probe of the order parameter, as the LDOS will be of the form:

$$\rho_{tot} \propto \alpha\rho_{SC} + (1 - \alpha)\,\rho_N, \tag{3.4}$$

with α a parameter varying between 0 and 1 picking the transparency of the interface ($\alpha = 1$ for a completely transparent interface, and 0 for a non-transparent interface), ρ_{tot} the measured LDOS and $\rho_{SC/N}$ the superconducting/normal fractions of the LDOS. With this simple image, we can see that the LDOS at the quasiparticle state energy will reduce with the transparency of the interface, giving us a probe of the order parameter. A dI/dU

map of a single ε-Co island recorded at this energy is shown in Fig. 3.14 (a), while a map of a ε-Co island relaxing to hcp stacking is shown in Fig. 3.14 (b). One can see that, on ε-Co islands, the LDOS appears the same as on free Ru, while the contrast is darker on hcp-Co islands. This indicates to us that ε-Co islands are mostly transparent, not reducing the gap significantly, while hcp-Co transparency reduces the gap in a visible way. It is also worth noting that ε-Co islands exhibit a lower differential conductance at the edge, similarly to hcp-Co islands. While it may be interpreted as topological bound states [109], when we put this in parallel with the higher apparent height observed on topographic images, this rather gives us further indications that ε-Co islands relax into the hcp stacking at the edge. On the dI/dU maps, it is visible that the line following the edges are not continuous. On these discontinuities, the interface is again transparent to the Cooper-pairs. We interpret this effect as being simply locations where the ε island does not relax into the hcp stacking.

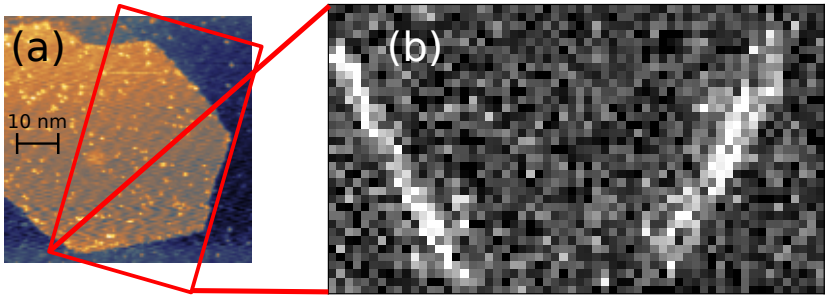

Figure 3.15: Incompletely formed ε island and corresponding hcp-relaxation: (a) Topography of an island that is not completely formed, i.e. edges perpendicular to the preferred directions of growth have not yet met. $I = 500$ pA, $U = -350$ mV (b) Grid-STS recorded on the island. $I = 1$ nA, $U = 1$ mV, $U_{mod} = 15$ µV. The displayed dI/dU value is the value taken at 0 eV. The darker regions are therefore regions where the gap is deeper, and the brighter region the ones where the gap is strongly reduced, i.e. where the transparency is high and low, respectively.

This last effect is even more obvious on incompletely formed islands. When the edges oriented perpendicularly to the preferred growth directions do not meet each other, it results on a hexagonal island. Such an island is shown in Fig. 3.15 (a). On this island, we performed a grid STS measurement, i.e. we defined a grid of points, on which we performed an STS measurement on each point (Fig. 3.15 (b)). We can then plot the value of dI/dU for each point

and the energy we want to investigate. As for the previous measurements, the island exhibit high transparency to SC Cooper-pairs on the core of the island, but seems to relax at the edge of the island into hcp stacking.

That being said, one can notice that, with this hexagonal shape island, the decreasing of transparency happens only every other edges, indicating that the relaxation of the ε phase happens only in the preferred growth directions of ε islands.

We investigated the proximity effect between Ru and the Co islands by recording local tunneling spectra. Fig. 3.16 (a) and (d) show individual dI/dU spectra recorded in three positions as indicated by the color code on (b) and (e). The insets of Fig. 3.16 (b) and (e) show the individual hcp and ε-islands as well as the line section, on which the spectra were taken. Next to both islands and on the Ru substrate, the spectra (blue curves) show a superconducting gap of $\Delta = 60.7 \pm 0.7$ μeV which is slightly lower than our previous measurements on bare Ru(0001) [72]. Additionally, the gap is incomplete, i.e. the differential conductance does not vanish at zero bias. This non-vanishing 0 eV LDOS is due to the estimated coherence length for Ru being $\xi = \frac{\hbar v_f}{\pi \Delta} = 3.4$ μm, i.e. it is much larger than the average Co islands and their separation. Thus, the effect of the islands on superconductivity of the substrate is spatially averaged out and the gap on the free Ru surface is consistently reduced on the whole surface due to the proximity effect. Placing the tip on the island edge, the behaviors of hcp- and ε-islands are similar (green curves). The zero-bias conductance is further increased, i.e. the Cooper-pair density decreased. When, however, measuring inside the islands (red curves), the spectra differ dramatically. While on the ε-island, the spectrum is almost identical to that of the bare Ru, on the hcp island we find a strong reduction of the gap. Both the gap depth and its width are reduced. Moreover, an asymmetry is observed in the peak structure above and below the gap. Such a behavior is caused by Yu-Rusinov-Shiba (YRS) states [110–113], when a magnetic metal or impurity is brought in contact with a superconductor. Fig. 3.16 (b) and (e) show color coded dI/dU spectra as function of lateral displacement when going from the island (left) over the island edge to the bare substrate (right). We note that the reduced gap on the edge of the ε-island coincides with the bright rim observed in the STM topography. The atomically resolved image shown in Fig. 3.4 (a) indicates that the rim consists of hcp Co. This also explains the similar spectra for the two island edges.

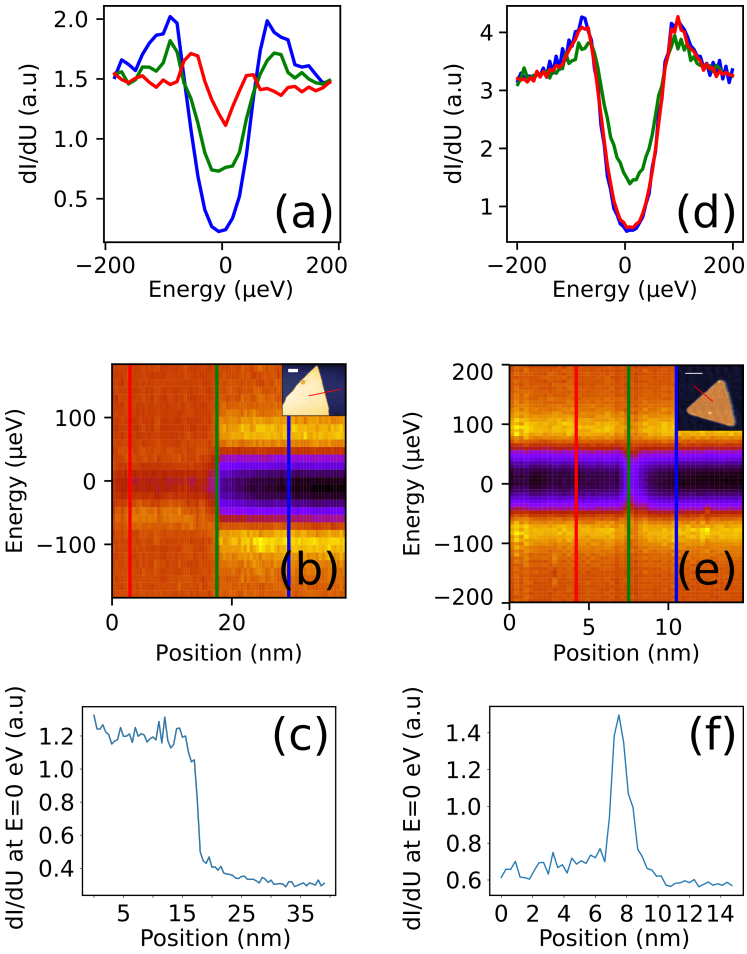

Figure 3.16: Proximity effect at Co island's edge: Left panel: recorded data for hcp-Co. I = 1 nA, U = 600 μV, U_{mod} = 20 μV Right panel: recorded data for ε-Co. I = 1 nA, U = 300 μV, U_{mod} = 20 μV. (a) and (d): Individual dI/dU spectra recorded on free Ru (blue curves), edge of the island (green curves) and on the bulk of the island (red curves). The line profiles are extracted from the dI/dU spectra visible on (b) and (e). (b) and (e) : Color coded dI/dU spectra plotted against lateral position of the tip. The leftmost spectra are recorded on the island, while the rightmost spectra are recorded on free Ru. Insets show the topographic images of the islands on which the spectra were recorded (white bar=10 nm). The red line shows the position of the tip. (c) and (f): dI/dU value at the Fermi energy plotted against the position of the tip.

We performed STS on each region of the sample, i.e. hcp- and ε-Co and free Ru(0001) surface. A comparison of the gap measured on the different regions is shown in Fig. 3.16. In this figure, we can see that the gap is not reduced compared to the gap measured on free Ru surface of the same sample when the tip is placed above an ε-Co island, while it is strongly reduced when it is placed above a hcp-Co island. Calculations of the Fermi surface made for fcc and hcp stacking by Bertrand Dupé and Patrick Bühl are shown in Fig. 3.17 (a). It shows that the two arrangements have a different matching with the one of Ru(0001) surface: the fcc Fermi surface has a hexagonal-like shape, which one is aligned with the one of Ru(0001), while hcp Fermi surface exhibits the same general shape, but rotated by 30°, and therefore not aligned with the one of Ru(0001). Although ε-Co stacking is different from the fcc stacking, we can compare experimental differential conductance spectra shown in Fig. 3.17 (b) to the simulated density of states in the vacuum obtained for hcp and fcc stacking of Co, at distances of 4 Å, 8 Å and 12 Å as shown in Fig. 3.17 (c), (d) and (e), respectively. All spectra show 3 peaks below the Fermi level whose intensities change as a function of the distance. The calculated vacuum DOS are very similar for the hcp and fcc stacking to the experimental spectra. For the hcp stacking 3 peaks are visible at −500 meV, −270 meV and −10 meV whose amplitudes are increasing monotonically with distance. In the fcc case, the 3 peaks are located at lower energies. The peaks are located at −100 meV and −350 meV while the third peak at −600 meV sees its position and amplitude changing. The computed vacuum DOS are in very good agreement with the experimental measurements, which indicates that the ϵ stacking is rather similar to the fcc stacking. It gives us pretty good insight on the reason why the gap is not reduced in a meaningful way for this arrangement. Furthermore, ε-Co has a large primitive lattice with multiple atoms, which would cause the Fermi surface to fold back, therefore increasing the matching between it and the Fermi surface of Ru(0001).

For the hcp island, an increase of the quasiparticles state starts about ≈15 nm before the island edge, abruptly jumps at the edge and is essentially constant on the island. The first effect can be simply explained by the dimensionality n of the problem. In general, the proximity effect leads to variations of the order parameter in a superconductor with the function $|\Psi|^2 \approx r^{-(n-1)} e^{-r/\xi}$, i.e. for a 1d problem the usual exponential decay is found, while for higher dimensions, the scattering geometry has to be considered. For a 3d situation, the $1/r^2$ factor simply represents particle conservation. We here refrained to fit the dependence, as first of all ξ is so large that no meaningful number can be fitted

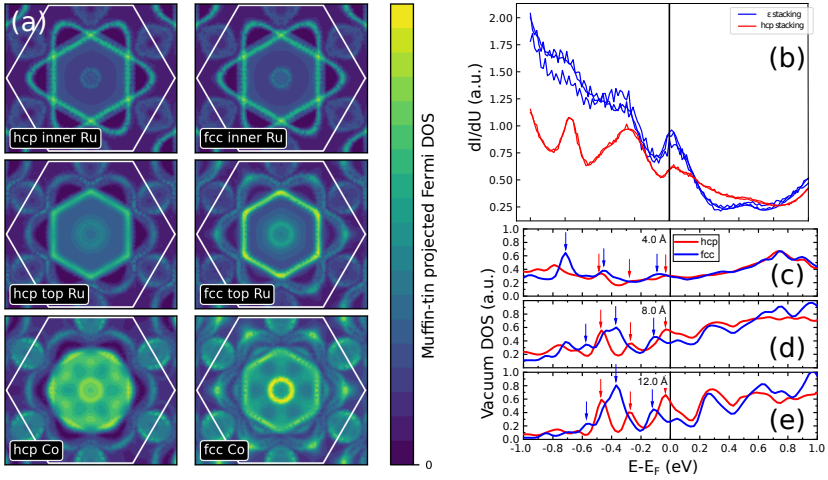

Figure 3.17: Fermi surfaces calculation for different stackings of Co/Ru(0001) and calculated and experimental DOS comparison: (a) Fermi surface muffin-tin projection for the fcc and hcp configuration of the 21 atoms thick symmetric slab DFT calculation. A Gaussian smearing of 100meV is used. (b) differential conductance obtained for both the ϵ and hcp phases. (c), (d) and (e) simulated vacuum density of states at 4Å, 8Å and 12Å from the Co surface, respectively.

on sections of a length of only few nm and secondly, the dimensionality of the problem near an island should display a crossover from 2d to 3d. Essentially, the same behavior is found for the ε-island. The sudden jump, however, indicates partial transmission of electrons at the edge. Again, the two islands show the same behavior at the island edge. This is well justified by a narrow hcp rim around the ε-island.

We found another noticeable effect when we performed STS measurement on the triangular impurities described in section 3.2.2. As we saw previously, these impurities appear on some islands and prevent us to see the spin structures. We could measure the gap on these impurities, and observed that the LDOS was different from the LDOS measured on pure hcp-Co islands. On the long scale, far from the impurities, the LDOS is not modified. But on the impurities positions, the transparency appears slightly larger than on hcp-Co. That is, the dI/dU value at the Fermi level is lower, as more Cooper-pairs cross the interface without problem. Furthermore, the asymmetry of the gap is reduced or even canceled in certain cases, indicating that these impurities

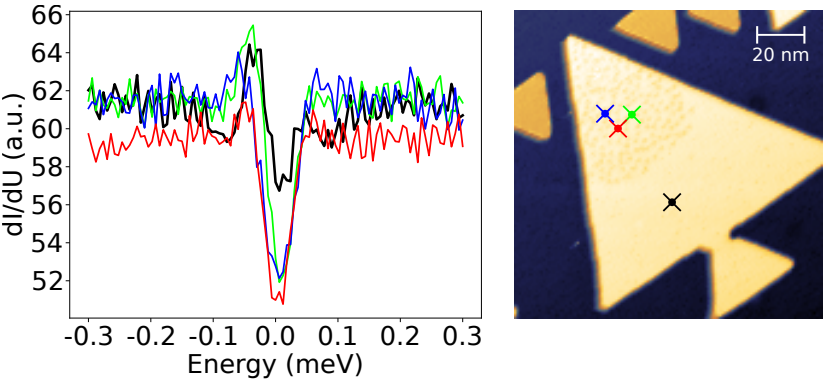

Figure 3.18: Cooper-pair transparency comparison between pure Co layer and Ru/Co impurities: (a): Spectra recorded on Co island containing Ru inclusion impurities. The position where each spectrum was recorded are indicated on the topographic image in (b). $I = 1$ nA, $U = 300$ µV, $U_{mod} = 20$ µV. Spectra recorded on the area containing the impurities (red, green and blue curves) have a lower differential conductance at 0 eV, meaning a higher Cooper-pair transparency. $I = 1$ nA, $U = -350$ mV.

are non-magnetic and therefore do not lead the emergence of YRS states in the gap. This gives us further indication that these impurities are in fact Ru atoms included in the hcp-islands, as the transparency is increased on the impurity location. The STS measurements as well as the position they were measured on is shown in Fig. 3.18 (a) and (b).

3.2.5 Coexistence of skyrmion and superconductivity

For the MZS to appear, it is necessary to have both a magnetic skyrmion living on the surface, and the superconducting state of the Ru(0001) sample. Although it may seem trivial, we recall that a superconductor is a perfect diamagnet and as such, it will repel magnetic field. Therefore, one might expect the spin spiral structure to change, as the stray field coming from the magnetic adatoms will experience a repulsion from the surface [43]. This phenomenon is illustrated in Fig. 3.19

The important question to answer is if this phenomenon affects the magnetic structure of Co/Ru(0001) in a meaningful way: does it modify the period of

the spin spiral or forces the spins to align further? Finally, is it possible to have stable skyrmions existing when the Ru substrate experiences a transition to the SC state?

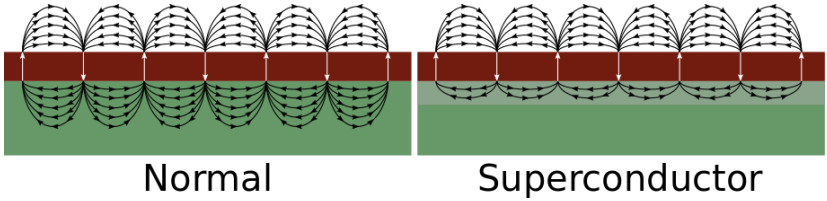

Figure 3.19: Schematic view of the SC's action on the spin spiral: Normal state (left) compared with superconducting state (right). The stray field penetrates the substrate when it is in the normal state, while it is repulsed and compressed out when the substrate is superconducting.

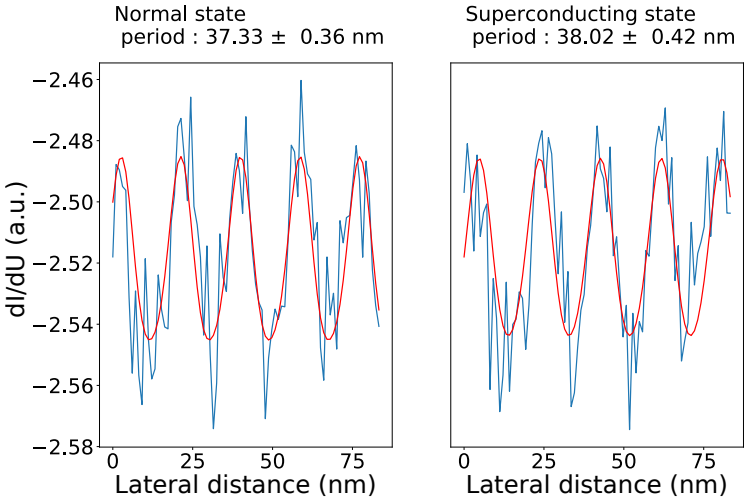

Figure 3.20: Averaged dI/dU signals recorded on an isolated island: Left: normal state of the substrate. Right: superconducting state of the substrate. The blue curves show the averaged signal, while the red curves show the obtained fit in both cases.

To answer the first two questions, we simply measured the magnetic ground state of an isolated Co island in the normal and in the superconducting state. To extract the spin spiral features, we average it over a certain width on the

island. We then fit the averaged signal with the first and second harmonic of the periodic signal:

$$\frac{dI}{dU}(x) = A\cos\left(\frac{4\pi x}{l} + \phi_1\right) + B\cos\left(\frac{2 * 4\pi x}{l} + \phi_2\right), \tag{3.5}$$

with x the lateral position along the spiral, l the period of the spiral and $\phi_{1/2}$ an arbitrary phase between the two harmonics. Fitting the TAMR signal in the normal state gives us a lateral period of $l_N = 38.02 \pm 0.42$ nm, while in the SC state we obtain $l_{SC} = 37.33 \pm 0.36$ nm. The averaged signals for both states of the substrate are shown in Fig. 3.20. As we can see, no significant modification occurs on the spin spiral state when the sample is in the superconducting state, which indicates that skyrmions should also not undergo meaningful modification in the same situation.

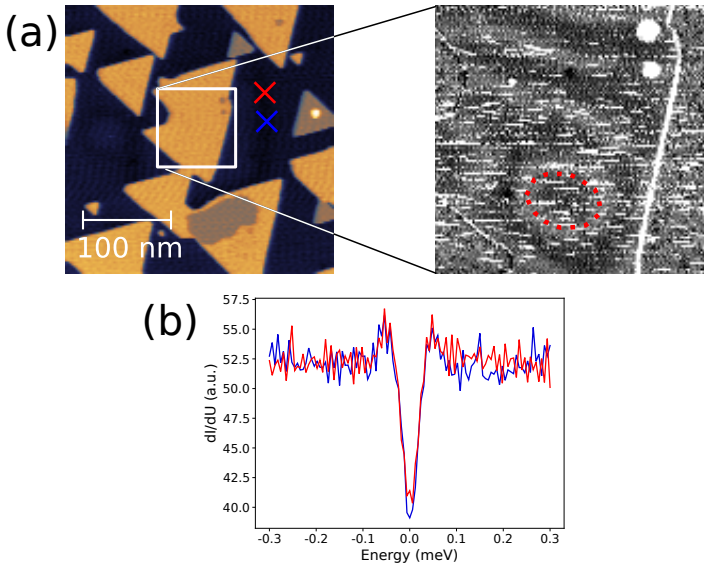

Figure 3.21: Superconductivity in presence of a skyrmion: (a): Topographic image with corresponding dI/dU map indicated by a white box, In the dI/dU maps, the red dashed curve imposed on the formed skyrmion guide the eyes. (b) dI/dU spectra recorded on the positions indicated in (a) after the skyrmion was formed. No MZS is visible. (a) topography $I = 1$ nA, $U = 100$ mV. (a) dI/dU map $I = 1$ nA, $U = -350$ mV, $U_{mod} = 60$ mV. (b) $I = 1$ nA, $U = 300$ µV, $U_{mod} = 20$ µV.

Since we could successfully restore the superconductivity of the sample after applying a magnetic field above the value of the critical field of Ru, we can form skyrmions and ramp down the field below the critical field value to obtain a superconducting sample hosting skyrmions as well. At base temperature, the field is ramped up to 250 mT to create skyrmions. Once this is done, the field is ramped down until the SC state is retrieved and STS is performed to check the existence of MZS. As mentioned earlier, MZS are not predicted to appear for a skyrmion-SC hybrid system if the skyrmion has an odd winding number [21, 22], which is the case here. We could confirm this statement, as after forming skyrmions with winding number $n = 1$ and successfully restoring superconductivity, no zero energy state could be observed reliably. In Fig. 3.21 (a) and (b), we show a skyrmion on the superconducting surface, and the corresponding STS measurements that were performed.

Yet, on two occurrences, we could detect a modification of the LDOS that took the form of a zero energy state. These states were not stable in time and disappeared after some minutes. Therefore, we could not link the existence of these states to any magnetic texture on the surface. The STS measurement exhibiting this behavior are shown in Fig. 3.22 (a), as well as the position on which they were measured in Fig. 3.22 (c) and (d). Fig. 3.22 (b) show the dI/dU spectra recorded without skyrmion (black curve) and after forming the skyrmion (orange curve). Fig. 3.22 (d) shows the corresponding dI/dU map exhibiting a skyrmion on the Co island Although skyrmions formed in our experiment do not provide a platform to host MZS, other spin texture could be the reason we observed this zero energy state. These objects are shortly described in the next section.

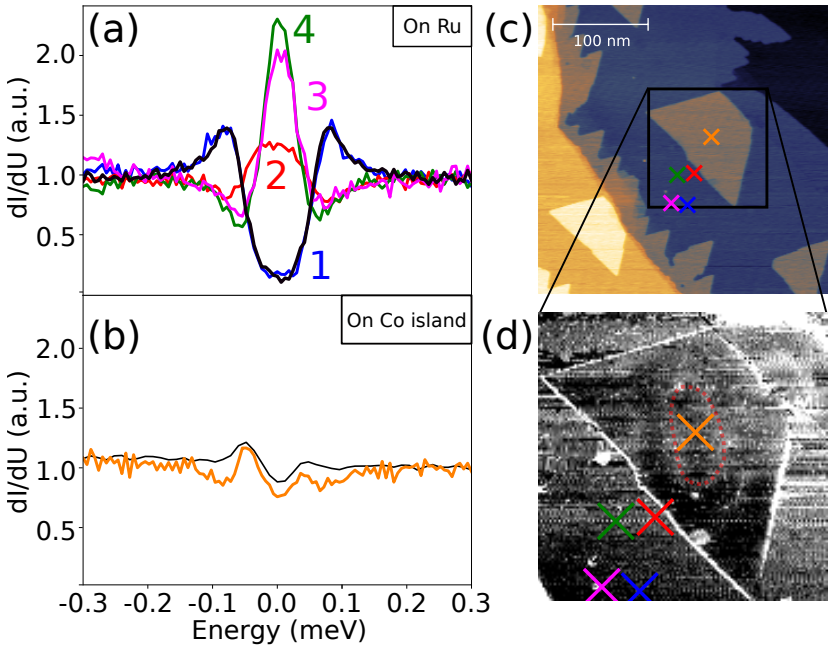

Figure 3.22: Emergent 0 energy state after magnetic field application: (a) dI/dU spectra recorded on free Ru(0001) near an island hosting a skyrmion. The black curve was recorded before a magnetic field was applied for reference. The other curves were recorded after magnetic field was applied on the positions indicated on (c) and (d). Zero energy states are visible for curves 2, 3 and 4. (b) Spectrum recorded in the center of the skyrmion visible in (d), on the Co island. No meaningful modification of the LDOS before magnetic field was applied (black curve for reference) is visible. (c) Topographic image of the island hosting a skyrmion. A zoomed dI/dU map indicated by a black box is shown in (d) and a dashed red curve imposed on the skyrmion guides the eyes. (a) and (b) $I = 700$ pA, $U = 300$ µV, $U_{mod} = 20$ µV. (c) $I = 1$ nA, $U = 10$ mV. (d) $I = 1$ nA, $U = -350$ m V, $U_{mod} = 50$ mV.

3.3 Other candidates for MBS realization

Even if skyrmions with an odd winding number did not lead to the emergence of MBS, we just saw that MZS alike states were measured. Other spin textures are predicted to lead to MBS when placed in contact with a superconductor. In this work, we also tried to study these textures, and see if MBS would be

visible, to check if they could be responsible for the zero energy state we observed.

3.3.1 Trijunction spin texture

The trijunction spin texture is simply a particular configuration of the default structure of the spin spiral. It consists of three distinct zones with out-of-plane spin orientation, separated by three lines also with out-of-plane magnetization, but in the other direction, meeting at one single point. Such a texture is shown in Fig. 3.23 (a). It is predicted that this structure placed in contact with an SC could lead to MBS emergence [114]. Although it is in principle not possible to engineer such a structure with magnetic field only (further action of the tip may be required, endangering the surface), we found it naturally formed on some islands, and could therefore verify if MBS emerged from this structure. Once we found a structure resembling the trijunction texture, shown in Fig. 3.23 (b), we ramped the magnetic field in both directions and measured the gap at the same time, until $B = \pm 5$ mT (killing the superconductivity), as it is predicted that trijunction structures in contact with an SC would lead to MBS emergence on the condition that a magnetic field is applied to the system [114]. Yet, no zero energy state could be observed like this.

3.3.2 skyrmion with winding number n=0 or n=2

It is also possible in theory to form a skyrmion with a topological winding number $n = 0$ (that is, the magnetic moment at the core has the same orientation as the moments at the edge of the skyrmion, and the moments in the middle of these two locations have an opposite direction) or $n = 2$. In fact, It has been recently proposed that skyrmions with an arbitrary winding number can be engineered [115]. In Fig. 3.24 (a), we show the theoretical shapes that skyrmions with winding number $n = 0$ would exhibit and compare it with the shape of the $n = 1$ skyrmion. We also show the attempt to experimentally realize a skrymion with $n = 0$ [115] in Fig. 3.24 (b) and (c). In principle, as this object has an even winding number, MBS should emerge naturally without further action when placed in contact with a superconductor. In practice, this object can be hard to form, since it will not form spontaneously. Therefore, we have to somehow engineer its formation. We attempted to create these

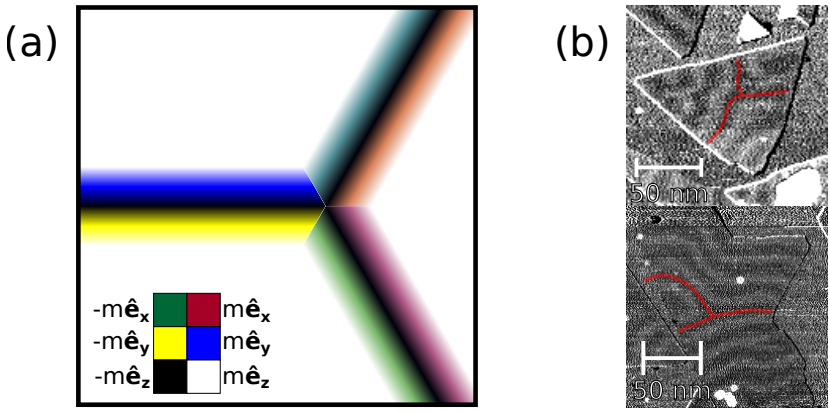

Figure 3.23: Trijunction model and experimental observation: (a) Theoretical trijunction spin texture. Reproduced from [114]. (b) dI/dU maps of islands exhibiting trijunction-like structure. Red lines are superimposed to guide the eyes. $I = 1$ nA, $U = -350$ mV, $U_{mod} = 50$ mV.

skyrmions by first applying a magnetic field of 250 mT in order to form a skyrmion with winding number $n = 1$, and ramped down the field to 0 mT. At this stage, the core of the skyrmion and the edge of the skyrmion are antiparallel. Now, since we want the edge of the skyrmion to be in the same orientation as its core, we have to apply the magnetic field in the opposite direction as before. We therefore slowly ramped down the field from 0 mT to −250 mT, and imaged the spin texture every −50 mT. Most of the time, the core of the skyrmion was expanding and relaxed to the ferromagnetic state at around −200 mT, as this time it was aligned with the applied field. Although, on one attempt, the skyrmion was constrained enough so that the force applied from the edge to the core of the skyrmion were larger than the opposite force. On this attempt, we came close to the desired object, shown in Fig. 3.24 (b) and (c). Unfortunately, the local defects pinned the magnetic moments, and the object could not be detached from these defects before it relaxed into the ferromagnetic state. This showed that, although hard, the experimental realization of a skyrmion with winding number $n = 0$ may not be an impossible task, but more engineering is required. Specifically, one needs to obtain a defect free island, otherwise the magnetic moments pinned to these defects will not unpin, and the magnetic structure will not close itself.

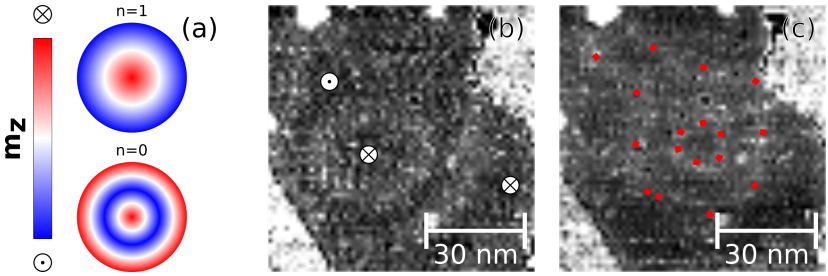

Figure 3.24: $n = 0$ skyrmion model and experimental realization attempt: (a) Comparison of two skyrmions with $n = 1$ and $n = 0$. Only the projection of the magnetic moment on the out of plane axis is displayed. Figure reproduced from [115]. (b) and (c) Experimental attempt to create skyrmion with $n = 0$. The direction of the magnetic moments is indicated in (b). In (c), the dashed red curve is imposed with the in-plane magnetic moments. Image recorded with external magnetic field $B = -100$ mT for (b) and $B = -240$ mT for (c). Darker and brighter stripes correspond to out-of- and in-plane magnetization, respectively. $I = 1$ nA, $U = -350$ mV, $U_{mod} = 50$ mV.

4 Study of Ru multilayers deposited on Nb(110) surface

As shown in the previous chapter, the existence of skyrmions in contact with an S-wave superconductor does not lead to MZS. In fact, the skyrmions we form on the Co/Ru(0001) system have an odd winding number of 1, which in turn prevents the emergence of MZS [22]. Yet, correctly coupled with other materials, it is in theory possible to raise the effective winding number by one, bringing it to an even number and allowing the emergence of MZS. To do so, the skyrmion may be coupled to a superconducting vortex [22]. To achieve that, we propose to use a new hybrid system of Co/Ru_{10ML}/Nb(110). This chapter shortly presents the basic principles that motivate the experiment, the investigated system and finally the results of the preliminary work made on this system.

4.1 Overview of the basic principle

The idea behind this preliminary work is to couple skyrmions with an odd winding number with a superconducting vortex created by a type II superconductor. The phase winding of the superconducting order parameter adds up to the skyrmion's winding number, effectively bringing the winding number of the skyrmion-vortex system to an even value [22]. Since the skyrmion keeps its topologically non-trivial structure, the effective Rashba and Zeeman interactions are conserved and the emergence of MZS is still possible [21]. The coupling of skyrmions with antivortices has recently been experimentally realized [IrFeCoPt]/Nb heterostructure [116], where the skyrmions stray field nucleate the antivortices in 25 nm Nb film.

In our case, we saw in the previous chapter that it was possible to create skyrmions for the system Co/Ru(0001) with great reproducibility, and experi-

ments suggest that moving skyrmions on the surface is a possible task, given their soft nature. Hence, Co/Ru(0001) still seems to be the system we want to work with. Yet, because of the skyrmions having a winding number $n = 1$, and the Ru being a rather weak type I superconductor with low T_C and large coherence length, the system needs to be tuned, and some key ingredients require to be brought to the system to allow the emergence of MZS, namely increasing the winding number by 1 (or any odd number), and increasing the robustness of the superconducting substrate (the latter is optional, but for convenience and reliability of the measurement, quite necessary)

As stated before, a way to increase the effective winding number would be to couple the skyrmions with a superconducting vortex. Therefore, we choose to use a single crystal of niobium 110 (Nb(110)) to be the substrate of the system. Nb(110) is a type II superconductor, and will naturally host a superconducting vortices lattice when a magnetic field is applied. The T_c of Nb is 9.26 K [117, 118], which makes it a more robust superconductor than Ru with a much shorter coherence length. By proximity, and given the long coherence length of Ru, we expect the superconductivity properties of Nb to leak into deposited Ru over several MLs, as long as the thickness of the deposited material is much lower than the coherence length of Ru. Furthermore, Ru having a low critical field, superconducting vortices trapping a field higher than B_c(Ru) would also be visible through several MLs of Ru. Effectively, Ru deposited on top of Nb(110) would exhibit the same SC properties as the latter over a thickness of the same order of magnitude than the coherence length of Ru, that is $\xi \sim 3.4$ µm. If the deposited Ru stacks in the (0001) direction of the crystalline structure, Co sub-ML can then be deposited on the obtained surface, in order to later form skyrmions that would couple to superconducting vortices. For this, one need to deposit > 6 ML of Ru on Nb(110), as the Co needs to be decoupled from Nb(110). The imagined system is pictured in Fig. 4.1.

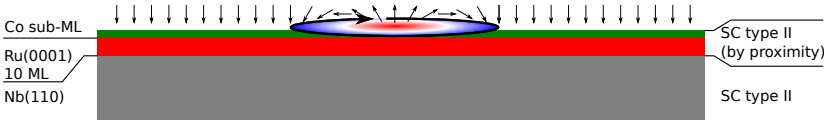

Figure 4.1: Model of the $Co_x/Ru_y/Nb(110)$ system: The model system is depicted, with monocrystalline Nb(110) as a substrate, Ru monolayers can be deposited (y > 6 ML). If Ru stacks in the (0001) direction, Co sub-ML (x<1) can be deposited to later form skyrmions by applying magnetic field.

As illustrated in Fig. 4.2 (a), when skyrmions and vortices have been created successfully, by default the interaction between them would be repulsive, as the magnetic flux lines in the vortex will have an opposite direction than the magnetic moment of the core of the skyrmion. With the lines of the vortex parallel to the magnetic moment of the skyrmion's core, the interaction becomes attractive as shown in Fig. 4.2 (b). If needed, a small magnetic field can be applied in the other direction to invert the polarization of the vortices core and make the interaction between them and the skyrmions attractive.

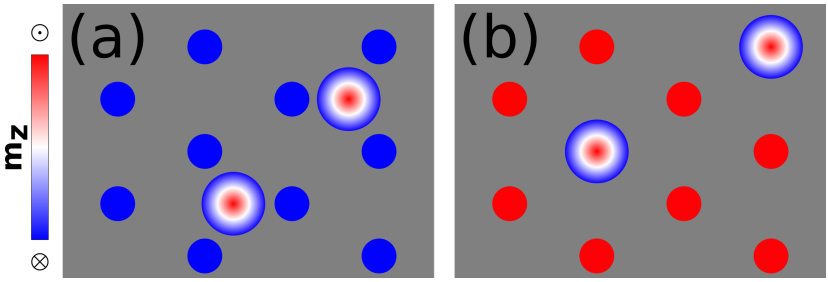

Figure 4.2: Illustration of interaction between skyrmions and SC vortices: (a) In the case that the skyrmions core's magnetic moment is in the opposite direction as the magnetic field lines trapped by the vortices, the interaction between the two is repulsive, and the former will lie in between the latter. (b) If the core's magnetic moments are in the same direction as the trapped magnetic field, the interaction becomes attractive and skyrmions would lie in the on-site positions.

4.2 Nb(110) surface

4.2.1 Surface preparation

Previous works described the process to obtain a clean surface of Nb(110), near to impurity free [83, 119]. For this, it is in principle necessary to alternate between Ar^+-sputtering and annealing cycles at $T \gtrsim 2200$℃. Yet, the melting point of pure Nb is $T = 2477$℃, i.e. a difference of only 250℃. Furthermore, to obtain a cleaner sample, it is necessary to bring the temperature of the sample as close to the melting point as possible.

To avoid the risk of melting the sample, we limited the annealing temperature at $T = 1700$℃. Any higher temperature could not be achieved without putting

the sample or the manipulator head at risk. The consequence of this is that, although the surface is mostly found to be free of impurities, the annealing temperature is not high enough to remove the oxide layer reconstruction bound to the surface [119]. We decided to make the Ruthenium deposition on that surface, as the effects we want to transmit to the ruthenium multilayers are bulk effects and should not depend on the surface.

4.2.2 Clean surface and NbO surface reconstruction

As mentioned before, when the Nb crystal is not annealed high enough, an NbO layer remains on the surface and reconstruct in a quasi-periodic structure. Topographic images of the surface and of the surface reconstruction in Fig. 4.3. Actually, this oxide layer forms in a very similar way as the carbon impurities on Ru(0001) surface. That is, oxygen atoms are stored in the bulk Nb(110) crystal and are removed from the surface via sputtering, making the surface almost oxygen free (below AES detection level). Then, when the crystal is annealed to allow the surface to flatten again, the oxygen atoms stored in the bulk segregate toward the surface and form a layer of NbO upon cooling down.

An image of the surface reconstruction and the line profile of the reconstruction are shown in Fig. 4.4. The reconstruction of this system has been extensively studied and is well known [119–121]; it is constituted of NbO nanocrystals that form an angle of about $5°$ with the $\langle 111 \rangle$ direction of the Nb(110) crystal. The nanocrystals have a length between 2 nm and 3.2 nm and are arranged periodically with a periodicity of 1.15 ± 0.05 nm. In the rest of the text, we will refer to this surface as free surface of Nb(110).

On a clean surface, we could observe the superconducting properties of our sample, for reference and further comparisons with future samples. We measured the SC gap on the free Nb(110) surface, and fitted it with a regular BCS gap function. The result of the STS measurement and the fit are shown in Fig. 4.5.

4.2.3 Deposition of Ru multilayers on Nb(110)

As explained above, the final goal is to be able to prepare a sample consisting of $Co_{x<1ML}$/Ru(0001)$_{y<10ML}$/Nb(110) to couple skyrmions and superconducting

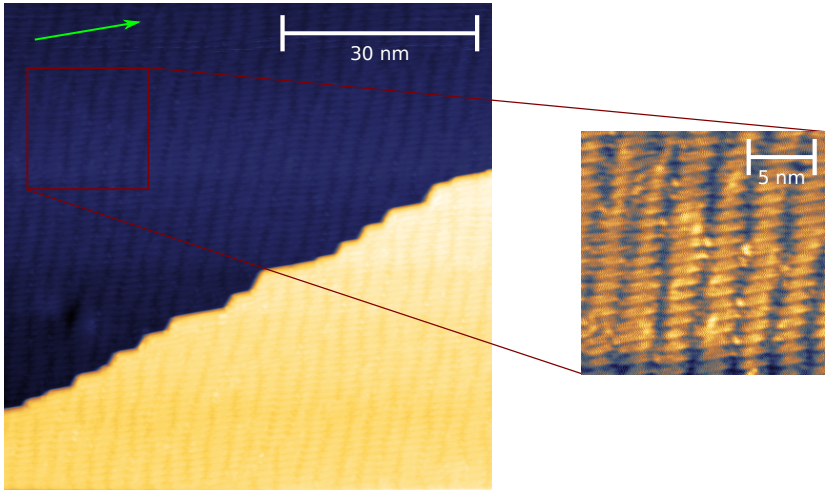

Figure 4.3: Cleaned Nb(110) surface: Topography of the cleaned Nb surface and zoom of the NbO reconstruction (indicated by the red box). The green arrow shows the ⟨111⟩ direction of the Nb(110) crystal. $I = 1$ nA, $U = 100$ mV.

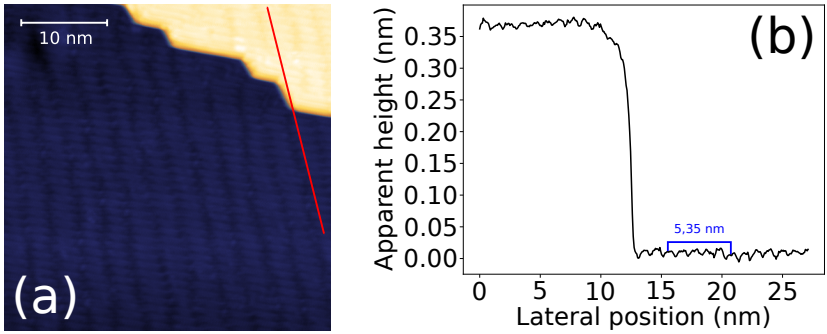

Figure 4.4: NbO surface reconstruction: (a) Topography of the surface showing the reconstruction. (b) Line profile indicated by the red line on (a) taken perpendicularly to the ⟨111⟩ direction. $I = 1$ nA, $U = 1$ V.

vortices. The following sections will present the preliminary work, consisting in the study of Ru/Nb(110).

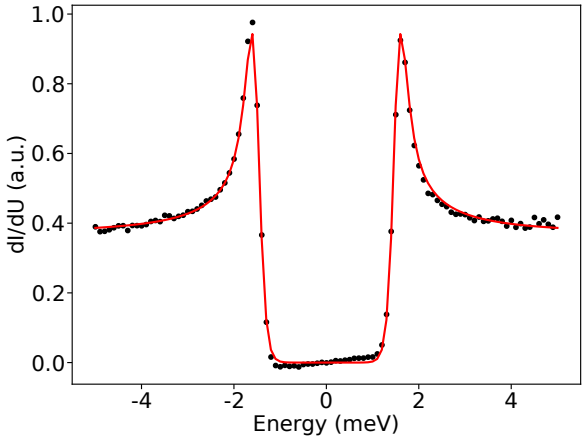

Figure 4.5: Superconducting gap of Nb(110): The superconducting gap was measured on a free Nb(110) surface. The black dots show the measured gap, while the red curve shows the BCS fit performed on the data. Gap obtained by fitting: $\Delta = 1.52 \pm 0.01$ meV. Data were recorded at $T = 686$ mK, $I = 1$ nA, $U = 5$ mV, $U_{mod} = 50$ µV.

Once the Nb surface appears clean enough, we deposited sub-ML to multilayers of Ru on it using MBE. Multilayers were deposited to calibrate the position of the evaporator, and sub-ML to calibrate the deposition rate. It should first be noted that, when depositing Ru on Nb(110), as well as when proceeding to post annealing, one should take care not to apply too high temperatures because Nb and Ru can form unwanted binary alloys [122]. The binary alloys phase diagram for Nb/Ru systems is shown in Fig. 4.6. We estimated the upmost temperature to apply to be 980℃, in order to keep two separated Ru/Nb phases. As we can see in the same diagram, too low-temperature deposition may result in the formation of NbRu' alloy when the weight percentage of Ru exceed 41.6% (at 0℃). For that reason, The temperature of deposition should not be lower than 730℃ to avoid the formation of this alloy.

Multilayers were deposited to calibrate the deposition position. We checked that Ru was present on the surface with AES, which spectra for free Nb and Ru/Nb are shown in Fig. 4.7. Since Ru has a higher melting point compared to Co, a much higher heating of the evaporation rod is required to deposit a significant amount of material on the sample surface. We first tried to deposit

the material at room temperature with the following parameters: $U = 1290$ V, $I_{fil} = 2.3$ A, $f = 150 \rightarrow 205$ nA, $\varepsilon = 35$ mA, $t = 10$ min. The sample was later post annealed at 600 ℃ for 10 min after checking the surface. From the Ru/Nb AES spectrum in Fig. 4.7, it is clear that multilayers of Ru were deposited, considering how the Nb and Ru peaks respectively decreased and increased. Although it may be very hard to estimate the amount of deposited material with precision, we then proceeded with the calibration of the evaporation rate, indicating that ~ 3 ML of Ru were deposited.

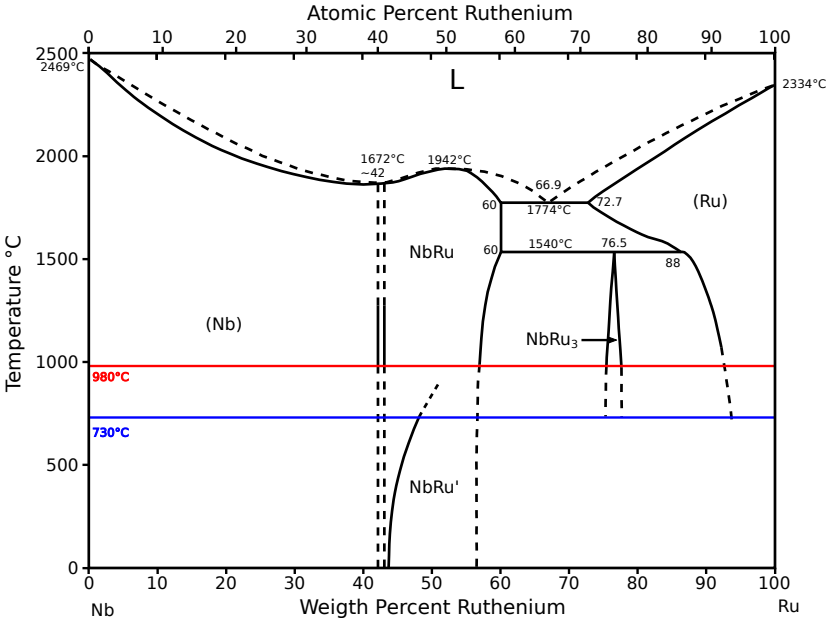

Figure 4.6: Binary phase diagram for Nb-Ru systems: On this diagram it is possible to see that Nb-Ru system can form alloys at relatively low temperature (i.e. far away from the melting point of the two metals). The red line shows the temperature at which the transition between Nb and NbRu happen, while the blue line shows the temperature below which NbRu' alloy forms. These temperatures are the limits of the range the Ru should be deposited in order to avoid forming unwanted alloys and keep the two phases separated. Diagram reproduced from [122].

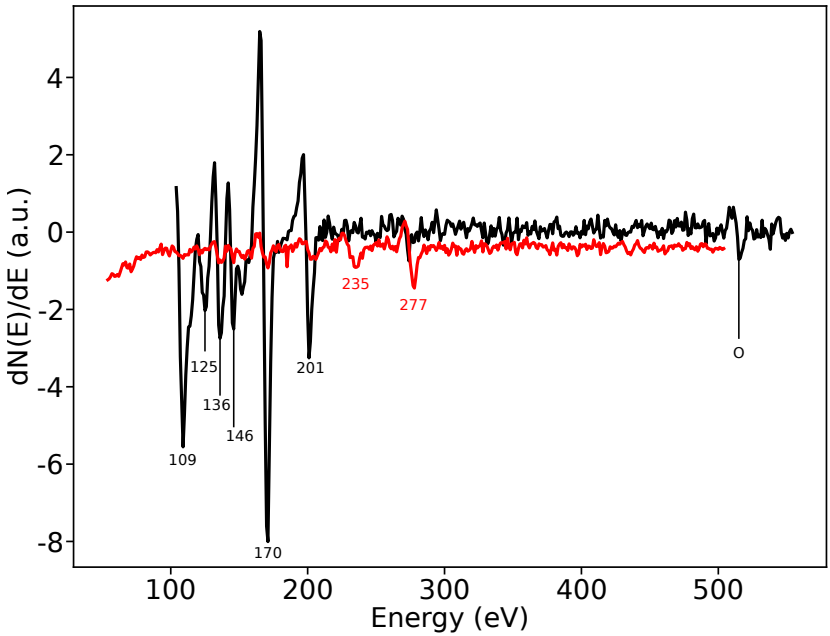

Figure 4.7: Nb(110) and Ru/Nb(110) AES spectra: Comparison of AES spectra recorded on a free surface of Nb(110) (black curve) and multilayers of Ru on Nb(110) (red curve). The characteristic peaks used to identify material on the surface are indicated with the corresponding energies.

The surface shown in Fig. 4.8 (a) was recorded before the post annealing step. It is covered by Ru and appears granular. No order can be seen, but a pseudo-order is visible, as the Ru tend to form a super structure following the one of the NbO reconstruction. After the post annealing at 600℃, the surface shown in Fig. 4.8 (b) is better ordered, and rectangular structures are formed. Yet, it seems that monolayers stacking on top of each other are not fully completed, giving a rough surface and very few flat areas as desired for Co deposition. Furthermore, the rectangular structure seems to indicate that Ru does not stack in the (0001) direction, i.e. in its hcp configuration. This is understandable, as the underlying structure of NbO does not have a 6-fold symmetry. But having Ru in its hcp configuration is of first importance, because we want to keep previous interactions (DMI and exchange) between

a Co sub-ML and the Ru substrate. It is necessary if one wants to form skyrmions when Co is later deposited.

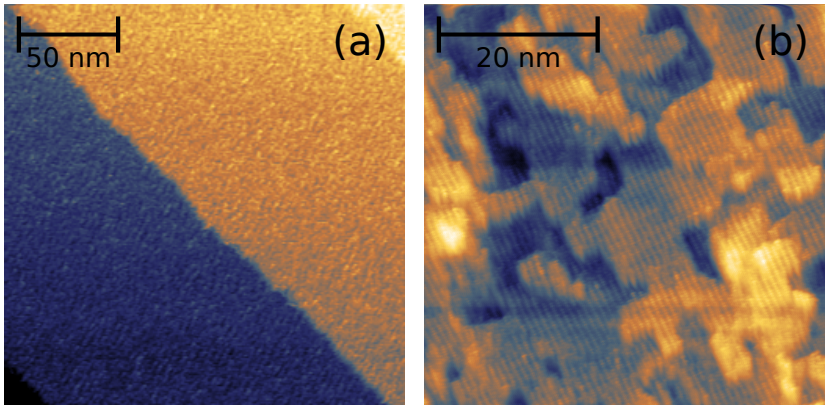

Figure 4.8: multilayers of Ru deposited on Nb(110): (a) $Ru_{3-ML}/Nb(110)$ deposited at room temperature. Ru presents a granular structure with pseudo-periodic arrangement, likely aligning against the NbO reconstruction. (b) Same sample with post annealing at 600 °C. The structure is more regular, and presents a pseudo periodic super structure in one direction. $I = 1$ nA, $U = 1$ V.

Once the position was correctly calibrated, we proceeded with sub-ML deposition for rate calibration. To do so, we heated the Nb crystal at $T \approx 630$ ℃ using HV emission. Once the temperature was stable, the crystal was brought to the deposition position, and Ru was deposited on the surface using the following parameters: $U = 1270$ V, $I_{fil} = 2.3$ A, $f = 160$ nA, $\varepsilon = 36$ mA, $t = 2$ min. The resulting sample surface is shown in Fig. 4.9. The sample is made of 0.57 ML of Ru, and the rest of free Nb(110). The deposited Ru arranges itself in islands that do not seem to follow any particular order at first glance. The size of the islands vary from a few nm^2 to several 100 nm^2. One can recognize the free Nb(110) surface areas, as when we investigate the sample on smaller area, the surface reconstruction appears clearly in the topographic images. This is shown in Fig. 4.10.

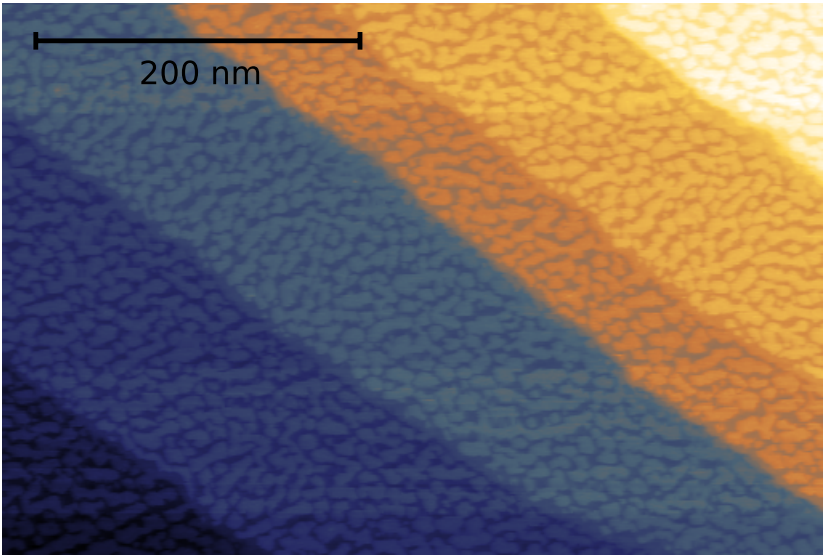

Figure 4.9: 0.57 ML Ru/Nb(110): $I = 1$ nA, $U = 1$ V.

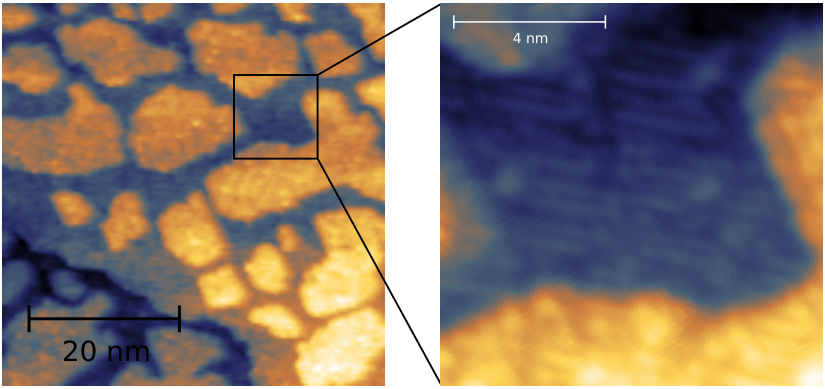

Figure 4.10: 0.57 ML Ru/Nb(110) topography detail: A detail of the topographic image shows that the islands do not seem to exhibit any particular order. The right image is a zoom, indicated by the black box on the left image. The surface reconstruction of Nb(110) is clearly visible. $I = 1$ nA, $U = 1$ V.

Although it is not clear at first sight, the formed islands do respect some kind of ordering. Indeed, when we make a detailed topographic image of the islands' surface, we can distinguish some pattern. This is shown in Fig. 4.11. The islands adopt the structure of the underlying Nb(110) surface reconstruction, and we can therefore see a pseudo ordered structure on the islands. One can notice that a few locations on the islands build up with an angle of 120° with respect to the ⟨111⟩ direction.

To cross-check these results, we made a longer deposition with similar parameters but longer time and hotter sample: $U = 1265$ V, $I_{fil} = 2.29$ A, $f = 160$ nA, $\varepsilon = 36$ mA, $t = 6$ min, $T = 800$℃, this to deposit a complete monolayer plus a certain percentage of a second. The obtained sample is shown in Fig. 4.12 (a) and (b). According to the previous deposition, the sample should have been covered with 1.71 ML of Ru, which is very close to the value we actually observed, 1.53 ML. This in turn gave us good reference values for the quantity of Ru deposited on the surface. As shown in Fig. 4.13, the upper layer (a) also displays a substructure that follows a certain direction, while the lower one (b) is mainly granular, indicating that it is not free Nb surface, but the first layer of Ru.

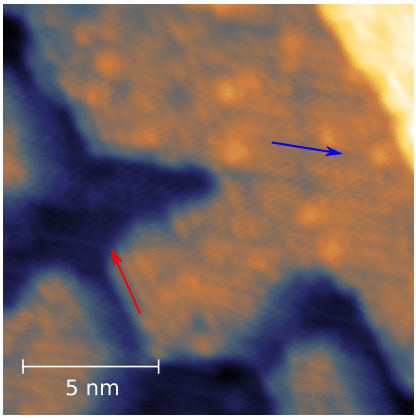

Figure 4.11: 0.57 ML Ru/Nb(110) island pseudo ordered structure: Ru island detail displaying a structure similar to the one of Nb(110) surface reconstruction. Two directions of the line structure are visible: one align with the Nb(110) reconstruction, i.e. along the ⟨111⟩ direction of the crystal (blue arrow along this direction), and the other one forming an angle of 120° with the first (red arrow). $I = 2$ nA, $U = 1$ V.

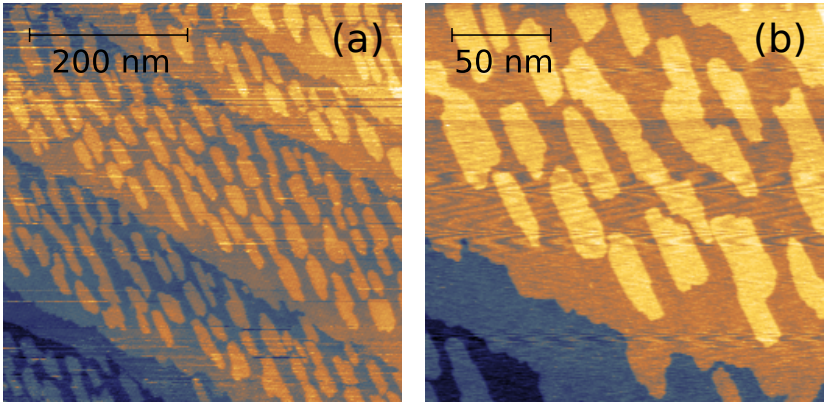

Figure 4.12: 1.53 ML Ru/Nb(110): $I = 500$ pA, $U = 1$ V.

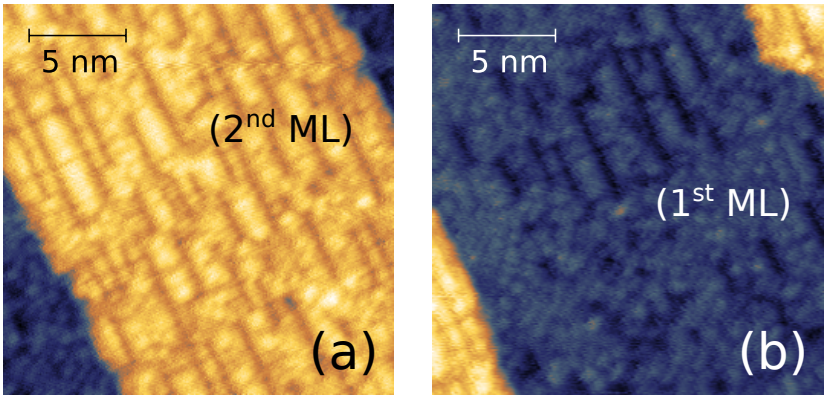

Figure 4.13: 1.53 ML Ru/Nb(110) topography detail: (a) and (b) : 1.53 ML Ru/Nb(110) surface exhibiting clear substructure. $I = 2$ nA, $U = 100$ mV.

4.3 Proximity effect between Nb(110) and Ru

After we successfully deposited Ru on Nb(110), we performed STS gap measurement and dI/dU maps to verify that the system was indeed transparent to superconducting Cooper-pairs coming from the Nb(110) substrate. We

could measure the superconducting gap of the system, and confirm that the superconductivity of Nb was not, or almost not affected by the Ru.

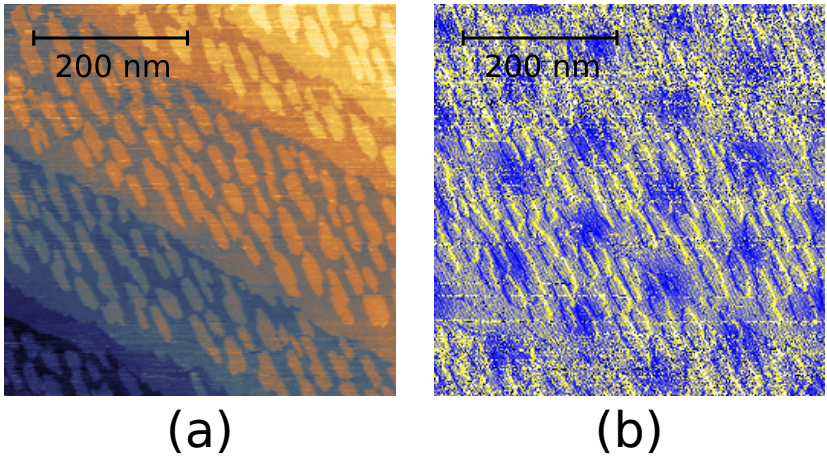

Figure 4.14: Formation of superconducting vortices on $Ru_{1.53\text{-ML}}/Nb(110)$: (a) Topographic image of the $Ru_{1.53\text{-ML}}/Nb(110)$. (b) dI/dU map at the quasiparticle state energy. SC vortices are visible (darker blue disks) whereas the sample is superconducting everywhere else (brighter yellow area). $I = 1$ nA, $U = 1.2$ mV, $U_{mod} = 100$ µV.

We also confirmed that SC vortices were present when applying a magnetic field, without disturbance from the 1.53-ML Ru. While at low temperature, we applied a magnetic field of $B = 250$ mT, and ramped it down to $0 =$ mT. Then, we mapped the differential conductance on the surface near the quasiparticle state energy. The topography of the surface and the dI/dU map are shown in Fig. 4.14 (a) and (b). It is clearly visible that SC vortices have been formed and are traversing the Ru islands without any visible deformation coming from them. That is to be expected, as thin coverage of Ru on Nb(110) should not modify the SC significantly. We therefore prepared a sample with a thicker Ru coverage, using the similar evaporation parameters than the calibration sample, except for a hotter sample and a higher deposition time, to have between 6 and 8 MLs of Ru deposited on the substrate. We then proceeded as before, and applied a magnetic field $B = 250$ mT, after what we preformed an STS grid over the surface, probing the LDOS at 0 eV for each point. The topography of the surface on the grid's frame as well as the grid can be seen in Fig. 4.15 (a) and (b), respectively. As one can see, SC vortices are still

visible and not at all disturbed by the thicker layer of Ru. Additionally, We measured the superconducting gap of the system and compared it with the one of free Nb(110). Again, we fitted the data with the BCS function. The newly measured gap of $Ru_{6-8\text{-ML}}$/Nb(110) as well as its comparison with the gap of free Nb(110) are shown in Fig. 4.16 (a) and (b). We can see that the gap appears clearly, and that the DOS at 0 eV still vanishes. Yet, when we fit the data and compare the gap with its previous value, it appears that the Ru multilayers reduced it by about 13%, i.e. the gap is ~ 0.2 meV smaller ($\Delta_{\text{Nb(110)}} = 1.52 \pm 0.01$ meV and $\Delta_{\text{Ru}_{6-8-\text{ML}}\text{Nb(110)}} = 1.31 \pm 0.01$ meV).

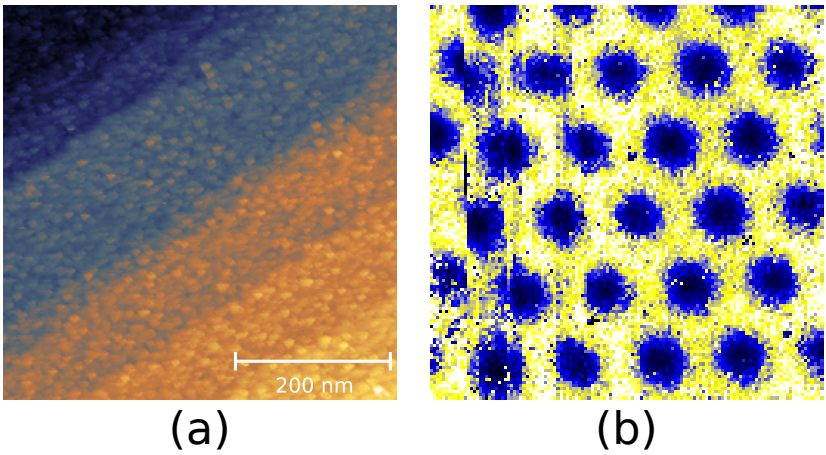

Figure 4.15: Formation of superconducting vortices on multilayers Ru/Nb(110): (a) Topographic image of the $Ru_{6-8-\text{ML}}$/Nb(110). $I = 100$ pA, $U = 5$ mV. (b) Grid STS measurement at $E = 0$ eV. $I = 100$ pA, $U = 5$ mV, $U_{mod} = 100$ µV. As on the previous sample with thinner Ru layer, SC vortices are visible (darker blue disks) whereas the sample is superconducting everywhere else (brighter area).

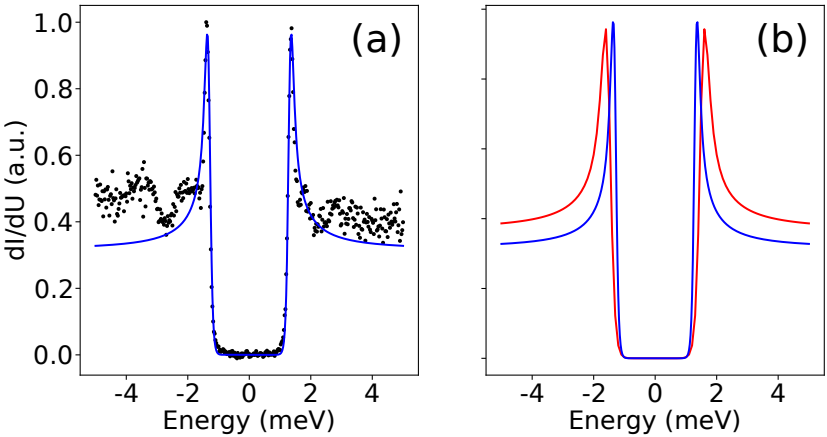

Figure 4.16: Superconducting gap of $Ru_{6-8-ML}/Nb(110)$: (a) Superconducting gap measured by STS on $Ru_{6\text{-}8\text{-}ML}/Nb(110)$ (black dots) and corresponding BCS fit performed on the data (blue curve). (b) Comparison of the BCS fit performed on free Nb(110) (red curve) and on $Ru_{6-8-ML}/Nb(110)$ (blue curve). Experimental data recorded at $I = 100$ pA, $U = 5$ mV, $U_{mod} = 100$ µV.

Conclusion and outlook

In the framework of this thesis, we investigated properties of sub-ML Co/Ru(0001) and multilayers Ru/Nb(110). The goal of this work was to provide confirmation of theoretical predictions about MBS emergence on a skyrmion-SC hybrid, and to provide meaningful experimental insights about the underlying physical properties behind their emergence and the dynamics of skyrmions hosting those states.

After successfully measuring the superconducting gap of a Ru single crystal, and confirming its conventional superconductor nature, we investigated what was necessary for the Co deposition on the surface to be successful. We discovered that two key parameters need to be looked after carefully: the carbon impurities surface concentration in one hand, and the constant temperature of the crystal during deposition in the other. We saw that if these two parameters are not optimal, a new stacking phase of the Co sub-ML appears, the ε-phase. We could resolve the atomic structure and confirm that the positions of the atoms matches the ones of the known ε-Co crystal lattice. This phase does not appear to be magnetic, and we could see that it was a highly transparent interface to Cooper-pairs, unlike the regular hcp-stacking of Co/Ru(0001). Working with theory, we gained insights on the proximity effect mechanisms in play for this system, namely the matching of the Fermi surfaces of Co and Ru. We saw that this difference in the transparency of the interfaces for the two stackings could be explained by the fact that the calculated Fermi surface of hcp-Co forms an angle of 30° with the one of Ru, while the one of fcc-Co trusted to be similar to the one of ε-Co superimpose with the Fermi surface of Ru.

Furthermore, we reproduced the formation of single isolated skyrmions from the spin-spiral ground state of the hcp phase of Co/Ru(0001), and studied their size dependency with an applied magnetic field. We could successfully observe the reduction of the skyrmions' radii, down to the point where the applied field reached a critical value, leading to the unwinding of the skyrmions and

to their collapse. We could compare this with theoretical calculations, giving us insights on the interactions in play in the skyrmions' dynamics. We could therefore confirm that the dipolar energy could be correctly approximated by an effective anisotropy. By doing so, the saddle point between single skyrmions and the ferromagnetic state was investigated. We found a very good agreement between experiment and calculations for the collapse field value.

To confirm theoretical predictions and propose new systems to work on, we studied the possibility to observe MBS when skyrmions were formed on Co/Ru(0001), and the superconductivity restored afterward. We could confirm that it is possible for skyrmions to exist on a superconducting surface, and that the Meissner effect is not affecting their shape. Eventually, we could observe states resembling MZS on several occurrences. Yet, no MBS could be linked to the existence of skrymion-SC hybrid system, confirming that skyrmions with an odd winding number do not lead to MBS emergence. Furthermore, we did not find a reproducible procedure to observe these states, so we could not link the observation of MZS to a given structure. Yet, we investigated the possibility for other structures like the magnetic trijunction in presence of a magnetic field, and skyrmions with winding number $n = 0$. While we did not observe MBS on the former, the formation of the later could not be achieved because of the magnetic moments being pinned on local defects.

To overcome the limitations of Co/Ru(0001), we proposed the model system of Co/Ru/Nb(110), meant to form skyrmions with the preserved DMI present of the Co/Ru(0001), and couple them with superconducting vortices coming from the Nb(110) substrate. To verify the feasibility of the project, we studied the deposition of multilayers of Ru on Nb(110) and the proximity effect on the resulting surface. We successfully deposited multilayers of Ru on the Nb(110) surface and verified that the superconducting properties of the latter are transmitted, with almost no loss, to the former; the superconducting gap value is reduced by 13% when 6 to 8 monolayers of Ru are deposited, and superconducting vortices are still visible on the surface when a magnetic field above the first critical field of Nb is applied. These promising results indicate that, in the future, skyrmions may be successfully coupled to superconducting vortices, which could be the key to observe MBS on skyrmions.

Tuning of the deposition still needs to be done, as the Ru needs to grow in its hcp stacking direction for this operation to be successful. Indeed, the key ingredient for the skyrmion formation on Co/Ru(0001) is the small DMI,

and this needs to be preserved. But we saw that Ru does not grow in this direction, and a rectangular lattice seems to be the preferred growth mode. This effect may come from the NbO surface reconstruction coming naturally on Nb(110), as we saw that Ru/Nb(110) present a structure similar to this reconstruction, even after the deposition of 8 monolayers. In the future, it may be necessary to deposit Ru on the Nb(110) surface free from NbO to allow the Ru monolayers to grow in the desired direction, and to finally grow Co sub-ML and study the MBS on skyrmions coupled with superconducting vortices.

List of Figures

Bibliography

[1] David P. DiVincenzo. “Quantum Computation”. In: Science 270.5234 (1995), pp. 255–261. DOI: 10.1126/science.270.5234.255.

[2] Seth Lloyd. “A Potentially Realizable Quantum Computer”. In: Science 261.5128 (1993), pp. 1569–1571. DOI: 10.1126/science.261.5128.1569.

[3] Jarryd J. Pla et al. “A single-atom electron spin qubit in silicon”. In: Nature 489.7417 (2012), pp. 541–545. DOI: 10.1038/nature11449.

[4] Toshio Miyamachi et al. “Stabilizing the magnetic moment of single holmium atoms by symmetry”. In: Nature 503.7475 (2013), pp. 242–246. DOI: 10.1038/nature12759.

[5] Daniel Loss and David P. DiVincenzo. “Quantum computation with quantum dots”. In: Phys. Rev. A 57.1 (1998), pp. 120–126. DOI: 10.1103/PhysRevA.57.120.

[6] Yuriy Makhlin, Gerd Schön, and Alexander Shnirman. “Quantum-state engineering with Josephson-junction devices”. In: Rev. Mod. Phys. 73.2 (2001), pp. 357–400. DOI: 10.1103/RevModPhys.73.357.

[7] Nikolai S Kiselev et al. “Chiral skyrmions in thin magnetic films: new objects for magnetic storage technologies?” In: Journ. Phys. D 44.39 (2011), p. 392001. DOI: 10.1088/0022-3727/44/39/392001.

[8] Albert Fert, Nicolas Reyren, and Vincent Cros. “Magnetic skyrmions: advances in physics and potential applications”. In: Nature Reviews Materials 2.7 (2017), p. 17031. DOI: 10.1038/natrevmats.2017.31.

[9] Takayuki Nozaki et al. “Brownian motion of skyrmion bubbles and its control by voltage applications”. In: Appl. Phys. Lett. 114.1 (2019), p. 012402. DOI: 10.1063/1.5070101.

[10] Jeremy L. O’Brien. “Optical Quantum Computing”. In: Science 318.5856 (2007), pp. 1567–1570. DOI: 10.1126/science.1142892.

[11] Achim Rosch. “Electric control of skyrmions”. In: Nature Nanotechnology 12.2 (2017), pp. 103–104. DOI: 10.1038/nnano.2016.244.

[12] Shijiang Luo and Long You. “Skyrmion devices for memory and logic applications”. In: APL Materials 9.5 (2021), p. 050901. DOI: 10.1063/5.0042917.

[13] T.H.R. Skyrme. “A unified field theory of mesons and baryons”. In: Nuclear Physics 31 (1962), pp. 556–569. DOI: 10.1016/0029-5582(62)90775-7.

[14] S. Mühlbauer et al. “Skyrmion Lattice in a Chiral Magnet”. In: Science 323.5916 (2009), pp. 915–919. DOI: 10.1126/science.1166767.

[15] X. Z. Yu et al. “Real-space observation of a two-dimensional skyrmion crystal”. In: Nature 465.7300 (2010), pages 901–904. DOI: 10.1038/nature09124.

[16] Marie Hervé et al. “Stabilizing spin spirals and isolated skyrmions at low magnetic field exploiting vanishing magnetic anisotropy”. In: Nature Communications 9.1 (2018), p. 1015. DOI: 10.1038/s41467-018-03240-w.

[17] Niklas Romming et al. “Writing and Deleting Single Magnetic Skyrmions”. In: Science 341.6146 (2013), pp. 636–639. DOI: 10.1126/science.1240573.

[18] Vegard Flovik et al. “Generation of single skyrmions by picosecond magnetic field pulses”. In: Phys. Rev. B 96.14 (2017), p. 140411. DOI: 10.1103/PhysRevB.96.140411.

[19] Guoqiang Yu et al. “Room-Temperature Skyrmion Shift Device for Memory Application”. In: Nano Letters 17.1 (2017), pp. 261–268. DOI: 10.1021/acs.nanolett.6b04010.

[20] Christina Psaroudaki and Christos Panagopoulos. “Skyrmion Qubits: A New Class of Quantum Logic Elements Based on Nanoscale Magnetization”. In: Phys. Rev. Lett. 127.6 (2021), p. 067201. DOI: 10.1103/PhysRevLett.127.067201.

[21] Guang Yang et al. “Majorana bound states in magnetic skyrmions”. In: Phys. Rev. B 93.22 (2016), p. 224505. DOI: 10.1103/PhysRevB.93.224505.

[22] Stefan Rex, Igor V. Gornyi, and Alexander D. Mirlin. “Majorana bound states in magnetic skyrmions imposed onto a superconductor”. In: Phys. Rev. B 100.6 (2019), p. 064504. DOI: 10.1103/PhysRevB.100.064504.

[23] Frank Wilczek. “Majorana returns”. In: Nature Physics 5.9 (2009), pp. 614–618. DOI: 10.1038/nphys1380.

[24] Sankar Das Sarma, Michael Freedman, and Chetan Nayak. “Majorana zero modes and topological quantum computation”. In: npj Quantum Information 1.1 (2015), p. 15001. DOI: 10.1038/npjqi.2015.1.

[25] Stevan Nadj-Perge et al. “Observation of Majorana fermions in ferromagnetic atomic chains on a superconductor”. In: Science 346.6209 (2014), pp. 602–607. DOI: 10.1126/science.1259327.

[26] V. Mourik et al. “Signatures of Majorana Fermions in Hybrid Superconductor-Semiconductor Nanowire Devices”. In: Science 336.6084 (2012), pp. 1003–1007. DOI: 10.1126/science.1222360.

[27] S. M. Albrecht et al. “Exponential protection of zero modes in Majorana islands”. In: Nature 531.7593 (2016), pp. 206–209. DOI: 10.1038/nature17162.

[28] Bert Voigtlaender. Scanning Probe Microscopy. Heidelberg: Springer, 2015. ISBN: 978-3-662-45239-4.

[29] J. Bardeen. “Tunnelling from a Many-Particle Point of View”. In: Phys. Rev. Lett. 6.2 (1961), pp. 57–59. DOI: 10.1103/PhysRevLett.6.57.

[30] J. Tersoff and D. R. Hamann. “Theory of the scanning tunneling microscope”. In: Phys. Rev. B 31.2 (1985), pp. 805–813. DOI: 10.1103/PhysRevB.31.805.

[31] Paul K. Hansma and Jerry Tersoff. “Scanning tunneling microscopy”. In: Journal of Applied Physics 61.2 (1987), R1–R24. DOI: 10.1063/1.338189.

[32] F N Hooge, T G M Kleinpenning, and L K J Vandamme. “Experimental studies on 1/f noise”. In: Reports on Progress in Physics 44.5 (1981), pp. 479–532. DOI: 10.1088/0034-4885/44/5/001.

[33] G. Binnig et al. “Surface Studies by Scanning Tunneling Microscopy”. In: Phys. Rev. Lett. 49.1 (1982), pp. 57–61. DOI: 10.1103/PhysRevLett.49.57.

[34] G. Binnig and D. P. E. Smith. “Singletube threedimensional scanner for scanning tunneling microscopy”. In: Review of Scientific Instruments 57.8 (1986), pp. 1688–1689. DOI: 10.1063/1.1139196.

[35] M Bode. “Spin-polarized scanning tunnelling microscopy”. In: Reports on Progress in Physics 66.4 (2003), pp. 523–582. DOI: 10.1088/0034-4885/66/4/203.

[36] N. Néel et al. “Tunneling Anisotropic Magnetoresistance at the Single-Atom Limit”. In: Phys. Rev. Lett. 110.3 (2013), p. 041114. DOI: 10.1103/PhysRevLett.110.037202.

[37] Johannes Schöneberg et al. “Tunneling anisotropic magnetoresistance via molecular π orbitals of Pb dimers”. In: Phys. Rev. B 97.4 (2018), p. 041114. DOI: 10.1103/PhysRevB.97.041114.

[38] Heike Kamerlingh Onnes. “The Superconductivity of Mercury”. In: Leiden Community 120b, 122b, 124c (1911).

[39] J. Bardeen, L. N. Cooper, and J. R. Schrieffer. “Microscopic Theory of Superconductivity”. In: Phys. Rev. 106.1 (1957), pp. 162–164. DOI: 10.1103/PhysRev.106.162.

[40] Michael Tinkham. Introduction to superconductivity. 2. ed. Dover books on physics. Mineola, NY: Dover Publ., 2004. ISBN: 0486435032.

[41] Leon N. Cooper. “Bound Electron Pairs in a Degenerate Fermi Gas”. In: Phys. Rev. 104.4 (1956), pp. 1189–1190. DOI: 10.1103/PhysRev.104.1189.

[42] Neil W. Ashcroft and N. David Mermin. Solid state physics. Singapore [u.a.]: Brooks/Coole Thomson Learning, 2005. ISBN: 0030839939.

[43] W. Meissner and R. Ochsenfeld. “Ein neuer Effekt bei Eintritt der Supraleitfähigkeit”. In: Naturwissenschaften 21.44 (1933), pp. 787–788. DOI: 10.1007/BF01504252.

[44] Charles Kittel. Introduction to solid state physics. 8. ed. [Internat. ed.] Hoboken, NJ: Wiley, 2005. ISBN: 9780471680574.

[45] R. Holm and W. Meissner. “Messungen mit Hilfe von flüssigem Helium. XIII”. In: Zeitschrift für Physik 74.11 (1932), pp. 715–735. DOI: 10.1007/BF01340420.

[46] Hans Meissner. “Superconductivity of Contacts with Interposed Barriers”. In: Phys. Rev. 117.3 (1960), pp. 672–680. DOI: 10.1103/PhysRev.117.672.

[47] J.P. Liu, Z. Zhang, and G. Zhao. Skyrmions: Topological Structures, Properties, and Applications. Series in Materials Science and Engineering. 2016. ISBN: 9781315284156.

[48] Stefan Waldmann. Topology : An Introduction. Springer eBook Collection. Cham: Springer, 2014. ISBN: 9783319096803.

[49] A. N. Bogdanov and U. K. RöSSler. “Chiral Symmetry Breaking in Magnetic Thin Films and Multilayers”. In: Phys. Rev. Lett. 87.3 (2001), p. 037203. DOI: 10.1103/PhysRevLett.87.037203.

[50] Naoto Nagaosa and Yoshinori Tokura. “Topological properties and dynamics of magnetic skyrmions”. In: Nature Nanotechnology 8.12 (2013), pp. 899–911. DOI: 10.1038/nnano.2013.243.

[51] I. Dzyaloshinsky. “A thermodynamic theory of weak ferromagnetism of antiferromagnetics”. In: Journal of Physics and Chemistry of Solids 4.4 (1958), pp. 241–255. DOI: 10.1016/0022-3697(58)90076-3.

[52] Tôru Moriya. “Anisotropic Superexchange Interaction and Weak Ferromagnetism”. In: Phys. Rev. 120.1 (1960), pp. 91–98. DOI: 10.1103/PhysRev.120.91.

[53] Stefan Heinze et al. “Spontaneous atomic-scale magnetic skyrmion lattice in two dimensions”. In: Nature Physics 7.9 (2011), pp. 713–718. DOI: 10.1038/nphys2045.

[54] Xiao-Liang Qi and Shou-Cheng Zhang. “Topological insulators and superconductors”. In: Rev. Mod. Phys. 83.4 (2011), pp. 1057–1110. DOI: 10.1103/RevModPhys.83.1057.

[55] B. Andrei Bernevig. Topological insulators and topological superconductors. Ed. by Taylor L. Hughes. Princeton [u.a.]: Princeton University Press, 2013. ISBN: 069115175X.

[56] Topodcondmat.org. https://topocondmat.org/.

[57] Ettore Majorana and Luciano Maiani. "A symmetric theory of electrons and positrons". In: Ettore Majorana Scientific Papers: On occasion of the centenary of his birth. Ed. by Giuseppe Franco Bassani. Berlin, Heidelberg: Springer Berlin Heidelberg, 2006. DOI: 10.1007/978-3-540-48095-2_10.

[58] Ettore Majorana. "Teoria simmetrica dell'elettrone e del positrone". In: Il Nuovo Cimento 14.4 (2008), p. 171. DOI: 10.1007/BF02961314.

[59] Masatoshi Sato and Yoichi Ando. "Topological superconductors: a review". In: Reports on Progress in Physics 80.7 (2017), p. 076501. DOI: 10.1088/1361-6633/aa6ac7.

[60] A Yu Kitaev. "Unpaired Majorana fermions in quantum wires". In: Physics-Uspekhi 44.10S (2001), pp. 131–136. DOI: 10.1070/1063-7869/44/10s/s29.

[61] Takahiro Fukui et al. "Bulk-Edge Correspondence for Chern Topological Phases: A Viewpoint from a Generalized Index Theorem". In: Journal of the Physical Society of Japan 11 (2012), p. 114602. DOI: 10.1143/JPSJ.81.114602.

[62] Nicholas Sedlmayr et al. "Bulk boundary correspondence and the existence of Majorana bound states on the edges of 2D topological superconductors". In: Phys. Rev. B 96.18 (2017), p. 184516. DOI: 10.1103/PhysRevB.96.184516.

[63] Chetan Nayak et al. "Non-Abelian anyons and topological quantum computation". In: Rev. Mod. Phys. 80.3 (2008), pp. 1083–1159. DOI: 10.1103/RevModPhys.80.1083.

[64] A.Yu. Kitaev. "Fault-tolerant quantum computation by anyons". In: Annals of Physics 303.1 (2003), pp. 2–30. DOI: 10.1016/S0003-4916(02)00018-0.

[65] Jelena Klinovaja, Peter Stano, and Daniel Loss. "Transition from Fractional to Majorana Fermions in Rashba Nanowires". In: Phys. Rev. Lett. 109.23 (2012), p. 236801. DOI: 10.1103/PhysRevLett.109.236801.

[66] Falko Pientka, Leonid I. Glazman, and Felix von Oppen. "Topological superconducting phase in helical Shiba chains". In: Phys. Rev. B 88.15 (2013), p. 155420. DOI: 10.1103/PhysRevB.88.155420.

[67] Se Kwon Kim, Sumanta Tewari, and Yaroslav Tserkovnyak. "Control and braiding of Majorana fermions bound to magnetic domain walls". In: Phys. Rev. B 92.2 (2015), p. 020412. DOI: 10.1103/PhysRevB.92.020412.

[68] Bernd Braunecker et al. "Spin-selective Peierls transition in interacting one-dimensional conductors with spin-orbit interaction". In: Phys. Rev. B 82.4 (2010), p. 045127. DOI: 10.1103/PhysRevB.82.045127.

[69] Utkan Güngördü, Shane Sandhoefner, and Alexey A. Kovalev. "Stabilization and control of Majorana bound states with elongated skyrmions". In: Phys. Rev. B 97.11 (2018), p. 115136. DOI: 10.1103/PhysRevB.97.115136.

[70] Jinjun Ding, Xiaofei Yang, and Tao Zhu. "Manipulating current induced motion of magnetic skyrmions in the magnetic nanotrack". In: Journal of Physics D: Applied Physics 48.11 (2015), p. 115004. DOI: 10.1088/0022-3727/48/11/115004.

[71] Gerbold C. Ménard et al. "Isolated pairs of Majorana zero modes in a disordered superconducting lead monolayer". In: Nature Communications 10.1 (2019), p. 2587. DOI: 10.1038/s41467-019-10397-5.

[72] T. Balashov, M. Meyer, and W. Wulfhekel. "A compact ultrahigh vacuum scanning tunneling microscope with dilution refrigeration". In: Review of Scientific Instruments 89.11 (2018), p. 113707. DOI: 10.1063/1.5043636.

[73] BF-LD250 Cryogen-Free Dilution Refrigerator System by Bluefors. https://bluefors.com/products/ld-dilution-refrigerator/.

[74] O V Lounasmaa. "Dilution refrigeration". In: Journal of Physics E: Scientific Instruments 12.8 (1979), pp. 668–675. DOI: 10.1088/0022-3735/12/8/001.

[75] David S. Betts. An introduction to millikelvin technology. 1. publ. Cambridge studies in low temperature physics ; 1. Cambridge [u.a.]: Cambridge Univ. Pr., 1989. ISBN: 0521344565.

[76] Frank Pobell. Matter and methods at low temperatures : with 28 tables, and 81 problems. 3., rev. and expanded ed. Berlin: Springer, 2007. ISBN: 9783540463566.

[77] MercuryiPS by Oxford Instruments. https://nanoscience.oxinst.com/accessories/mercuryips.

[78] THS119 gaas ion implanted planar type hall sensor by Toshiba Co.

[79] Yasuhiro Nakamura, Akio Iwasa, and Akio Fukushima. "Simple Method for Measurement of Decay Rate in Superconducting Magnet". In: Japanese Journal of Applied Physics 34.Part 1, No. 7A (1995), pp. 3741–3745. DOI: 10.1143/jjap.34.3741.

[80] Harald Ibach. Physics of surfaces and interfaces. Berlin: Springer, 2006. ISBN: 3540347097.

[81] David Briggs and John T. Grant, eds. Surface analysis by Auger and X-ray photoelectron spectroscopy. Chichester [u.a.]: IM Publ. [u.a.], 2003. ISBN: 1901019047.

[82] Rafael Lopes et al. "Epitaxial growth of Co on stepped Ru(0001): Stabilization of CoRu magnetic surface alloy". In: Surface Science 692 (2020), p. 121512. DOI: doi.org/10.1016/j.susc.2019.121512.

[83] R.G. Musket et al. "Preparation of atomically clean surfaces of selected elements: A review". In: Applications of Surface Science 10.2 (1982), pp. 143–207. DOI: doi.org/10.1016/0378-5963(82)90142-8.

[84] Petr Klapetek. Quantitative Data Processing in Scanning Probe Microscopy: SPM Applications for Nanometrology. Elsevier, 2018.

[85] J. K. Hulm and B. B. Goodman. "Superconducting Properties of Rhenium, Ruthenium, and Osmium". In: Phys. Rev. 106.4 (1957), pp. 659–671. DOI: 10.1103/PhysRev.106.659.

[86] Marie Hervé et al. "Large tunneling anisotropic magnetoresistance mediated by surface states". In: Phys. Rev. B 97.22 (2018), p. 220406. DOI: 10.1103/PhysRevB.97.220406.

[87] Víctor Antonio de la Peña OShea et al. "Electronic and magnetic structure of bulk cobalt: The α, β, and -phases from density functional theory calculations". In: The Journal of Chemical Physics 133.2 (2010), p. 024701. DOI: 10.1063/1.3458691.

[88] Shouheng Sun and C. B. Murray. “Synthesis of monodisperse cobalt nanocrystals and their assembly into magnetic superlattices (invited)”. In: Journal of Applied Physics 85.8 (1999), pp. 4325–4330. DOI: 10.1063/1.370357.

[89] Specs EBE1 evaporator. https://www.specs-group.com/nc/specs/products/detail/ebe-1/.

[90] Loic Mougel et al. “Instability of skyrmions in magnetic fields”. In: Applied Physics Letters 116.26 (2020), p. 262406. DOI: 10.1063/5.0013488.

[91] Niklas Romming et al. “Field-Dependent Size and Shape of Single Magnetic Skyrmions”. In: Phys. Rev. Lett. 114.17 (2015), p. 177203. DOI: 10.1103/PhysRevLett.114.177203.

[92] S. Rohart, J. Miltat, and A. Thiaville. “Path to collapse for an isolated Néel skyrmion”. In: Phys. Rev. B 93.21 (2016), p. 214412. DOI: 10.1103/PhysRevB.93.214412.

[93] Anne Bernand-Mantel et al. “The skyrmion-bubble transition in a ferromagnetic thin film”. In: SciPost Phys. 4.5 (2018), p. 27. DOI: 10.21468/SciPostPhys.4.5.027.

[94] A O Leonov et al. “The properties of isolated chiral skyrmions in thin magnetic films”. In: New Journal of Physics 18.6 (2016), p. 392001. DOI: 10.1088/1367-2630/18/6/065003.

[95] E. Wigner. “The transition state method”. In: Trans. Faraday Soc. 34.0 (1938), pp. 29–41. DOI: 10.1039/TF9383400029.

[96] Graeme Henkelman, Blas P. Uberuaga, and Hannes Jónsson. “A climbing image nudged elastic band method for finding saddle points and minimum energy paths”. In: J. Chem. Phys. 113.22 (2000), pp. 9901–9904. DOI: 10.1063/1.1329672.

[97] Pavel F Bessarab, Valery M Uzdin, and Hannes Jónsson. “Harmonic transition-state theory of thermal spin transitions”. In: Phys. Rev. B 85 (2012), p. 184409. DOI: 10.1103/PhysRevB.85.184409.

[98] Pavel F Bessarab, Valery M Uzdin, and Hannes Jónsson. “Method for finding mechanism and activation energy of magnetic transitions, applied to skyrmion and antivortex annihilation”. In: Computer Physics Communications 196 (2015), pp. 335–347. DOI: 10.1016/j.cpc.2015.07.001.

[99] S. von Malottki et al. “Enhanced skyrmion stability due to exchange frustration”. In: Scientific Reports 7.1 (2017), p. 12299. DOI: 10.1038/s41598-017-12525-x.

[100] Pavel F Bessarab et al. “Lifetime of racetrack skyrmions”. In: Sci. Rep. 8.1 (2018), p. 3433. DOI: 10.1038/s41598-018-21623-3.

[101] Stephan von Malottki et al. “Skyrmion lifetime in ultrathin films”. In: Phys. Rev. B 99.6 (2019), p. 060409. DOI: 10.1103/PhysRevB.99.060409.

[102] Kirsten von Bergmann et al. “Tunneling anisotropic magnetoresistance on the atomic scale”. In: Phys. Rev. B 86.13 (2012), p. 134422. DOI: 10.1103/PhysRevB.86.134422.

[103] A. N. Bogdanov and A Hubert. “Thermodynamically stable magnetic vortex states in magnetic crystals”. In: J. Magn. Magn. Mater. 138 (1994), pp. 255–269. DOI: 10.1016/0304-8853(94)90046-9.

[104] Murray Neff Wilson et al. “Chiral skyrmions in cubic helimagnet films: The role of uniaxial anisotropy”. In: Phys. Rev. B 89.9 (2014), p. 094411. DOI: 10.1103/PhysRevB.89.094411.

[105] Benjamin Heil, Achim Rosch, and Jan Masell. “Universality of annihilation barriers of large magnetic skyrmions in chiral and frustrated magnets”. In: Phys. Rev. B 100.13 (2019), p. 134424. DOI: 10.1103/PhysRevB.100.134424.

[106] A. N. Bogdanov and A Hubert. “The stability of vortex-like structures in uniaxial ferromagnets”. In: J. Magn. Magn. Mater. 195 (1999), pp. 182–192. DOI: 10.1016/S0304-8853(98)01038-5.

[107] Gideon P. Müller et al. “Spirit : Multifunctional framework for atomistic spin simulations”. In: Phys. Rev. B 99.22 (2019), p. 224414. DOI: 10.1103/PhysRevB.99.224414.

[108] Ernst Feldtkeller and Harry Thomas. “Struktur und Energie von Blochlinien in dünnen ferromagnetischen Schichten”. In: Physik der Kondensierten Materie 4.1 (1965), pp. 8–14. DOI: 10.1007/BF02423256.

[109] Berthold Jäck et al. “Observation of a Majorana zero mode in a topologically protected edge channel”. In: Science 364.6447 (2019), pp. 1255–1259. DOI: 10.1126/science.aax1444.

[110] Luh Yu. “Bound state in superconductors with paramagnetic impurities”. In: Acta Phys. Sin 21.1 (1965), pp. 75–91. DOI: 10.7498/aps.21.75.

[111] Hiroyuki Shiba. “Classical spins in superconductors”. In: Progress of theoretical Physics 40.3 (1968), pp. 435–451. DOI: 10.1143/PTP.40.435.

[112] AI Rusinov. “Theory of gapless superconductivity in alloys containing paramagnetic impurities”. In: Sov. Phys. JETP 29.6 (1969), pp. 1101–1106.

[113] Alexander V Balatsky, Ilya Vekhter, and Jian-Xin Zhu. “Impurity-induced states in conventional and unconventional superconductors”. In: Reviews of Modern Physics 78.2 (2006), p. 373. DOI: 10.1103/RevModPhys.78.373.

[114] Stefan Rex, Igor V. Gornyi, and Alexander D. Mirlin. “Majorana modes in emergent-wire phases of helical and cycloidal magnet-superconductor hybrids”. In: Phys. Rev. B 102.22 (2020), p. 224501. DOI: 10.1103/PhysRevB.102.224501.

[115] Filipp N. Rybakov and Nikolai S. Kiselev. “Chiral magnetic skyrmions with arbitrary topological charge”. In: Phys. Rev. B 99.6 (2019), p. 064437. DOI: 10.1103/PhysRevB.99.064437.

[116] A. P. Petrovi et al. “Skyrmion-(Anti)Vortex Coupling in a Chiral Magnet-Superconductor Heterostructure”. In: Phys. Rev. Lett. 126.11 (2021), p. 117205. DOI: 10.1103/PhysRevLett.126.117205.

[117] Julian Eisenstein. “Superconducting Elements”. In: Rev. Mod. Phys. 26.3 (1954), pp. 277–291. DOI: 10.1103/RevModPhys.26.277.

[118] B. T. Matthias, T. H. Geballe, and V. B. Compton. “Superconductivity”. In: Rev. Mod. Phys. 35.1 (1963), pp. 1–22. DOI: 10.1103/RevModPhys.35.1.

[119] Artem B. Odobesko et al. “Preparation and electronic properties of clean superconducting Nb(110) surfaces”. In: Phys. Rev. B 99.11 (2019), p. 115437. DOI: 10.1103/PhysRevB.99.115437.

[120] A. S. Razinkin and M. V. Kuznetsov. “Scanning tunneling microscopy (STM) of low-dimensional NbO structures on the Nb(110) surface”. In: The Physics of Metals and Metallography 110.6 (2010), pp. 531–541. DOI: 10.1134/S0031918X10120033.

[121] “Oxygen-induced surface structure of Nb(110)”. In: Surface Science 471.1 (2001), pp. 209–218. DOI: 10.1016/S0039-6028(00)00908-0.

[122] ASM International. Handbook Committee, H. Baker, and H. Okamoto. ASM Handbook: Alloy phase diagrams. Volume 3. ASM International. ISBN: 9781615031900.

Appendix: Derivation of the MZS exchange operators

We recall the identities for MZS creation and annihilation operators:

$$\gamma_n\gamma_m + \gamma_m\gamma_n = 0, \tag{1}$$
$$\gamma_n^2 = 1. \tag{2}$$

We can then directly obtain:

$$\gamma_n\gamma_m = -\gamma_m\gamma_n, \tag{3}$$

which yields:

$$(\gamma_n\gamma_m)^2 = -\gamma_m\gamma_n\gamma_n\gamma_m \tag{4}$$
$$= -i\gamma_m\gamma_m \tag{5}$$
$$= -1. \tag{6}$$

Therefore, we can write the MZS exchange operator of two Majorana states n and m:

$$U_{\gamma_n\gamma_m} = e^{\frac{\pi}{4}\gamma_n\gamma_m} = \frac{1}{\sqrt{2}}\left(1 + \gamma_n\gamma_m\right). \tag{7}$$

If we consider a system with two fermionic states, either occupied or unoccupied, the basis is $|00\rangle, |11\rangle, |01\rangle, |10\rangle$, with the total wave function of the system having the form:

$$|\psi\rangle = a_{00}|00\rangle + a_{11}|11\rangle + a_{01}|01\rangle + a_{10}|10\rangle. \tag{8}$$

The system then has four MZS, and we can calculate how the operators act on the basis:

γ_1	$c_1 + c_1^\dagger$	$\|00\rangle \rightarrow \|10\rangle$ $\|11\rangle \rightarrow \|01\rangle$ $\|01\rangle \rightarrow \|11\rangle$ $\|10\rangle \rightarrow \|00\rangle$
γ_2	$i\left(c_1 - c_1^\dagger\right)$	$\|00\rangle \rightarrow -i\|10\rangle$ $\|11\rangle \rightarrow i\|01\rangle$ $\|01\rangle \rightarrow -i\|11\rangle$ $\|10\rangle \rightarrow i\|00\rangle$
γ_3	$c_2 + c_2^\dagger$	$\|00\rangle \rightarrow \|01\rangle$ $\|11\rangle \rightarrow \|10\rangle$ $\|01\rangle \rightarrow \|00\rangle$ $\|10\rangle \rightarrow \|11\rangle$
γ_4	$i\left(c_2 - c_2^\dagger\right)$	$\|00\rangle \rightarrow -i\|01\rangle$ $\|11\rangle \rightarrow i\|10\rangle$ $\|01\rangle \rightarrow -i\|00\rangle$ $\|10\rangle \rightarrow i\|11\rangle$

Table 1: Action of the Majorana operators on the fermion states basis.

$U_{\gamma_1\gamma_2}$	$\frac{1}{\sqrt{2}}(1+\gamma_1\gamma_2)$	$\|00\rangle \rightarrow e^{-i\frac{\pi}{4}}\|00\rangle$ $\|11\rangle \rightarrow e^{i\frac{\pi}{4}}\|11\rangle$ $\|01\rangle \rightarrow e^{-i\frac{\pi}{4}}\|01\rangle$ $\|10\rangle \rightarrow e^{i\frac{\pi}{4}}\|10\rangle$
$U_{\gamma_2\gamma_3}$	$\frac{1}{\sqrt{2}}(1+\gamma_2\gamma_3)$	$\|00\rangle \rightarrow \|00\rangle - i\|11\rangle$ $\|11\rangle \rightarrow \|11\rangle - i\|00\rangle$ $\|01\rangle \rightarrow \|01\rangle - i\|10\rangle$ $\|10\rangle \rightarrow \|10\rangle - i\|01\rangle$
$U_{\gamma_3\gamma_4}$	$\frac{1}{\sqrt{2}}(1+\gamma_3\gamma_4)$	$\|00\rangle \rightarrow e^{-i\frac{\pi}{4}}\|00\rangle$ $\|11\rangle \rightarrow e^{i\frac{\pi}{4}}\|11\rangle$ $\|01\rangle \rightarrow e^{i\frac{\pi}{4}}\|01\rangle$ $\|10\rangle \rightarrow e^{-i\frac{\pi}{4}}\|10\rangle$

Table 2: Action of the exchange operators on the state basis.

List of Abbreviations

AES	Auger electron spectroscopy
BCS	Bardeen-Cooper-Schrieffer
DDI	Dipole-dipole interaction
DFT	Density functional theory
DMI	Dzyaloshinskii-Moriya interaction
DOS	Density of states
fcc	Face-centered cubic structure
GNEB	Geodesic nudged elastic band
hcp	Hexagonal close-packed structure
HV	High voltage
JT	Joule-Thomson
LDOS	Local density of states
LEED	Low-energy electron diffraction
LHe	Liquid helium
LN_2	Liquid nitrogen
MAE	Magnetocrystalline anisotropy
MBE	Molecular beam epitaxy
MBS	Majorana bound states
ML	Monolayer
MZS	Majorana zero states
NEB	Nudged elastic band
PCB	Printed circuit board
SC	Superconducting/Superconductor
SOC	Spin-orbit coupling
SOI	Spin-orbit interaction
SP-STM	Spin-polarized Scanning tunneling microscopy
STM	Scanning tunneling microscopy
STS	Scanning tunneling spectroscopy
TAMR	Tunneling anisotropic magnetoresistance
TMP	Turbo molecular pump
TMR	Tunneling magnetoresistance
UHV	Ultra high vacuum
YRS	Yu-Rusinov-Shiba

Acknowledgements

This has been a truly great experience. I have countless memories of the hours spent in the lab, and in front of my computer, trying to solve the mystery of physics. I could not have made it this far without the help and support of the people that were in my life and the ones I met along the way. Therefore, my most sincere gratitude goes to...

... Prof. Dr. Wulf Wulfhekel for the offered chance to do my PhD in his group, for all the discussions we had together about physics, but not only, and for all the support he showed even in the hardest times of this work.

... Prof. Dr. Markus Garst who accepted to be the second referee of this thesis.

... Prof. Dr. Bertrand Dupé and Dr. Patrick Bühl for the theoretical support for the experimental results they provided.

... Dr. Marie Hervé, without whom this project would not have been possible, and for the support she gave me.

... Dr. Timofey Balashov for giving me the help I needed all the way from the beginning to the end. I also thank him and his wife Inna for the friendship moments we had.

... Dr. Hung-Hsiang Yang, and Dr. Hongyan Chen for the help and support in the lab, always present when I needed them.

... the SPP2137 and all its member for making this project possible, and for all the interesting projects I could discover during the meetings.

... Jannis Ret and all the members of the electronics workshop for the kind patience they had.

... Michael Meyer and all the members of the mechanical workshop for all the help they provided, sometimes several times a day.

... all the students I had under my supervision in the lab, Anika Müller, Pavao Brica and Samuel Tesfamariam, who helped me to understand a lot of things during our discussions.

... all members of our group, still present or not, including, Timo, Julian, Gabriel, Lukas, Kevin, Mirjam, Jasmin, Jinjie, Sergey, Vibhuti, Thomas, Fang and Haoran for the best workplace I have ever been, for the unforgettable memories and for all the discussions we had together.

... all my friends and family, who are but one big entity, for their unfailing support, and for always believing I could do it. Thank you mom, dad, Christian, Marianne, Luc, Noémie, Nelson, Berenger and Guillaume. I would also thank my uncle Michel, and my grandfather René, who left us.

... finally, a special thanks to Laëtitia, the special one, without whom every day would be a waste.

Thank you all!